



NTNU – Trondheim
Norwegian University of
Science and Technology

Modelling of Subsurface Releases of Oil and Gas

Testing of a New Algorithm for Droplet Size
Formation and Laboratory Verification

**Peter Johan Bergh
Lindersen**

Chemical Engineering and Biotechnology

Submission date: June 2013

Supervisor: Gisle Øye, IKP

Co-supervisor: Per Johan Brandvik, SINTEF and NTNU

Norwegian University of Science and Technology
Department of Chemical Engineering

Abstract

The objective of the Master's thesis has been modelling of subsurface blowouts of oil and gas. The main objective was to test a new algorithm for droplet size formation implemented into SINTEF's simulation tool "Marine Environmental Modelling Workbench", MEMW. A few laboratory experiments were performed with three different oil types, i.e. Alve, Norne and Svale. The crude oils were utilized in MEMW to investigate different effects such as addition of gas or dispersant. The condensate, Alve, was the default oil in the simulations due to its low viscosity.

The last couple of years the oil industry have shown an increased interest in oil and gas resources in inaccessible areas. Hence, the requirements for models to simulate subsurface blowouts of oil and gas is increasing, especially in deep water where phenomena such as hydrate formation and dissolution of gas play an important role.

The new algorithm with modified Weber number, We , predicts larger droplets than the existing algorithm where the viscosity number, Vi , is not included. The simulations with the new version of MEMW, v6.5 β yield results in accordance with existing theory.

The laboratory results obtained with SINTEF's MiniTower yielded oil droplet size distributions that were mostly in accordance with the oil droplet distributions from the simulations. The up-scaled laboratory results predicted volume median diameters, d_{50} , of oil droplets that were too large to be stable. Hence, they will be exposed to secondary droplet splitting.

Further research should emphasize on the effect of variable viscosity as a function of shear rate can have on the prediction of oil droplet size distributions. A more comprehensive and miscellaneous set of simulations with MEMW v6.5 β should be performed to test the robustness of the model. In addition, a set of new experiments with the Mini-Tower should be performed to confirm the oil droplet size distributions attained in this Master's thesis.

Sammendrag

Masteroppgaven har fokusert på modellering av undervannsutblåsninger av olje og gass. Hovedformålet har vært å kartlegge den nye algoritmen for dråpestørrelsedannelse implementert i SINTEFs simuleringsverktøy “Marine Environmental Modelling Workbench”, MEMW. Laboratorieforsøk ble utført med tre forskjellige oljetyper, Alve, Svale og Norne. De samme råoljene ble brukt i MEMW for å simulere forskjellige tilfeller. Kondensatet, Alve, var standardoljetypen i simuleringene på grunn av den lave viskositeten.

Grunnet oljeindustriens konstante søken etter å utnytte olje- og gassressurser i utilgjengelige områder er det en økende interesse for simuleringsmodeller for undervannsutblåsninger av olje og gass. Særlig på dypt vann hvor fenomener som hydratdannelse og oppløsning av gass spiller en viktig rolle.

Den nye algoritmen med modifisert Webertall, We , forutsier større dråper enn den eksisterende algoritmen der viskositetstallet, Vi , ikke er inkludert. Simuleringene med den nye versjonen av MEMW, v6.5 β , har gitt resultater i overensstemmelse med eksisterende teori.

Resultater fra laboratorieforskene, gjennomført med SINTEFs MiniTower, ga oljedråpestørrelsesfordelinger som samsvarte med fordelingene fra simuleringene. De oppskalerte laboratorieresultatene til fullskala resulterte i for store volum-mediandiametere av oljedråpene til at de var stabile. Dermed vil oljedråpene utsettes for sekundær dråpe-splitting.

Videre forskning bør legge vekt på hva den variable viskositeten, som er avhengig av skjærraten, kan resultere i for den estimerte oljedråpestørrelsefordelingen. Et mer omfattende og variert sett med simuleringer med MEMW v6.5 β bør utføres for å kartlegge robustheten av modellen. Det bør i tillegg utføres flere eksperimenter med SINTEFs MiniTower for å verifisere oljedråpestørrelsefordelingene funnet i denne masteroppgaven.

Preface

The Master's thesis in "TKP4900 - Chemical Process Technology, Master's Thesis" is performed as a collaboration between the Department of Chemical Engineering, Norwegian University of Science and Technology, NTNU, Faculty of Natural Sciences and Technology, and the Department of Marine Environmental Technology, SINTEF Materials and Chemistry.

Supervisors are professor Gisle Øye at the Colloid and Polymer Chemistry Group at the Department of Chemical Engineering, NTNU, and adjunct professor and senior research scientist Per Johan Brandvik at Department of Marine Environmental Technology, SINTEF Materials and Chemistry. Co-supervisor is Master of Science Petter Rønningen at Department of Marine Environmental Technology, SINTEF Materials and Chemistry. I appreciate the helpful discussions and good guidance during the work with my Master's thesis.

In addition, a great thanks goes to senior engineer Frode Leirvik at Department of Marine Environmental Technology, SINTEF Materials and Chemistry for invaluable help with the laboratory experiments. I would thank research scientist Umer Farooq and the helpful people at SINTEF Marine Environmental Technology that has helped me with my Master's thesis.

Finally, I would thank my good friends, Martin S. Foss and Ivar M. Jevne, for good support and inspiring discussions during the work with my Master's thesis.

Declaration of compliance

I hereby declare that this is an independent work in compliance with the exam regulations of the Norwegian University of Science and Technology.

Trondheim, 10th June, 2013

Peter J. B. Lindersen

Table of Contents

Abstract	i
Sammendrag	iii
Preface	v
Table of Contents	vii
Nomenclature	xi
List of Figures	xix
List of Tables	xxiii
1 Introduction	1
2 Theory	5
2.1 Jet and Plume Theory	5
2.2 Subsurface Blowout Models	8
2.2.1 Existing Theory on Subsurface Blowouts of Oil & Gas	8
2.2.2 A Model for Subsurface Blowouts at Shallow to Moderate Depth	11
2.2.3 Subsurface Blowouts at Deep Water	16
2.2.4 Gas Hydrates	18
2.2.5 Special Case - A Model for Subsurface Blowouts at Deep Water	19
2.2.5.1 Kinetics model for hydrate formation	19
2.2.5.2 Gas dissolution in deep water plumes	21
2.2.5.2.1 Non-ideal behaviour of gas in deep water .	22
2.2.5.2.2 The effect of pressure on solubility of gas .	23
2.2.5.2.3 The effect of salinity on solubility of gas . .	23
2.2.5.3 Blowout model with gas hydrate kinetics and inte- grated thermodynamics	24
2.2.5.4 Modelling gas separation from a bent plume	26
2.2.6 CDOG and DeepBlow Model	28

2.2.6.1	CDOG	28
2.2.6.2	DeepBlow	29
2.3	Droplet Formation from Oil Jets	29
2.3.1	Modelling of Droplet Size Formation	29
2.3.2	Basis for a New Prediction Method for Droplet Size Distributions	31
2.3.3	New Prediction Method for Droplet Size Distributions	34
2.3.4	Droplet Size Distribution Functions	35
2.4	Oil Chemistry	36
2.4.1	General Characterization of Crude Oils	36
2.4.2	Classification of Oil Types	37
2.4.3	Weathering of Crude oils at Sea	38
2.4.3.1	Oil-in-water dispersion	39
2.4.3.2	Water-in-oil emulsion	40
2.4.3.3	Evaporation	40
2.4.3.4	Additional weathering effects	41
2.4.4	Physical Characteristics of Oil	41
2.5	Interfacial Tension and Dispersants	43
2.6	Marine Environmental Modelling Workbench	47
2.6.1	Plume3D	48
3	Assumptions	51
3.1	Information from Simulations	51
3.2	Properties of Crude Oils	53
4	Experimental Work	55
4.1	Particle Size Analyzer	55
4.2	SINTEF MiniTower	56
4.3	Description of a MiniTower Experiment	60
4.4	Interfacial Tension Measurements	62
4.5	Quality Assurance and Calibration	63
5	Results	65
5.1	Simulations with MEMW	65
5.1.1	Comparison of Oil Types	65

TABLE OF CONTENTS

5.1.2	Flow Rate	67
5.1.3	Effect of Gas-to-Oil Ratio	69
5.1.4	Effect of dispersant	72
5.1.5	Dispersant-to-Oil Ratio	73
5.2	Laboratory Experiments	75
5.2.1	Monodisperse Particles	76
5.2.2	Alve Laboratory Results	77
5.2.3	Norne Laboratory Results	77
5.2.4	Svale Laboratory Results	79
5.2.5	Comparison of Volume Median Diameters	80
5.3	Interfacial Tension Measurements	80
5.4	Up-scaling from Laboratory to Full Scale Experiments	81
6	Discussion	85
6.1	Effect of Oil Type	85
6.2	Effect of GOR	86
6.3	Effect of Dispersant	87
6.4	Laboratory Experiments	89
6.5	Up-scaling of Laboratory Experiments	90
6.6	General Considerations	91
7	Conclusion	93
8	Recommendations	95
	References	97
	Appendices	
A	Add Info Theory	A-1
A.1	Derivation of a Droplet Size Distribution	A-1
A.1.1	Maximum Entropy Formalism Model for Oil Droplet Size Distribution	A-2
A.1.1.1	Numerical procedure for solving the PDF	A-4
A.1.2	Simplified Maximum Entropy Formalism-Based Models	A-5

A.1.2.1	Model 1: Conservation of mass	A-5
A.1.2.2	Model 2: Averaged specific surface area	A-6
A.2	Shear Rate	A-8
A.3	Dispersant Requirements	A-9
B	Add Info Sim and Lab Exp	B-1
B.1	Input Data to MEMW	B-1
B.2	Salinity and Temperature Profile	B-3
B.3	Size Ranges for LISST-100X Type C	B-4
C	Add Info Results	C-1
C.1	Comparison of Oil Types	C-1
C.2	Flow Rate	C-2
C.3	Effect of Dispersant	C-3
C.4	Dispersant-to-Oil Ratio	C-4
C.5	Droplet Size Raw Data	C-7
C.6	Up-scaling of Laboratory Results	C-9
C.7	Viscosity Measurements	C-10
C.8	Interfacial Tension Measurements	C-11
D	Health, Safety and Environment	D-1

Nomenclature

Latin Letters

Symbol	Explanation	Unit
a	Constant of proportionality	—
A	Constant	—
A	Factor of proportionality	—
A	Area	m^2
A	Surface area	m^2
$A_{o/w}$	Interfacial area	cm^2
$^\circ\text{API}$	Density in American literature	—
b	Radius	m
B	Buoyancy flux of mixture	m^4/s^3
B	Constant	—
B	Empirical coefficient	—
c	Empirical coefficient	—
C	Constant	—
C'	Constant	—
C	Concentration	mol/m^3
C	Mass fraction of oil concentration	—
C_0	Concentration of dissolved gas	mol/m^3
C_a	Mass fraction concentration in ambient flow	—
C_D	Drag coefficient	—
C_i	Concentration a hydrate-water interface	mol/m^3
C_i	Constant where i is 1 or 2	—
C_p	Specific heat capacity	$\text{J}/(\text{kg K})$
C_S	Saturated value of C_0	mol/m^3
C_s	Constant	—
d	Diameter	m
d_{50}	Volume median diameter	m
d_{95}	95 % maximum droplet diameter	m

Continued on next page...

Latin Letters continued

Symbol	Explanation	Unit
$d_{50,\text{disp}}$	Volume median diameter for oil with dispersant	m
$d_{50,\text{oil}}$	Volume median diameter for oil	m
d_i	Characteristic diameter	m
d_{max}	Maximum stable droplet diameter	m
D	Diffusivity	m^2/s
D	Diameter of nozzle	m
D_g	Effective diffusion coefficient	m^2/s
E	Proportionality constant	–
f	Fraction	–
f	Fugacity	MPa
f	Probability density function	–
Fr	Froude number	–
g	Standard gravity	m/s^2
g'	Reduced gravity	m/s^2
h	Element thickness	m
h	Height of a control volume	m
h_s	Separation height	m
H	Henry's law constant	Pa
H^*	Henry's law constant	$\text{mol}/(\text{m}^3 \text{ atm})$
I	Symbol for scalar parameters	–
I_a	Scalar parameter for ambient fluid	–
J	Number flux of bubbles	1/s
J_N	Number flux of bubbles	1/s
k	Constant	–
k	Mass transfer coefficient	m/s
k_i	Parameter in Rosin-Rammler	–
\vec{k}	Unit vector in vertical direction	–
K_c	Oil concentration diffusivity	m^2/s
K_f	Hydrate formation rate constant	$\text{mol}/(\text{m}^2 \text{ MPa s})$
K_r	Mass transfer coefficient	m/s

Continued on next page...

Latin Letters continued

Symbol	Explanation	Unit
K_S	Salinity diffusivity	m^2/s
K_T	Heat diffusivity	m^2/s
K_W	Thermal conductivity of water	$\text{W}/(\text{m K})$
m	Mass	kg
\bar{m}	Mean value	–
m_b	Bubble mass	kg
m_d	Mass loss due to turbulent diffusion	kg
m_h	Hydrate mass in a control volume	kg
m_i	Mass of component i	kg
m_l	Liquid mass of control volume	kg
M_0	Initial momentum	m^4/s^2
M	Molecular weight	kg/mol
M_g	Molecular weight of gas	kg/mol
M_w	Molecular weight of water	kg/mol
n	Number of moles	mol
n	Gas void fraction	–
n	Number of oil components	–
n_h	Hydrate number	–
N	Number of gas bubbles	–
p	Pressure	Pa
p_∞	Hydrostatic pressure of surrounding water	MPa
q	Constant	–
Q	Volume flow	m^3/h
Q_e	Entrainment rate for ambient water	m^3/s
Q_E	Effective volume flow	m^3/h
Q_f	Forced entrainment	m^3/s
Q_{fi}	Forced entrainment component in i direction	m^3/s
Q_g	Volume flux of gas moving out a control volume	m^3/s
Q_s	Shear-induced entrainment	m^3/s
r	Radius	m

Continued on next page...

Latin Letters continued

Symbol	Explanation	Unit
r_b	Radius of gas bubble	m
r_h	Radius of hydrate shell	m
R	Universal gas constant	J/(mol K)
Re	Reynolds number	–
Re'	Modified Reynolds number	–
s	Shape factor	–
Δs	Displacement length	m
S	Shannon's entropy	–
S	Salinity	–
S_e	Source term for energy conservation	–
S_i	Fresh water solubility	kg/m ³
S_m	Source term for mass conservation	–
S_{mv}	Source term for momentum constraint	–
Sc	Schmidt number	–
Sh	Sherwood number	–
t	Time	s
Δt	Time step	s
T	Temperature	K or °C
T_∞	Water temperature before hydrate formation	K or °C
T_a	Temperature of ambient fluid	K or °C
u	Velocity	m/s
u_∞	Velocity of cross-current	m/s
u_a	Ambient velocity	m/s
u_s	Bubble rise velocity	m/s
U	Velocity	m/s
U_0	Initial velocity	m/s
U_E	Effective velocity	m/s
U_n	Velocity, corrected for void fraction	m/s
U_{oil}	Velocity of oil jet	m/s
v_j	Jet/plume velocity	m/s

Continued on next page...

Latin Letters continued

Symbol	Explanation	Unit
v^l	Partial molar volume	m^3/mol
V	Volume	m^3
V_i	Cumulative volume fraction	–
\vec{V}	Velocity vector	m/s
\vec{V}_a	Average velocity vector of the ambient flow over the exposed buoyant jet surface	m/s
\vec{V}_a	Velocity of ambient flow	m/s
V'_a	projection of \vec{V}_a in \vec{V} 's direction	m/s
\vec{V}_g	Velocity of gas bubble	m/s
V_G	Volume flux	$\text{m}^3/(\text{m}^2 \text{ s})$
\vec{V}_j	Velocity of jet	m/s
$ \vec{V} $	Local velocity	m/s
Vi	Viscosity number	–
w	Rise velocity	m/s
w_a	Average velocity of ambient fluid over the exposed jet/plume surface	m/s
w	Vertical velocity of liquid part of the jet/plume	m/s
w_b	Slip velocity	m/s
W_K	Mixing energy	kg m/s^2
We	Weber number	–
We'	Modified Weber number	–
x^l	Mole fraction of dissolved gas in a solution	–
X_i	Molar fraction of component i	–
Z	Compressibility factor	–

Greek Letters

Symbol	Explanation	Unit
α	Entrainment coefficient	–
α	Spreading parameter	–
α_i	Empirical constant	–
β	Bubble core width and buoyant diameter ratio	–
β	Ratio between cross-sectional area occupied by gas and cross-section area of CV	–
$\gamma_{o/w}$	Oil-water interfacial tension	g cm/s ²
$\dot{\gamma}$	Shear rate	s ^{–1}
δ	Diameter	m
δ^*	Non-dimensional droplet diameter	–
ε	Bubble fraction	–
ε	Stationary turbulent dissipation rate	m ² /s ³
θ	Angle between the x -axis and the projection of the jet trajectory on the horizontal plane	°
λ	Latent heat of hydrate formation	J/mol
λ_i	Lagrangian multiplier	–
μ	Dynamic viscosity	Pas
ν	Kinematic viscosity	m ² /s
ρ	Density	kg/m ³
ρ_a	Density of ambient fluid	kg/m ³
ρ_b	Density of bubble	kg/m ³
ρ_{com}	Combined density for gas and hydrate shells	kg/m ³
ρ_G	Density of gas	kg/m ³
ρ_h	Density of hydrate	kg/m ³
ρ_l	Density of liquid	kg/m ³
ρ_{oil}	Density of oil	kg/m ³
ρ_W	Density of water	kg/m ³
$\Delta\rho$	Density deficiency	kg/m ³
σ	Interfacial tension	N/m

Continued on next page...

Greek Letters continued

Symbol	Explanation	Unit
σ_x	Standard deviation	—
τ	Travel time for one bubble through a control volume	s
ϕ	Angle between jet trajectory and the horizontal plane	°
Φ	Volume-based Rosin-Rammler distribution function	—
ψ	Overall shape factor	—

Abbreviations

Symbol	Explanation
BSD	Bubble size distribution
CDOG	Comprehensive Deepwater Oil and Gas
CMC	Critical micelle concentration
DOR	Dispersant-to-oil ratio
DCM	Dichloromethane
DREAM	Dose-related risk and assessment model
HLB	Hydrophilic-lipophilic balance
IFT	Interfacial tension
LISST	Laser In-Situ Scattering Transmissometry
MEMW	Marine Environmental Modelling Workbench
NBL	Neutral buoyancy level
OSCAR	Oil spill contingency and release
O/W	Oil-in-water
ParTrack	Particle tracking for drilling discharges
PSD	Particle size distribution
TLPD	Terminal level for plume dynamics
W/O	Water-in-oil

List of Figures

1.1	Illustration of an oil plume from SINTEF MiniTower (Brandvik, SINTEF, 2013).	2
2.1	Sketch of a subsurface plume.	6
2.2	Sketch of a subsurface plume.	7
2.3	Illustration of a subsurface plume.	18
2.4	Sketch of a gas bubble with a hydrate shell.	20
2.5	Weathering processes for crude oil in seawater.	39
2.6	Oil droplets of an arbitrary oil with three different DOR. Pictures are taken with the spinning drop video tensiometer during IFT measurements (Farooq, SINTEF, 2013).	43
2.7	Snapshot of MEMW for an arbitrary simulation.	48
3.1	Location of the Norne field with coordinates 66°2'N 8°5'E, at the Norwegian continental shelf from MEMW.	51
3.2	Vertical cross-section of a subsurface plume from MEMW. Red box indicates region of interest.	52
3.3	Illustration of maximum concentration of oil in the water column, output from MEMW.	53
4.1	Overview of the inside of the LISST-100X.	56
4.2	Schematic diagram over the SINTEF MiniTower setup (Leirvik, SINTEF, 2013).	57
4.3	Close-up of SINTEF MiniTower (Lindersen, 2013).	58
4.4	Placement of LISST-100X in the MiniTower (Lindersen, 2013).	58
4.5	Oil jet from nozzle in the MiniTower for two of the oils (SINTEF, 2013).	59
4.6	Illustration of an oil plume and an oil plume mixed with dispersant (Brandvik, SINTEF, 2013).	59
4.7	Release arrangement in SINTEF's Tower basin where 1 is the simulated insertion tool and 2 is the external insertion tool. Illustration with an arbitrary pure oil release.	61

5.1	Oil droplet size distributions for Alve, Norne and Svale. Utilized for comparison between the three oil types. Simulations with MEMW v6.2 are showed with solid lines and simulations with MEMW v6.5 β are showed with dashed lines.	66
5.2	Alve: Droplet size distributions at three different flow rates; 4800, 7200 and 9600m ³ /d. Simulations with MEMW v6.2 are showed with solid lines and simulations with MEMW v6.5 β are showed with dashed lines.	68
5.3	Alve: Droplet size distributions for four different GOR; 0, 100, 200 and 400. Simulations with MEMW v6.2 are showed with solid lines and simulations with MEMW v6.5 β are showed with dashed lines.	69
5.4	Norne: Droplet size distributions for four different GOR; 0, 100, 200 and 400. Simulations with MEMW v6.2 are showed with solid lines and simulations with MEMW v6.5 β are showed with dashed lines.	70
5.5	Svale: Droplet size distributions for four different GOR; 0, 100, 200 and 400. Simulations with MEMW v6.2 are showed with solid lines and simulations with new MEMW v6.5 β are showed with dashed lines.	71
5.6	Alve: Droplet size distributions without and with dispersant. Without dispersant are blue lines, and with dispersant are red lines. Simulations with MEMW v6.2 are showed with solid lines and simulations with MEMW v6.5 β are showed with dashed lines.	72
5.7	Alve: Droplet size distributions for six different IFT values and flow rate of 7200m ³ /d. Simulations with MEMW v6.2 are showed with solid lines.	73
5.8	Alve: Droplet size distributions for six different IFT values at a flow rate of 7200m ³ /d. Simulations with MEMW v6.5 β are showed with dashed lines.	74
5.9	Alve: d_{95} as a function of IFT, with flow rate of 7200m ³ /d, without the lowest IFT value of 0.01 mN/m.	75
5.10	Verification of the LISST measurements with monodisperse particles, or standards, with diameter of 80 μ m and 346 μ m, respectively.	76
5.11	Droplet size distributions for Alve, both with and without dispersant, from laboratory experiment. d_{50} for pure only: 259 μ m, and d_{50} for oil and dispersant: 157 μ m.	77

5.12	Droplet size distributions for Norne, both with and without dispersant, from laboratory experiment. d_{50} for pure only: 219 μm , and d_{50} for oil and dispersant: 88.2 μm	78
5.13	Droplet size distributions for Norne, at four different flow rates, from laboratory experiment. d_{50} values are presented in Table 5.10.	78
5.14	Droplet size distributions for Svale, both with and without dispersant, from laboratory experiment. d_{50} for pure only: 219 μm , and d_{50} for oil and dispersant: 128 μm	79
5.15	Oil droplets with premixed dispersant, with a DOR equal to 1:100. The pictures are taken with the spinning drop video tensiometer during the IFT measurements.	81
5.16	Alve: Comparison of calculated and measured droplet size distributions. d_{50} value for pure oil; measured was 259 μm and calculated was 125 μm . For oil mixed with dispersant; measured was 157 μm and calculated was 17 μm	82
5.17	Norne: Comparison of calculated and measured droplet size distributions. d_{50} value for pure oil; measured was 219 μm and calculated was 247 μm . For oil mixed with dispersant; measured was 88.2 μm and calculated was 140 μm	83
5.18	Svale: Comparison of calculated and measured droplet size distributions. d_{50} value for pure oil; measured was 219 μm and calculated was 353 μm . For oil mixed with dispersant; measured was 128 μm and calculated was 313 μm	84
B.1	Salinity profile for the Norne field.	B-3
B.2	Temperature profile for the Norne field.	B-3
C.1	d_{95} as a function of flow rate, blue line, and d_{max} is the asymptote, red line. C-1	
C.2	Svale: Droplet size distributions at three different flow rates; 4800, 7200 and 9600 m^3/d . Simulations with MEMW v6.2 are showed with solid lines and simulations with MEMW v6.5 β are showed with dashed lines. C-2	
C.3	Svale: Droplet size distributions without and with dispersant. Without dispersant are blue lines, and with dispersant are red lines. Simulations with MEMW v6.2 are showed with solid lines and simulations with MEMW v6.5 β are showed with dashed lines.	C-3

C.4	Alve: Droplet size distributions for six different IFT values at a flow rate of 4800m ³ /d. Simulations with MEMW v6.2 are showed with solid lines.	C-4
C.5	Alve: Droplet size distributions for six different IFT values at a flow rate of 4800m ³ /d. Simulations with MEMW v6.5 β are showed with dashed lines.	C-4
C.6	Svale: Droplet size distributions for six different IFT values at a flow rate of 4800m ³ /d. Simulations with MEMW v6.2 are showed with solid lines.	C-5
C.7	Svale: Droplet size distributions for six different IFT values at a flow rate of 4800m ³ /d. Simulations with MEMW v6.5 β are showed with dashed lines.	C-6
C.8	Viscosity measurements of Alve, Norne and Svale performed at SINTEF Sealab to check and verify the already earlier measured viscosities. . . .	C-10
C.9	IFT measurements of Alve, Norne and Svale as a function of time from the spinning drop video tensiometer.	C-11

List of Tables

3.1	The most important physical properties of Alve, Norne and Svale. . . .	54
5.1	Droplet sizes calculated for the comparison of oil types. The peak value, d_{peak} , and d_{95} are presented for MEMW v6.2. The same values are presented for MEMW v6.5 β together with the maximum stable droplet size, d_{max} . All droplet sizes in μm	66
5.2	Viscosity for the three different oil types calculated by MEMW v6.5 β compared to the earlier measured, input to MEMW, and the recently measured in the laboratory.	67
5.3	Alve: Droplet sizes for three different flow rates. The peak value, d_{peak} , and d_{95} are presented for MEMW v6.2. The same values are presented for MEMW v6.5 β together with the maximum stable droplet size, d_{max} . All droplet sizes in μm	68
5.4	Alve: Droplet sizes for simulations with and without gas. The peak value, d_{peak} , and d_{95} are presented for MEMW v6.2. The same values are presented for MEMW v6.5 β together with the maximum stable droplet size, d_{max} . All droplet sizes in μm	69
5.5	Norne: Droplet sizes for simulations with and without gas. The peak value, d_{peak} , and d_{95} are presented for MEMW v6.2. The same values are presented for MEMW v6.5 β together with the maximum stable droplet size, d_{max} . All droplet sizes in μm	70
5.6	Svale: Droplet sizes for simulations with and without gas. The peak value, d_{peak} , and d_{95} are presented for MEMW v6.2. The same values are presented for MEMW v6.5 β together with the maximum stable droplet size, d_{max} . All droplet sizes in μm	71
5.7	Alve: Droplet sizes for simulations with and without simulations. The peak value, d_{peak} , and d_{95} are presented for MEMW v6.2. The same values are presented for MEMW v6.5 β together with the maximum stable droplet size, d_{max} . All droplet sizes in μm	72

5.8	Alve: Droplet sizes for simulations with different IFT values at a flow rate of $7200\text{m}^3/\text{d}$. The peak value, d_{peak} , and d_{95} are presented for MEMW v6.2. The same values are presented for MEMW v6.5 β together with the maximum stable droplet size, d_{max} . All droplet sizes in μm	74
5.9	Flow rates for fluids utilized in laboratory experiments.	76
5.10	d_{50} values for Norne with four different flow rates.	79
5.11	d_{50} values for the three oils utilized in the laboratory experiments. Both for pure only and with dispersant with a DOR of 1:100.	80
5.12	Interfacial tension results for the fresh crude oils and with premixed dispersant for Alve, Norne and Svalde (Farooq, SINTEF, 2013).	80
5.13	Alve: Up-scaled data from MiniTower to full scale, with same diameter as utilized in simulations.	82
5.14	Norne: Up-scaled data from MiniTower to full scale, with same diameter as utilized in simulations.	83
5.15	Svalde: Up-scaled data from MiniTower to full scale, with same diameter as utilized in simulations.	84
B.1	Size ranges for spherical particle inversion method for the LISST-100X Type C.	B-4
C.1	Svalde: Droplet sizes for three different flow rates. The peak value, d_{peak} , and d_{95} are presented for MEMW v6.2. The same values are presented for MEMW v6.5 β together with the maximum stable droplet size, d_{max} . All droplet sizes in μm	C-2
C.2	Svalde: Droplet sizes for simulations with and without dispersant. The peak value, d_{peak} , and d_{95} are presented for MEMW v6.2. The same values are presented for MEMW v6.5 β together with the maximum stable droplet size, d_{max} . All droplet sizes in μm	C-3
C.3	Alve: Droplet sizes for simulations with different DOR at a flow rate of $4800\text{m}^3/\text{d}$. The peak value, d_{peak} , and d_{95} are presented for MEMW v6.2. The same values are presented for MEMW v6.5 β together with the maximum stable droplet size, d_{max} . All droplet sizes in μm	C-5

LIST OF TABLES

- C.4 Svale: Droplet sizes for simulations with different DOR. The peak value, d_{peak} , and d_{95} are presented for MEMW v6.2. The same values are presented for MEMW v6.5 β together with the maximum stable droplet size, d_{max} . All droplet sizes in μm C-6
- C.5 Raw data with droplet sizes from log files. All droplet sizes in μm C-8

1 Introduction

Understanding subsurface releases of oil and gas is crucial to predict the outcome of an eventual blowout. What will occur if large amounts of oil and gas are released at the sea bed? How will the plume¹ behave on its way to the surface? Will the plume remain in the water column? How long does it take for the oil to reach the surface? If these questions are answered, it will be easier to predict the outcome of different oil and gas releases from various depths.

Many of the questions are already answered and implemented into models for predicting subsurface releases of oil and gas. Theory for modelling of subsurface releases in shallow to moderate depth is well documented. There is insufficient theory and experimental data for subsurface releases. Johansen (2003) describe the development of a deep water blowout model as well as a verification of the model. The DeepSpill experiment, conducted in the Norwegian Sea at the Helland Hansen site at a depth of 844 meters in June 2000, has resulted in one adequate data set and are utilized to verify models worldwide (Johansen, Rye and Cooper, 2003). Experiments in more shallow water are found in e.g. Topham (1975) and Fanneløp and Sjøen (1980) among others. They describe the behaviour of the plume from a subsurface release and have yielded valuable background data for the models developed during the last years.

Droplet formation from oil jets is not well documented, however there is an increasing interest for the topic as the oil companies continue their search for fossil fuels in more complicated waters. A description of oil droplet size distributions in oil spills are found in Chen and Yapa (2007).

Plume theory for oil and gas blowouts require improvement in order to understand the behavior of the gas bubbles and the oil droplets inside the plume. To be able to understand the phenomena, it is especially important to have knowledge concerning the chemical properties. There exist many oil types which can cause challenges due to their composition, viscosity or interfacial tension in contact with seawater. The natural gases have different chemical compositions, thus affecting the formation of hydrates.

¹A plume is a elongated “cloud” of fluid, e.g. oil or gas, resembling a feather as it spreads from its point of origin (Oxford Dictionaries, 2013).



Figure 1.1: Illustration of an oil plume from SINTEF MiniTower (Brandvik, SINTEF, 2013).

The objective of the Master's thesis will be modelling of subsurface releases of oil and gas at moderate depths. A short literature review of existing theory and laboratory data from experiments with droplet formation from oil jets will be presented. Description of existing models for subsurface blowouts of oil and gas will be covered as well. A theoretical model for simulation of a deep water blowout will be presented as a special case of interest. SINTEF's simulation software Marine Environmental Modelling Workbench, MEMW, will be utilized for suitable field cases with emphasize on the formation oil droplets. Both the existing version of MEMW, v6.2, and the new version of MEMW, v6.5 β , with a new implemented algorithm for the oil droplet size distribution, will be utilized to perform the simulations. The simulations will be divided into a few different topics too investigate the effect of the new algorithm compared to the simpler algorithm in MEMW v6.2.

Laboratory experiments with SINTEF MiniTower will be conducted to verify the newly implemented algorithms in the simulation model. The experiments are a part of the Master's thesis to increase the understanding of the theory of oil droplet formation and the

oil droplet distributions. An up-scaling of the laboratory results to full scale, with the same requirements as in the simulations, will be included as well. Interfacial tension measurements for the crude oils in seawater will be performed and utilized in calculations.

2 Theory

Several topics will be addressed in the theory section to present a broad foundation for understanding subsurface blowouts of oil and gas. The topics are: general hydrodynamics theory, subsurface blowout models of oil and gas, and theory and laboratory data from experiments on droplet formation from oil jets. Theory concerning oil chemistry, dispersants and the simulation software, MEMW, are in addition mentioned in the following section.

2.1 Jet and Plume Theory

The most important characteristics of an underwater blowout are the jet region, close to the sea bed, the plume, above the jet region and below the sea surface, and the interaction zone, just below the sea surface. The jet region is not important for deep water² wells, while the plume region is of larger importance. The plume extends from the sea bed to the sea surface. A special category of the plumes are the underwater plumes and are defined as oil submerged for a long time. Smaller droplets increases the probability of formation of underwater plumes (Yapa, Wimalaratne, Dissanayake and DeGraff Jr., 2012).

The surface interaction zone is small compared to the plume region and is of large importance for weathering of oil on the surface (Fanneløp and Sjøen, 1980). Figure 2.1 illustrates a subsurface plume with the jet region, plume region and the interaction zone.

²In Yapa and Zheng (1997) the definition of deep water is 1000 meters below the sea surface and deeper. It is the oil industry's own definition. At this depth the oil and gas will experience other phenomena compared to more shallow water regions. However, another earlier European definition was 200 meters, while a new definition for an online database is now 300 meters (Infield Systems, 2013). Here, deep water will be 1000 meters and deeper.

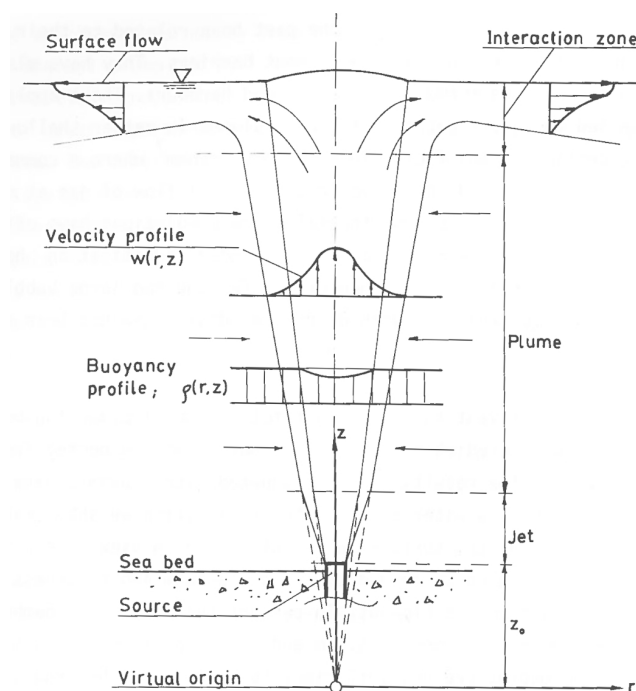


Figure 2.1: Sketch of a subsurface plume as presented in Fanneløp and Sjøen (1980).

Experiments are needed to understand the behaviour of oil and gas plumes. Fanneløp and Sjøen (1980) performed experiments with oil and gas plumes at a maximum depth of ten meters. Their experiments can be utilized to increase the understanding of plume structure, such as profile data and entrainment rates. Fanneløp and Sjøen (1980) wanted to obtain data on the plume-surface interaction as well. The focus was on thickness and speed of the outward moving layer.

Today there are several models that simulate the transport of oil and gas mixtures in deep water. The Comprehensive Deepwater Oil and Gas, CDOG, model (Zheng, Yapa and Chen, 2002; Chen and Yapa, 2002; Yapa, 2003) and the DeepBlow model (Johansen, 2000) are two examples, see section 2.2.6 for a short description. Chen and Yapa (2004b) describes a method on how to visualize multi-phase plumes. Theory on hydrodynamics is useful as it is important to have an understanding of the processed data, in order to be

able to develop accurate and robust models.

Oil and gas released from the seabed will break up into droplets and bubbles, respectively. The typical size range for droplets and bubbles are from 1 to 10 mm. Formation of small bubbles are mainly caused by high turbulence at the release point or by addition of chemical dispersants (Yapa et al., 2012).

The oil droplet size do not significantly affect the transport of the mixture of plume fluid. There is a substantial quantity of water entrained in the plume. Hence, the phases are initially clustered together and then move as an integral mixture. The gas bubble size, will in contrast to the oil droplet size, affect the initial phase of the plume. Dissolution of gas and hydrate formation are phenomena affecting the bubble sizes. The phases will move differently with their own buoyant velocity. The movement is dependent on shape, size and density of droplets and bubbles. The terminal level for plume dynamics, TLPD, is the level where the plume dynamics is not important any more. Above the TLPD the oil droplet size distribution become important, as smaller droplets move slower towards the surface compared to larger droplets. Cross currents move droplets laterally, thus the droplets can spread in all directions. Turbulent dispersion and diffusion of droplets are other natural processes occurring in the seawater (Yapa et al., 2012).

The TLPD is illustrated as the terminal layer right above where the plume ends in Figure 2.2. The figure depict a blowout from 1500 meters depth. The formation of gas hydrates, will only take place below a certain depth and may not always occur in more shallow water.

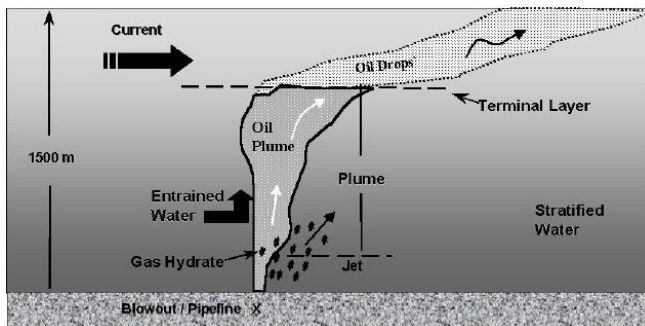


Figure 2.2: Sketch of a subsurface plume as presented by Lane and Labelle (2000).

Simulations have shown that the TLPD can be calculated based on buoyant oil droplet velocity, that corresponds to the median oil droplet size. A detailed examination of the criteria utilized for the TLPD can be found in Dasanayaka and Yapa (2009).

The most important processes for a plume in deep water with regard to change in composition and mass are (Johansen, 2003):

- Hydrate formation
- Dissolution of gas
- Separation of gas bubbles and oil droplets from bent plumes

2.2 Subsurface Blowout Models

Three main parts are covered in the section below; existing theory on subsurface blowouts of oil and gas, a model for blowouts occurring at shallow to moderate depth and a model for blowouts occurring in deep water.

2.2.1 Existing Theory on Subsurface Blowouts of Oil & Gas

A blowout model developed by Spaulding, Bishnoi, Anderson and Isaji (n.d.) solves the conservation of oil mass, water mass, buoyancy and momentum equations by using integral plume theory. A multi-phase flash calculation is utilized in the model to calculate equilibrium hydrate formation and dissociation for methane gas, the details are found in Bishnoi, Gupta, Englezos and Kalogerakis (1989). The blowout model predicts the plume centerline velocity, trapping depth, half width and buoyancy. Released oil and hydrates are transported as individual particles is assumed. A three dimensional, random walk model is utilized to calculate the transport of particles as the plume becomes trapped (Spaulding et al., n.d.).

An experiment describing the plume trap height for a plume in the water column with air is presented in Seol, Bryant and Socolofsky (2009). These data can contribute to a better understanding of oil plumes in seawater.

A data set or a hydrodynamic model is utilized to predict the horizontal advective currents, while oil and hydrate rise velocities are determined with Stokes law. In the model, the plume is predicted to be trapped and it usually occurs within 60 meters of the release depth. An important process, controlling plume dynamics in deep water, is hydrate formation affected by the entrainment rate (Spaulding et al., n.d.).

An oil well blowout was performed by Topham (1975) at two different depths, 60 meters and 23 meters. A few of the conclusions from the work are;

- The rising plume is initially conical in shape, however it becomes cylindrical above a certain height as long as the release depth is large enough.
- Mean centerline velocities was not affected in considerable amounts by air flow or depth, for a specific plume height.
- Difficult to extrapolate data considerably outside the range of experiments.

Bettelini and Fanneløp (1993) describes a model for an underwater plume from an instantaneously started source at the seabed, together with a comparison of existing data.

Theory describing general multiphase plumes can be applicable to subsurface blowouts of oil and gas and can be found in e.g. Socolofsky and Adams (2003), Socolofsky and Adams (2005) and Socolofsky, Bhaumik and Seol (2008). These papers describes the multiphase plumes with respect to liquid volume fluxes, the role of slip velocity and a double-plume integral model for near-field mixing, respectively.

Data from one of the more recent oil spills, the Macondo³ blowout, can be found in e.g. S.L Ross Enviromental Research Ltd. (1997) and Ryan, Zhang, Thomas, Rienecker and Cummings (2010). A simulation of underwater plumes originating in the Gulf of Mexico can be found in Adcroft, Hallberg, Dunne, Samuels, Galt, Barker and Payton (2010). Analysis of the data from Macondo are utilized to obtain an increased in depth knowledge for deep water blowouts.

Data from a field experiment performed in June 1996 at 106 meters depth yielded re-

³The Deepwater Horizon spill, also called the Macondo blowout, was an accident with a loss of well control with subsequent explosions, fire in a well and the loss of 11 lives. The eventual sinking and total loss of the DEEPWATER HORIZON rig, and the continuous release of hydrocarbons into the Gulf of Mexico. The flow was stopped on July 15 2010 and the well was declared sealed on September 19 2010 (Republic of the Marshall Islands Maritime Administrator, 2011).

sults worth mentioning. First of all, the experiments showed that the field methodology utilized for studying blowouts appears to be appropriate. Secondly, the surface oil slick formed by a subsurface release is thinner and wider compared to a surface release. Thirdly, only a small amount of oil released was observed at the surface and the quantity is dependent on depth, gas-to-oil ratio, GOR, release velocity and oil type. The experiments also indicated differences from existing models, thus the data can be utilized for improvements (Rye, Brandvik and Strøm, 1997).

A verification of two field experiments, one in 1995 and the other in 1996, with existing computer models are presented in Rye and Brandvik (1997). The modelling results are in agreement with field experiments, however the size of the oil slick at the sea surface is occasionally overestimated by the computer model.

In Yapa and Xie (2002) the variation of jet/plume⁴ diameter as a function of depth for a selection of field experiments was compared with model simulations. A correspondence between experimental data and model simulations was observed. Still, there is less difference between the results if the jets have high gas-to-liquid ratios (Yapa and Xie, 2002).

In Lee and Cheung (1990) a general Lagrangian jet model, applicable for jets of oil and gas from subsurface blowouts, is presented. In Fry and Adams (1983) a general jet was studied, both experimentally and theoretically. General theory for jets can be utilized to improve the understanding of oil jets, even though it is not directly attached to jet theory for subsurface blowouts of oil and gas. Lin and Lian (1998) describes the breakup of liquid jets and a better knowledge in the area will improve the understanding of an oil jet created at the sea bed.

It is important to know the buoyant velocity of droplets and bubbles with different shapes. The knowledge is important for simulating blowouts, e.g. if the assumption of spherical shape of oil droplets is not valid. A calculation method proposed by Zheng and Yapa (2000) calculate the buoyant velocity for oil droplets, gas bubbles and hydrate particles.

⁴Jet/plume refer to a jet or a plume as it is not necessary to identify where the transformation from jet to plume occurs. The plume will eventually reach a neutral buoyancy level ,NBL, where the dynamics of the jet/plume ends (Chen and Yapa, 2004a).

2.2.2 A Model for Subsurface Blowouts at Shallow to Moderate Depth

A model describing subsurface blowouts of oil and gas at shallow to moderate depth is presented in detail in (Yapa and Li, 1997). The three-dimensional numerical model can simulate behaviour of oil in unstratified or stratified ocean environments. The model utilizes a Lagrangian integral technique and considers multi-directional ambient currents. The buoyant jet can simulate fluids such as liquid, gas or a liquid/gas mixture. Forced and shear entrainment are included in the model. It includes dissolution and diffusion of oil from the buoyant jet to ambient surroundings.

A verification of the model is found in (Yapa and Li, 1998), where the model described in Yapa and Li (1997), is tested with several simulations. Several variable conditions are tested to validate the robustness of the model. First, the results were validated with the asymptotic values to see if they matched in the limits. Second, the simulation results were validated with multiple experimental data for both small and large scale. The data utilized for comparison with the numerical model include both with and without ambient current, and two- and three-dimensional jet trajectories. The comparison yields a coherence between simulations and experimental data.

The model presented above is the basis for an extended model derived in (Yapa, Zheng and Nakata, 1999). Oil transport further away from the plume, intermediate and far-field, is added to improve the original model. Scenario simulations were also performed to demonstrate the model capability.

The model by Yapa and Li (1997) is described with equations in the remaining part of the section. Significant modifications are performed to adapt the model for blowouts. Assumptions to the processes are:

- Cross-section of the oil buoyant jet is round and perpendicular to the trajectory.
- The model is quasi-steady.
- The control volume has the shape of a bent cone.
- Variables included in the model represent the average values for the cross-section, top-hat profile.
- Effect of oil viscosity is neglected when considering the turbulent behaviour of

the submerged oil buoyant jet.

- Forced entrainment of ambient fluid into the buoyant jet occurs from the frontal side of the buoyant jet.
- If gas is present in the buoyant jet fluid, then it is assumed that the mass flow rate of the bubble is constant at each cross-section.

The governing equations for buoyant jets with no gaseous mixtures are presented below. The control volume is a Lagrangian⁵ element moving along the centerline of the buoyant jet. The Lagrangian element moves with its local centerline velocity. The element thickness is calculated by Equation (2.1) and the mass of the element by Equation (2.2).

$$h = |\vec{V}|\Delta t \quad (2.1)$$

$$m = \rho \pi b^2 h \quad (2.2)$$

where $|\vec{V}|$ is local velocity, Δt is the time step, ρ is density of buoyant jet and b is radius.

The conservation of mass for a jet/plume fluid is presented in Equation (2.3), where the second term on the right-hand side represents the dissolution of oil into water.

$$\frac{dm}{dt} = \rho_a Q_e - \sum_i^n \frac{dm_i}{dt} - \frac{dm_d}{dt} \quad (2.3)$$

where ρ_a is density of ambient fluid and Q_e is entrained volume flux due to shear-induced entrainment, Q_s , and forced entrainment, Q_f .

The dissolution term can be written as presented in Equation (2.4).

$$\frac{dm_i}{dt} = K_r \alpha_i A X_i S_i, \quad (i = 1, 2, \dots, n) \quad (2.4)$$

where m_i is mass loss due to dissolution of oil component i from the buoyant jet into ambient fluid, K_r is mass transfer coefficient of dissolution, α_i is an empirical constant equal to 0.7 and A is area of exposed buoyant jet surface equal to $2\pi b h$. X_i is molar fraction of component i , S_i is fresh water solubility of component i and n is number of

⁵A finite Lagrangian control volume is moving with the fluid, thus the same fluid particles are always in the same control volume. A finite Eulerian control is fixed in space and the fluid is moving through it (Jakobsen, 2008).

oil components utilized in the simulation.

The third term on the right-hand side of Equation (2.3) is the mass loss rate due to turbulent diffusion and can be related to the concentration gradient. The term is presented in Equation (2.5).

$$\frac{dm_d}{dt} = \rho_a K_C A \left| \frac{\partial C}{\partial r} \right| \approx \rho_a K_C \pi b h \frac{C - C_a}{b} \quad (2.5)$$

where K_C is oil concentration diffusivity, C and C_a are mass fraction oil concentrations in buoyant jet and ambient flow, respectively.

Equation (2.6) presents the conservation of momentum. The first term on the right-hand side of the equation represents the momentum from the entrained mass, while the two last terms represents the net force acting on the control volume. The drag force is neglected in the simulations, i.e. $C_D = 0$.

$$\frac{d(m\vec{V})}{dt} = \vec{V}_a \frac{dm}{dt} + m \frac{\Delta\rho}{\rho} g \vec{k} - \rho 2bh C_D \left(\left| \vec{V} \right| - V'_a \right)^2 \frac{\vec{V}}{\left| \vec{V} \right|} \quad (2.6)$$

where \vec{V}_a is average velocity vector of the ambient flow over the exposed buoyant jet surface, $\Delta\rho = (\rho_a - \rho)$ is density deficiency, C_D is the drag coefficient, V'_a is projection of \vec{V}_a in \vec{V} 's direction and \vec{k} is an unit vector in vertical direction.

Equation (2.7) is an equation for for calculating conservation of heat, oil mass and salinity.

$$\frac{d(mI)}{dt} = I_a \frac{dm}{dt} - \rho_a K 2\pi b h \frac{I - I_a}{b} \quad (2.7)$$

where I is a symbol for the scalar parameters of the buoyant jet and I_a is a scalar parameter for ambient fluid. For the conservation of heat; $I = C_p T$ where C_p is specific heat capacity and assumed constant, and T is temperature. For the conservation of oil; $I = C$ and for the conservation of salinity; $I = S$. K represents diffusivities, e.g., heat diffusivity K_T , oil concentration diffusivity K_C and salinity diffusivity K_S .

When Equation (2.7) is utilized for calculating the oil concentration, an additional term

accounting for the oil dissolution rate is added on the right-hand side of the equation. The additional term is presented in Equation (2.8).

$$\sum_i^n \frac{dm_i}{dt} \quad (2.8)$$

To fulfill the governing equations to simulate a buoyant jet, a state equation is required. It describes the change in density due to temperature, salinity and concentration. The general and functional form of the state equation is:

$$\rho = \rho(T, S, C) \quad (2.9)$$

Equation (2.9) will have different forms depending on the type of fluid in the buoyant jet.

If gas is present in the jet, the governing equations requires modification. In the model it is assumed that the bubble occupy the inner core even when the jet is bent, as there is no information available for the phenomena. The ratio between the bubble core width and the jet diameter is defined as β . β is set to 0.7 in the model. The slip velocity, w_b , is the vertical difference between the bubbles and the liquid part of the buoyant jet. It is set to 0.3 m/s in the model. Within the bubble core, there is a bubble fraction, ε , defined as presented in Equation (2.10).

$$\varepsilon = \frac{\rho_l - \rho}{\rho_l - \rho_b} \quad (2.10)$$

where ρ_b is density of a bubble determined by ideal gas law, ρ_l is density of the liquid determined by Equation (2.9), and ρ is density of the mixture of liquid and bubble.

Presence of gas bubbles can be included in the existing framework by assuming that Equation (2.3) is the same for the liquid part. For the gas part, it is assumed that the mass flow rate is constant at each cross-section, see Equation (2.11).

$$\frac{dm_b}{dt} = 0 \quad (2.11)$$

where m_b is the bubble mass of the control volume, calculated as $\rho_b \pi b^2 \beta^2 h \varepsilon$.

The momentum equation for the vertical direction is modified to incorporate the slip velocity, as presented in Equation (2.12). The first term on the right-hand side of equation is the momentum from entrained liquid mass. From the ambient fluid no gas is entrained. The second term considers vertical force acting in the liquid part. The third and last term include the vertical forces acting on gas.

$$\begin{aligned} \frac{d}{dt} [m_l w + m_b (w + w_b)] = w_a \frac{dm_l}{dt} + (\rho_a - \rho_l) g \pi b^2 (1 - \beta^2 \epsilon) h \\ + (\rho_a - \rho_b) g \pi b^2 \beta^2 h \epsilon \end{aligned} \quad (2.12)$$

where $m_l = \rho_l \pi b^2 (1 - \beta^2 \epsilon) h$ is liquid mass of the control volume. w_b is slip velocity, w is vertical velocity of liquid part of the jet/plume and w_a is average velocity of ambient fluid over the exposed jet/plume surface.

The entrainment process can be divided into two separate processes, shear-induced entrainment and forced entrainment. The shear-induced entrainment, calculated by Equation (2.13), is due to shear between the buoyant jet and the ambient.

$$Q_s = 2\pi b h \alpha \left| \left| \vec{V} \right| - V'_a \right| \quad (2.13)$$

where α is an entrainment coefficient.

The entrainment coefficient can be calculated by the local Froude number, Fr , and the local jet spreading rate. Equation (2.14) is one method to calculate the entrainment coefficient. More details are found in Yapa and Li (1997).

$$\alpha = \sqrt{2} \frac{0.057 + \frac{0.554 \sin \phi}{Fr^2}}{1 + 5 \frac{V'_a}{\left| \left| \vec{V} \right| - V'_a \right|}} \quad (2.14)$$

where Fr is calculated by Equation (2.15).

$$Fr = E \frac{\left| \left| \vec{V} \right| - V'_a \right|}{\left(g \frac{\Delta \rho}{\rho_a} b \right)^{1/2}} \quad (2.15)$$

where ϕ is the angle between the jet trajectory and the horizontal plane, g is standard

gravity and E is a proportionality constant, equal to 2.0 in the simulations performed by Yapa and Li (1997).

The forced entrainment is due to advection of ambient current into the buoyant jet. For a three-dimensional trajectory in a three-dimensional ambient flow field the forced entrainment is calculated by Equations (2.16) through (2.18).

$$Q_{fx} = \rho_a |u_a| \left[\pi b \Delta b |\cos \phi \cos \theta| + 2b \Delta s \sqrt{1 - \cos^2 \theta \cos^2 \phi} + \frac{\pi b^2}{2} |\Delta (\cos \phi \cos \theta)| \right] \Delta t \quad (2.16)$$

$$Q_{fy} = \rho_a |v_a| \left[\pi b \Delta b |\cos \phi \sin \theta| + 2b \Delta s \sqrt{1 - \sin^2 \theta \cos^2 \phi} + \frac{\pi b^2}{2} |\Delta (\cos \phi \sin \theta)| \right] \Delta t \quad (2.17)$$

$$Q_{fz} = \rho_a |w_a| \left[\pi b \Delta b |\sin \phi| + 2b \Delta s |\cos \phi| + \frac{\pi b^2}{2} |\Delta (\sin \phi)| \right] \Delta t \quad (2.18)$$

where Q_{fx} , Q_{fy} and Q_{fz} are forced entrainment components in x , y and z direction, respectively. u_a , v_a and w_a are components of \vec{V}_a in x , y and z direction, respectively. The displacement length, $\Delta s = \sqrt{\Delta x^2 + \Delta y^2 + \Delta z^2}$, where Δx , Δy and Δz are displacements of a control volume during one time step in x , y and z direction, respectively. θ is the angle between the x -axis and projection of the jet trajectory on the horizontal plane.

The numerical method utilized to solve the governing equations in the Lagrangian frame is a finite-difference discretization. The numerical solution is explicit. Additional assumptions made to solve the model are found in Yapa and Li (1997).

2.2.3 Subsurface Blowouts at Deep Water

The industry is moving further down into deeper waters where the environmental conditions are unknown. It resulted in the formation of the Deep Spills Task Force in 1998 (Lane and Labelle, 2000). Their task was to improve the understanding of subsurface releases of oil and gas in deep waters.

Models for subsurface blowouts at deep water are different from models at shallow to moderate depths. The main reason for it are the phenomenas occurring at greater depths. Important deep water processes are (Johansen and Durgut, 2006; Yapa, 2003):

- Shallow to moderate depths, the gas can be considered as an ideal gas. At greater depths the gas must be assumed to be non-ideal using a compressibility factor with the pressure-volume relationship.
- Fraction of gas dissolved in the oil will increase with pressure.
- Shallow to moderate depths, dissolution of gas from rising bubbles into seawater is negligible. In deep waters, dissolution of gas in seawater can cause a noticeable reduction in buoyancy flux.
- If gas hydrates are formed at larger depths, contribution of gas to buoyancy flux will vanish. Trapping of plume caused by density gradients in the ambient seawater may occur.
- At deep water blowouts, the spreading of the oil is due to droplet size distribution of oil, the variability and strength of the ambient current. While at moderate depths, the spreading of oil will mostly be caused by the radial outflow of seawater entrained by the rising gas bubble plume.

A model of gas separation from a bent deep water oil and gas jet/plume is described in Chen and Yapa (2004a). It is especially of interest for deep water models when strong ambient currents are present. The oil and gas jet/plume will be bent and gas may separate from the plume and rise towards the surface with its own velocity. The separation of gas from the bent plume can lower the NBL of the plume. Thus, a change in the oil droplet trajectory and the surface oil slick can be induced. Hence, the location of transition of the jet/plume mixing to the far-field turbulent mixing has been changed drastically (Chen and Yapa, 2004a).

A model proposed by Zheng et al. (2002) will be presented in the remaining part of the section.

Important aspects to consider for a deep water oil and gas blowout model according to Zheng et al. (2002) are:

- Kinetics of hydrate formation and decomposition
- Dissolution of gases in deep water plumes
- Buoyant velocity of oil, gas and hydrate particles/bubbles
- Integrate thermodynamics and gas hydrate kinetics with the jet/plume model
- Gas separation from a bent plume

Figure 2.3 shows how Zheng et al. (2002) illustrate a subsurface blowout of oil and gas from an oil well.

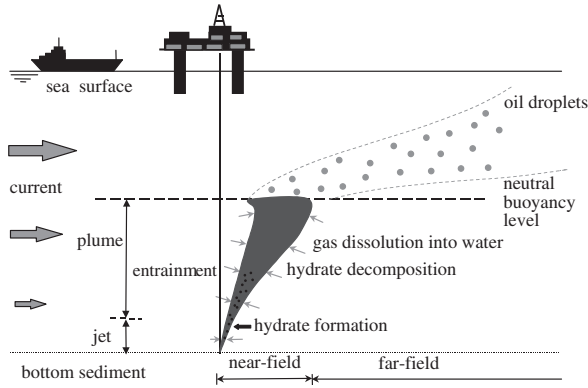
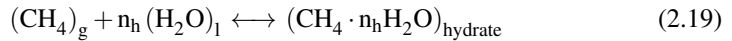


Figure 2.3: Illustration of a subsurface plume as presented by Zheng et al. (2002).

2.2.4 Gas Hydrates

The gas hydrates consists of water and gas, the combination result in a slush-like compound that are similar to frazil ice⁶. The chemical reaction for hydrate formation with methane, CH_4 , is shown in Equation (2.19) (Zheng et al., 2002).



⁶Frazil ice is the first stage in the formation of sea ice and is a collection of randomly, loose oriented needle-shaped ice crystals in water. It sporadically forms in turbulent, open, supercooled water (Daly, 1991).

Hydrates have the possibility to be formed when gas is released under high pressures and low temperatures, it is the case for deep water blowouts. The hydrates rise towards the surface due to their buoyant nature and they change the overall buoyancy of the plume. Gas hydrates can transform back to gas as the pressure decreases and the temperature increases towards the surface (Yapa et al., 2012).

A more detailed model estimating hydrate formation and decomposition of gases released in a deep water ocean plume is presented in Chen and Yapa (2001) and Yapa, Zheng and Chen (2001). The model presented in Chen and Yapa (2001) is based on earlier work from the 1980's. Another scientific paper published in 1980 investigated hydrate formation behaviour of natural gas bubbles in the laboratory (Maini and Bishnoi, 1981). The experiments were performed in a simulated deep sea environment, the results were utilized to increase the understanding of blowouts in deep waters. More knowledge about hydrate formation and a review of older literature can be found in e.g. Englezos (1993) and McCain Jr. (1990).

Topham (1984) describes a model for hydrocarbon plumes to include gas hydrate formation where the results indicate that below 800 meters from the sea surface, all gas will be converted to hydrate before reaching the surface.

2.2.5 Special Case - A Model for Subsurface Blowouts at Deep Water

Zheng et al. (2002) describe a complete model for subsurface blowouts at deep waters. The model considers hydrate formation, gas dissolution and gas separation from a bent plume. The most important equations are presented together with explanations of the terms. The model is presented as a special case since it should obtain increased attention during the next couple of years.

2.2.5.1 Kinetics model for hydrate formation

To be able to model hydrate formation in the gas phase of the jet/plume, hydrate kinetics must be combined with mass and heat transfer. Figure 2.4 shows a sketch of a gas bubble coated with hydrate. The same methodology, as for the single gas bubble, is applied to multiple gas bubbles, which is the case for a blowout.

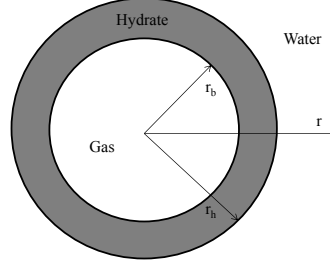


Figure 2.4: Sketch of a gas bubble with a hydrate shell, similar to a figure by Zheng et al. (2002).

Assumptions for the hydrate kinetics are e.g. mass and heat transfer at any cross-section is the same at a specific time. More assumptions can be found in Zheng et al. (2002). The rate of hydrate growth is described by Equation (2.20).

$$\frac{dn}{dt} = K_f A (f_{\text{dis}} - f_{\text{eq}}) \quad (2.20)$$

where K_f is a hydrate formation rate constant, $A = 4\pi r_h^2 \psi$ is hydrate formation surface area, ψ is overall shape factor to take into account non-spherical shape and f is fugacity, subscripts “dis” and “eq” is short for dissolved gas and at three-phase equilibrium condition, respectively.

The mass transfer rate or the quasi-steady diffusion equation with boundary conditions for the hydrate zone is presented in Equation (2.21).

$$\begin{aligned} \frac{d}{dr} \left(r^2 \frac{dC}{dr} \right) &= 0, \quad r_b \leq r \leq r_h \quad (2.21) \\ C(r_b) &= C_0 \\ C(r_h) &= C_i \\ -D_g 4\pi r_h^2 \psi_s \frac{dC}{dr} \Big|_{r=r_h} &= \frac{dn}{dt} \end{aligned}$$

where C is the gas concentration, C_i is concentration at the hydrate-water interface, C_0 is concentration at the hydrate-gas interface, D_g is effective diffusion coefficient and r_b, r_h is radii of gas bubble and hydrate shell, respectively.

The heat transfer rate or quasi-steady diffusion equation with boundary conditions for the water zone is presented in Equation (2.22).

$$\begin{aligned} \frac{d}{dr} \left(r^2 \frac{dT}{dr} \right) &= 0, & r &\geq r_h \\ T(r_h) &= T_i \\ T(\infty) &= T_\infty \\ -K_w 4\pi r_h^2 \psi_s \frac{dT}{dr} \Big|_{r=r_h} &= \lambda \frac{dn}{dt} \end{aligned} \quad (2.22)$$

where T is temperature at the hydrate-water interface, T_∞ is water temperature before hydrate formation, λ is latent heat of hydrate formation and K_w is thermal conductivity of water.

The size of gas bubbles can be calculated by using the non-ideal gas law as expressed in Equation (2.23).

$$p_\infty \frac{4}{3} \pi r_b^3 = n Z R T_\infty \quad (2.23)$$

where p_∞ is hydrostatic pressure of surrounding water, n is number of moles, Z is the compressibility factor and R is the universal gas constant.

The kinetics of hydrate decomposition can be described in a similar way to Equation (2.20). The difference is that the fugacity terms will be reversed, where f_{dis} will be replaced with f_g^v , the fugacity of gas at the particle surface temperature and pressure of surrounding water. The kinetic rate constant will be an exponential function of hydrate particle surface temperature. The effect of heat transfer for decomposition of hydrates are neglected, the details are found in Yapa et al. (2001).

2.2.5.2 Gas dissolution in deep water plumes

The dissolution rate of gas, Equation (2.24), is proportional to the surface area of the bubble, concentration difference between surface of bubble and surrounding water, and magnitude of mass transfer coefficient. It is necessary to calculate since dissolution of

gas will occur inside the jet/plume in deep waters.

$$\frac{dm}{dt} = kMA (C_S - C_0) \quad (2.24)$$

where m is mass of a gas bubble, k is a mass transfer coefficient, M is molecular weight of gas, A is surface area of a gas bubble, C_0 is concentration of dissolved gas and C_S is saturated value of C_0 .

The mass transfer coefficient, k , is expressed with the dimensionless Sherwood number, Sh , see Equation (2.25) (Johansen, 2003).

$$Sh = \frac{kd}{D} \quad (2.25)$$

where d is diameter of the droplet or bubble and D is diffusivity of the dispersed phase in liquid.

The Sherwood number can be described as a function of the Reynolds number, Re , see Equation (2.26), and the Schmidt number, Sc , see Equation (2.27). An empirical relation for the Sh number, valid for a rigid sphere in a liquid, is presented in Equation (2.28).

$$Re = \frac{wd}{\nu} \quad (2.26)$$

$$Sc = \frac{\nu}{D} \quad (2.27)$$

$$Sh = 2 + 0.95Re^{1/2}Sc^{1/3} \quad (2.28)$$

where w is rise velocity of bubbles or droplets and ν is kinematic viscosity of the continuous phase, water.

2.2.5.2.1 Non-ideal behaviour of gas in deep water

Non-ideal behavior of gas in deep water is another phenomena to consider for a subsurface blowout of oil and gas. The reason is the high ambient pressure. The compressibility factor, Z , describes the deviation of a real gas compared to an ideal gas, as shown in

Equation (2.29).

$$Z = \frac{V_{\text{actual}}}{V_{\text{ideal}}} \quad (2.29)$$

Equation (2.30) is an equation of state for a real gas based on the ideal gas law (McCain Jr., 1990).

$$Z = \frac{pV}{nRT} \quad (2.30)$$

2.2.5.2.2 The effect of pressure on solubility of gas

Henry's law, Equation (2.31), is utilized to calculate the solubility of gas in water for low pressures.

$$p = Hx^l \quad (2.31)$$

where H is Henry's law constant, dependent on water temperature, and x^l is mole fraction of dissolved gas in a solution.

With the higher pressure in deep waters it is possible to utilize a modified version of Henry's law, as presented in Equation (2.32). The two equations above should be utilized to include the effect of pressure on solubility.

$$f^g = Hx^l \exp\left(\frac{pv^l}{RT}\right) \quad (2.32)$$

where f^g is fugacity of gas in gas phase and v^l is partial molar volume of gas in solution.

2.2.5.2.3 The effect of salinity on solubility of gas

To simplify Equation (2.32), it is rewritten to Equation (2.33) which also includes the effect of salinity on solubility of gas.

$$C_S = H^* f^g \exp\left(\frac{(1-p)v^l}{RT}\right) \quad (2.33)$$

where H^* is a different type of Henry's law constant.

The buoyant velocity of hydrate particles, oil droplets and gas bubbles must be calculated. It is accounted for by determining the terminal velocity of bubbles, which is assumed to be the same as the slip velocity in a plume. More details of the calculations are found in Zheng and Yapa (2000).

2.2.5.3 Blowout model with gas hydrate kinetics and integrated thermodynamics

The equations for hydrate formation and decomposition are integrated with the jet/plume hydrodynamic model. The governing equations of the main jet/plume is described in the following, starting with the number of gas bubbles, N in a CV in Equation (2.34). The equation neglects strong cross flows (Zheng et al., 2002).

$$N = \frac{J_N h}{w + w_b} \quad (2.34)$$

where J_N is number flux of bubbles, h is height of the CV, w is vertical velocity of plume liquid and w_b is gas slip velocity.

If there is strong cross flow conditions affecting the jet/plume it will be bent. Gas may separate from the main jet/plume and the number of bubbles in a CV is calculated as in Equation (2.35).

$$N = \frac{f J h}{v_j + w_b \sin \phi} = f J \tau \quad (2.35)$$

where τ is travel time for one bubble through the CV, v_j is jet/plume velocity, ϕ is angle of jet/plume axis from the horizontal plane and f is a fraction representing the gas portion left in the CV.

Conservation of liquid mass, Equation (2.36), is applied to the CV. The last term, on the right hand side of the equation, is the rate of loss or gain of water mass induced by hydrate formation and decomposition.

$$\frac{dm_l}{dt} = \rho_a Q_e - f \cdot J \cdot \tau \cdot n_h \frac{dn}{dt} M_w \quad (2.36)$$

where $m_l = \rho_l \pi b^2 (1 - \beta \epsilon) h$ is the liquid mass in the CV, β is a ratio between the cross-

sectional area occupied by gas and cross-section area of the CV, $\varepsilon = (\rho_l - \rho) / (\rho_l - \rho_{com})$ is volume fraction of gas bubbles with hydrate shell where $\rho_{com} = (\rho_b r_b^3 + \rho_h (r_h^3 - r_b^3)) / r_h^3$. $\rho_l, \rho, \rho_{com}, \rho_b, \rho_h$ and ρ_a are the densities of the liquid part of CV, gas-liquid mixture in plume, combined gas and hydrate shells, gas, hydrate, and ambient fluid, respectively. r_b, r_h is inner and outer radii of a gas bubble with a hydrate shell, Q_e is entrainment rate for ambient water, n_h is the hydrate number, M_w is molecular weight of water and $\frac{dn}{dt}$ is hydrate formation rate for one bubble.

The gas loss due to free gas dissolution and hydrate formation is presented in Equation (2.37).

$$\Delta m_b = -f \cdot J \cdot \tau \left(\frac{dn}{dt} + \frac{dn_s}{dt} \right) M_g \Delta t \quad (2.37)$$

where $\frac{dn_s}{dt}$ is rate of gas dissolution for one gas bubble, M_g is molecular weight of gas and Δt is the time step.

Average conditions within a CV are utilized for the momentum equations, Equations (2.38) through (2.40). The slip velocity between liquid and gas/hydrate is still considered. The drag force due to the change of flow field is neglected.

$$\frac{d}{dt} [(m_l + m_b + m_h) \cdot u] = u_a \rho_a Q_e - u \rho_{com} Q_g \quad (2.38)$$

$$\frac{d}{dt} [(m_l + m_b + m_h) \cdot v] = v_a \rho_a Q_e - v \rho_{com} Q_g \quad (2.39)$$

$$\begin{aligned} \frac{d}{dt} [m_l w + (m_b + m_h)(w + w_b)] = & w_a \rho_a Q_e - w \rho_{com} Q_g + (\rho_a - \rho_l) g \pi b^2 (1 - \beta \varepsilon) h \\ & + (\rho_a - \rho_{com}) g \pi b^2 \beta \varepsilon h \end{aligned} \quad (2.40)$$

where m_h is hydrate mass in a CV, u, v and w is the cross-sectional averaged velocity of the CV in three orthogonal directions, and Q_g is volume flux of gas moving out of the CV.

The first term on the right hand side of Equations (2.38) through (2.40) represent the

momentum from the entrained liquid mass. The second term on the right hand side represents the loss of momentum due to gas moving outside the jet/plume boundaries. The third term in Equation (2.40) on the right hand side has to do with the vertical force acting on the liquid part. The fourth and last term on the right hand side in Equation (2.40) describes the vertical force acting on the gas bubbles with the hydrate shells (Zheng et al., 2002).

Equation (2.41) describes the conservation of heat, where the heat content for gas is neglected. It is very small compared to liquid and hydrate part. The first term on the right hand side represents heat input from entrained water. The second term is the change in heat energy due to loss or gain of latent heat with hydrate decomposition and formation (Zheng et al., 2002).

$$\frac{d}{dt} [(C_{p_l} m_l + C_{p_h} m_h) T] = C_{p_l} T_a \rho_a Q_e + f \cdot J \cdot \tau \cdot \frac{dn}{dt} \lambda \quad (2.41)$$

where C_{p_l}, C_{p_h} is the specific heat capacity of liquid and hydrate at constant pressure, respectively. T is temperature of the plume, T_a is temperature of ambient fluid and λ is latent heat of hydrate formation or decomposition.

Conservation of oil mass and salinity can be calculated with Equation (2.42) where the change of salinity or oil mass in the CV is due to entrained mass input.

$$\frac{d(m_l I)}{dt} = I_a \frac{dm_l}{dt} \quad (2.42)$$

where I is either oil concentration by mass, C , or salinity, S .

Tracking the fate⁷ and trajectories of gas bubbles are important, especially if the gases are toxic or flammable.

2.2.5.4 Modelling gas separation from a bent plume

If there is a cross flow the plume will be bent. It can result in escaping oil droplets and gas bubbles. An earlier suggested equation for calculation of the critical separation height, h_s , is presented in Equation (2.43). It was first presented by Davidson and Pun

⁷Fate is a term utilized to describe the development of the oil or gas in the environment.

(1999) and does not include the ambient density stratification in seawater.

$$h_s = C_s \frac{M_0^{1/2}}{u_s} \quad (2.43)$$

where M_0 is initial momentum, u_s is cross-flow velocity and C_s is a constant equal to 1.0.

An empirical equation developed by Socolofsky (2001), Equation (2.44), describes the same correlation. It yields an estimate of the characteristic length for phase separation in the jet/plume with cross flow conditions. The ambient density stratification is indirectly represented by u_s . The separation height, h_s , for oil droplets and gas bubbles from the plume, is described in terms of buoyancy flux, B , bubble rise velocity, u_s , and velocity, u_∞ , of cross-current (Johansen, 2003).

$$h_s = \frac{5.1B}{(u_\infty u_s^{2.4})^{0.88}} \quad (2.44)$$

where B is defined as:

$$B = V_G g' \quad (2.45)$$

where V_G is volume flux and g' is reduced gravity calculated by:

$$g' = \frac{g(\rho_w - \rho_G)}{\rho_w} \quad (2.46)$$

where g is the acceleration of gravity, ρ_w and ρ_G are densities of water and gas, respectively.

A gas bubble moves differently outside and inside of the jet/plume. Equation (2.47) describes the velocity of a gas bubble in mathematical terms.

$$\vec{V}_g = a\vec{V}_j + b\vec{V}_a + w_b\vec{k} \quad (2.47)$$

where \vec{V}_j is velocity of jet, \vec{V}_a is velocity of ambient flow and w_b is slip velocity. If the gas bubble is outside the plume after a very short transition period yields $a = 0$ and $b = 1$. If the gas bubble is inside the plume yields $a = 1$ and $b = 0$.

Usually two criteria are utilized to decide if the gas can separate from the main jet/plume. Firstly, there is no gas separation if $h < h_s$, meaning that the height must be larger than the critical height. Secondly, the angle at which the gas will travel immediately after escaping. If the angle is larger than the angle of the jet, the gas will escape from the jet/plume.

To test the model proposed by Zheng et al. (2002) the CDOG model was utilized. It simulates behaviour of oil and gas released from deep water, however the model still requires verification by comparison with experimental data. The numerical simulations from the CDOG model were compared with the DeepSpill field experiment. The comparison between the experimental data and the numerical simulations yielded results in accordance with theory. One exception was near the release point for oil and gas (Chen and Yapa, 2002).

2.2.6 CDOG and DeepBlow Model

A short description of the CDOG and the DeepBlow model are presented below.

2.2.6.1 CDOG

The CDOG model was developed at Clarkson University to simulate behaviour of oil and gas accidentally released at deep waters. The model is three-dimensional and includes additional processes, i.e. phase change of gas with associated change in thermodynamics and hydrodynamics of the jet/plume, hydrate formation and decomposition, gas dissolution, non-ideal behaviour of gas, and thermodynamics and hydrodynamics of the jet/plume (Yapa, 2013).

CDOG was utilized to analyze multiple deep water blowout scenarios. A summary of the results from the simulations are listed below (Yapa and Chen, 2004).

- Pure oil, i.e. untreated oil, released; ambient conditions do not affect surfacing time⁸. Location and size of oil slick are affected.
- Oil and gas mixes released; gas type do not affect the surfacing time, however it is dependent on ambient conditions.

⁸Time for the oil and/or gas to reach the seawater surface.

- Free gas did not reach the surface for any of the simulations.
- Changing the release temperature had almost no effect.
- Oil type and GOR affected the results.

2.2.6.2 DeepBlow

DeepBlow is a similar plume model based on the Lagrangian integral method which applies to multiphase discharges in the formation of oil, gas and water in a stratified water column with changeable currents. Non-ideal gas behaviour is included in the model by utilizing the compressibility factor, as presented earlier in Equation (2.30).

The results from the model are in accordance with field data from an experiment at 100 meters depth. When the dissolution of gases are included in the model, the results from the simulation are in accordance with both experimental data and droplet size distributions predicted by theory (Johansen, 2000).

2.3 Droplet Formation from Oil Jets

The following topics will be covered in the following; general theory for modelling of droplet formation from oil jets, a new prediction method for droplet size distribution and a couple of droplet size distribution functions.

2.3.1 Modelling of Droplet Size Formation

Today there is only a limited amount of experiments performed with jets in oil-water systems, especially in deep waters. It was one of the objectives for Masutani and Adams (2001), they wanted to conduct laboratory experiments that would support the already existing predictive models and possibly improve them as well. Experiments with four different crude oils was conducted. The effects of jet velocity, ambient and jet fluid properties on the breakup mechanism and the size distribution of droplets were observed (Masutani and Adams, 2001).

During the last years SINTEF has conducted numerous experiments with their Tower basin. They have tested different oil types at several temperatures and with different

dispersants. All the experimental data will improve the oil droplets size calculated by MEMW. The knowledge is important to obtain improved blowout models compared to the models existing today (Brandvik, Øistein Johansen, Angell and Leirvik, 2013).

The GOR is important to describe the properties of an underwater release. It has an impact on the gas volumes which affects the composite release velocities of the oil and gas mixture, especially at deep waters. The release velocity affects the the turbulence which influences the oil droplet size distribution. The surfacing time is again influenced by the oil droplet size (Yapa et al., 2012).

Another name for the droplet size distribution is the bubble size distribution, BSD. Bandara and Yapa (2011) found that breakup and coalescence are considered to be the most important processes that control the BSD in turbulent jets. A population balance equation was suggested to describe bubble volumes and it is utilized to model the evolution of bubble sizes caused by coalescence and breakup. Theory for bubble columns with coalescence and breakup rates are modified to fit for deep water plumes. Bandara and Yapa (2011) compares in addition simulated data with experimental data and found that the theory is in agreement with collected data. The simulations indicates that coalescence and breakup of bubbles are only significant during the first meters of the jet/plume, where turbulence is dominant (Bandara and Yapa, 2011).

An article by Chen and Yapa (2007) describes a method on how to determine the droplet size distribution of oil. A thorough summary of the maximum entropy formalism model is presented in Appendix A.1. Two types of constraint equations were utilized, i.e. the mass balance and the specific surface area. The constraint with specific surface area yielded results in agreement with both theory and experimental data.

There are few studies of droplet splitting in large volume oil jets released into water, however it is possible to utilize an analogy with splitting of droplets in a turbulent pipe flow. The maximum oil droplet size is related to the non-dimensional Weber number, We , at exit conditions of the pipe, see Equation (2.48) (Hinze, 1955; Johansen, 2003).

$$We = \frac{\rho U^2 d}{\sigma} \quad (2.48)$$

where U is initial velocity of jet, d is orifice diameter of nozzle. ρ is density of fluid in jet and σ is interfacial tension between the fluid in the jet and the continuous phase, e.g.

oil and water.

An empirical relation between the 95 % maximum droplet size, d_{95} , and the Weber number, valid for one liquid dispersed into another liquid in a turbulent pipe flow, is calculated by Equation (2.49).

$$d_{95} = c d We^{-0.6} \quad (2.49)$$

where c is an empirical coefficient. The best value for a pipe flow is found to be 4.0. However, the value is not necessarily correct for oil jets emerging into water. The estimated value, based on oil droplet size counts from video close-ups, was approximately 20 (Johansen, 2003).

2.3.2 Basis for a New Prediction Method for Droplet Size Distributions

SINTEF has developed a new prediction method for estimating droplet size distributions from subsea oil and gas releases (Johansen, Brandvik and Farooq, 2012). The method is developed with data from measurements with SINTEF's Tower basin, details for the Tower basin can be found in Brandvik, Johansen, Leirvik, Farooq and Daling (2012).

The fate of oil in the environment is affected by the droplet size distribution for oil droplets and gas bubbles, formed at large depths. Small droplets, with a diameter smaller than 0.5 mm, require approximately a day to reach the surface. Larger droplets, diameter larger than 5 mm, will reach the surface within a couple of hours after release. The approximated values is based on a 1000 meters depth. The smallest particles, below 100µm can be detained in the water column for a long period of time before they may reach the surface. In addition, other factors such as, cross flows, vertical turbulence mixing in the water column and density stratification can detain the smallest droplets for an even longer period of time (Brandvik et al., 2012).

Oil jets in water breakup regimes can be represented by the two dimensionless numbers, the Reynolds number, Re , in Equation (2.50) and the Ohnesorge number, Oh , in Equation (2.51). Re versus Oh predicts a relationship for different droplet breakup regimes.

$$\text{Re} = \frac{\rho U d}{\mu} \quad (2.50)$$

$$\text{Oh} = \frac{\mu}{(\rho \sigma d)^{1/2}} \quad (2.51)$$

where ρ is density of jet fluid, U is exit velocity, d is orifice diameter, μ is dynamic viscosity of jet fluid and σ is interfacial tension between jet fluid and continuous phase.

The Oh number can be defined as a function of We, earlier defined in Equation (2.48), and Re, defined above in Equation (2.50), to yield the following coherence in Equation (2.52).

$$\text{Oh} = \frac{\text{We}^{1/2}}{\text{Re}} \quad (2.52)$$

There is a boundary between transitional and turbulent or atomization⁹ breakup, see details in Johansen et al. (2012), which results in a constant We, i.e. We equal to c^2 . The constant is found to be 18, which yields a lower limit for turbulent breakup. It results in We equal to 324, and yield the lowest limit where there is still atomization of oil in the jet (Johansen et al., 2012).

A maximum stable droplet size, d_{\max} , from classical theory of droplet splitting in turbulence, is presented in Equation (2.53).

$$d_{\max} = a \left(\frac{\sigma}{\rho} \right)^{3/5} \epsilon^{-2/5} \quad (2.53)$$

where a is a constant of proportionality, σ is interfacial tension between oil and water, ρ is density of continuous phase, i.e. water, and ϵ is stationary turbulent dissipation rate.

In an oil jet released into water from a nozzle, oil droplets will be transported downstream in the jet during the splitting process. Thus, in Lagrangian framework, the turbulent dissipation rate will diminish rapidly with time. Thus, assuming stationary turbulence will not be correct. Still, the theoretical model may be a starting point for ex-

⁹Atomization is a process of breaking up a jet into droplets of diameter much smaller than the jet diameter (Lin and Lian, 1998).

perimental design and empirical equations. An example is presented in Equation (2.54), where the relationship with the exit turbulent dissipation rate, which scales with exit velocity, and diameter is accounted for (Johansen et al., 2012).

$$\frac{d_{\max}}{D} = AWe^{-3/5} \quad (2.54)$$

where D is diameter of nozzle and A is a factor of proportionality. The maximum diameter can be replaced by other characteristic diameters, e.g. the volume median diameter.

An equation that includes both viscous forces and interfacial tension influencing the droplet breakup, is presented in Equation (2.55). The equation, is an example where an other diameter than the maximum is utilized, was originally presented by Wang and Calabrese (1986).

$$\frac{d_{50}}{D} = AWe^{-3/5} \left[1 + BVi \left(\frac{d_{50}}{D} \right)^{1/3} \right]^{3/5} \quad (2.55)$$

where

$$Vi = \frac{\mu U}{\sigma} = \frac{We}{Re} \quad (2.56)$$

Vi is a dimensionless group named the viscosity number and B in Equation (2.55) is an empirical coefficient. For large Vi , Equation (2.55) can be approximated as:

$$\left(\frac{d_{50}}{D} \right)^{4/5} = AWe^{-3/5} (BVi)^{3/5} \quad (2.57)$$

By manipulations, Equation (2.57) can be expressed only by Re :

$$\frac{d_{50}}{D} = A^{5/4} B^{3/4} Re^{-3/4} \quad (2.58)$$

There are different flow regimes for multiphase flows. If the continuous phase is liquid, it is named bubble flow. If the continuous phase, is gas, it is named mist flow, meaning a high gas void fraction in the multiphase flow. Here, a bubble flow is assumed as it is the most probable for deep water oil well blowouts (Gould, Tek and Katz, 1974).

It is a challenge to understand how the normalized variables, such as Re , Oh and We numbers, include presence of gas. The presence of gas can be included by e.g. defining an effective water velocity, U_E , see Equation (2.59) and neglecting the contribution of gas to the momentum flux.

$$U_E = \frac{U}{(1-n)^{1/2}} \quad (2.59)$$

where n is the gas void fraction.

The velocity, U , is replaced with the effective water velocity, U_E , in the dimensionless variables to account for the presence of gas. The presence of gas has effects in the volume flow as well. By adjusting the volume flow with the void fraction of gas, a new adjusted volume flow will be obtained, as presented in Equation (2.60).

$$Q_E = \frac{Q}{(1-n)^{1/2}} \quad (2.60)$$

where Q is volume flow.

2.3.3 New Prediction Method for Droplet Size Distributions

Based on the experimental data in Johansen et al. (2012) the original representation of the We number does not fit the data for cases with oil with premixed dispersants. Experiments conducted in SINTEF's Tower basin resulted in a modified We number, We' , presented in Equation (2.61) (Johansen et al., 2012).

$$We' = \frac{We}{\left[1 + B \cdot Vi \left(\frac{d_{50}}{D}\right)^{1/3}\right]} \quad (2.61)$$

Hence, the equation for the volume median diameter is expressed as;

$$\frac{d_{50}}{D} = A \cdot (We')^{-3/5} \quad (2.62)$$

An implicit model for the predicted variable d_{50}/D is obtained and an iterative method is required in order to solve Equation (2.62). The model is valid for momentum jets and

single fluid releases. Releases with oil and gas requires additional correction, such as a void fraction. If there are large volume flows that could be buoyancy dominated, then a correction with the Froude number, Fr , should be included. The correction for the void fraction is presented in Equation (2.63) (Johansen et al., 2012).

$$U_n = \frac{U_{oil}}{(1-n)^{1/2}} \quad (2.63)$$

where U_{oil} is outlet velocity of oil only and n is gas void fraction at the exit of the nozzle.

A correction can be made for large volume flows that are buoyancy dominated, as presented in Equation (2.64).

$$U' = U_n(1 + Fr^{-1}) \quad (2.64)$$

where

$$Fr = \frac{U_n}{(g'D)^{1/2}}, \quad g' = g \frac{\rho_w - \rho_{oil}(1-n)}{\rho_w} \quad (2.65)$$

The corrected U' is inserted into the equation for the We number to calculate a corrected We' :

$$We' = \frac{\rho U'^2 d}{\sigma} \quad (2.66)$$

Finally, We' is inserted into Equation (2.62) to calculate d_{50} which yields the oil droplet size distribution.

2.3.4 Droplet Size Distribution Functions

The droplet size distribution function has also been called a probability density function, PDF. The PDF is dependent on the characteristic size in order to estimate the droplet size distribution for a blowout model. If there is a wide distribution of droplets, it is best described by mean diameters. Two common methods to present the droplet size distributions are by the Rosin-Rammler distribution function or by the log-normal distribution function (Johansen, 2003; Johansen et al., 2012).

The Rosin-Rammler distribution function is presented in Equation (2.67). It is defined by a characteristic diameter, d_i , that corresponds to a certain cumulative volume fraction, V_i , and a spreading parameter, α .

$$V(d) = 1 - \exp \left[-k_i \left(\frac{d}{d_i} \right)^\alpha \right], \quad k_i = -\ln(1 - V_i) \quad (2.67)$$

If $V_i = 50\%$, d_i is the median volume diameter with $k_i = -\ln(0.5) = 0.693$.

The log-normal distribution function is a normal distribution function of $x = \ln(d)$, with a mean value, $m = \langle x \rangle$, and a standard deviation, σ_x , based on x . The mean value is equal to the logarithm of the median volume droplet diameter, $m = \ln(d_{50})$. Only two parameters is required to calculate the log-normal distribution function, viz. m and σ_x .

2.4 Oil Chemistry

General properties, typical characteristics and weathering effects of crude oil will be discussed in the section to follow.

2.4.1 General Characterization of Crude Oils

Crude oils are complex mixtures that can contain thousand of chemical components. One crude oil is often significantly different from another crude oil. Crude oils are divided into chemical groups based on their characteristics, where the two main groups are hydrocarbons and organic non-hydrocarbons. These two groups are divided into smaller groups and presented in the list below (Sørheim, Leirvik and Brandvik, 2010b; Sørheim, Leirvik and Brandvik, 2010a).

- Hydrocarbons
 - Aliphatics: Paraffins and naphthenes
 - Aromatics
- Organic non-hydrocarbons
 - Resins

– Asphaltenes

Crude oil contains mostly hydrocarbons, consisting of approximately 85 to 90 wt% carbon, and 10 to 15 wt% hydrogen. The hydrocarbons found in crude oil ranges from the lightest and simplest molecules to more heavier, complex structures. The hydrocarbons appears as saturated molecules, with only single bonds, and unsaturated molecules, with multiple double or triple bonds.

For the aliphatic hydrocarbons, the most important groups are naphthenes and paraffins. Naphthenes are cyclic alkanes consisting of one or more saturated rings. Paraffins are n-alkanes, straight chained molecules, and iso-alkanes, branched molecules. Paraffins with more than 20 carbons are named wax and affect the crude oil properties significantly. Thus, the wax content in different crude oils affect the flow properties.

The aromatics is a type of unsaturated cyclic hydrocarbons with branched side chains or straight chains. Hence, they can have a large degree of isomerism.

Non-organic hydrocarbons contains oxygen, sulphur, nitrogen, and trace metals such as nickel, and vanadium, in addition to carbon and hydrogen. The resins are relatively polar compared to hydrocarbons and usually have surface active characteristics. Asphaltenes on the other hand are a group of complex molecules with undefined chemical structure and consist of condensed polycyclic aromatic compounds.

2.4.2 Classification of Oil Types

Before investigating the weathering, see Section 2.4.3, of oils it is useful to classify the petroleum products in three categories. They are categorized based on their evaporation, emulsion and spreading characteristics, and the categories are:

- **Condensate:** Does not contain heavier components; wax or asphaltenes. A condensate will not absorb water, also known as emulsifying, and it will spread over a large area. It will have an evaporation of approximately 70% at 250°C. A terminal film thickness in the order of 0.05 mm is predicted from earlier observations.
- **Light oil:** A definition utilized for weathering studies, usually it is included in the crude oil definition. It has a high content of lighter components. Evaporation of 50 to 70% at 250°C is typical, however it will contain heavier components than

condensate. It can emulsify and the emulsions formed are unstable. Light oil has a lower spreading than condensate and has a terminal film thickness in the order of 0.5 mm.

- **Crude oil:** Highest content of heavier components. An evaporation of 40–50 % at 250°C. Reduced spreading due to formation of water in oil emulsions. The terminal film thickness is at 1 mm water free oil, however it will vary for the characteristics of the emulsions.

2.4.3 Weathering of Crude oils at Sea

Weathering processes can cause changes in the physical characteristics for a crude oil. These processes occur when the crude oil is exposed to sunlight at sea. The most important are:

- Dispersion
- Emulsifying
- Evaporation
- Spreading on the sea surface

Figure 2.5 presents the weathering processes a crude oil is postponed to at sea.

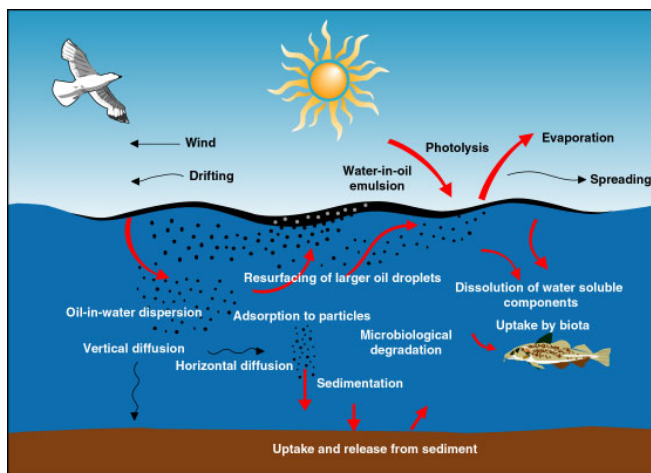


Figure 2.5: Weathering processes for crude oil in seawater, as presented Sørheim et al. (2010b).

There are several aspects affecting the oil's behaviour at sea. Three of them are:

- Physical and chemical properties of non weathered crude oil.
- Environmental conditions; e.g. current, wind, waves, temperature and sunshine.
- Characteristics of the water; e.g. density, salinity, oxygen content, temperature, bacterias, particles and nutrients.

2.4.3.1 Oil-in-water dispersion

It is common to distinguish between natural and chemical oil-in-water, O/W, dispersions. If breaking waves are present, usually occurring with wind speeds above 5 m/s, natural dispersion may happen. The oil will break into droplets of various sizes and mixed with the water masses. The effect will gradually decrease as the viscosity increases, mainly caused by emulsification.

The chemical oil-in-water dispersion is an important weathering process. It occurs when chemical dispersants are added to an oil and water mixture. The dispersion process can be divided into three separate processes. First, initial globulization where formation of oil droplets take place under the influence of wave action. Secondly, water column transport due to the kinetic energy of oil droplets supplied by buoyancy forces and wave

action. Thirdly, coalescence of oil droplets (Sterling Jr., Bonner, Ernest, Page and Autenrieth, 2004)

2.4.3.2 Water-in-oil emulsion

Water-in-oil, W/O, emulsions decrease the evaporation rate of oil, causing increasing viscosity for the oil, and limits the natural dispersion of oil in water. W/O emulsions are promoted by breaking waves as they require an energy supply. Crude oil has an absorption level of 30 to 80 % water. Wind speed will in addition affect the water absorption level.

W/O emulsions can be divided in different classes of stabilities dependent of the asphaltene content. A division between mesostable, stable and unstable emulsions are a common way to classify the emulsions (Fingas, Fieldhouse and Mullin, 1996).

The rate of emulsion formation and the rheological properties of the emulsion are dependent of the release conditions and physico-chemical¹⁰ properties of oils that control the initial film thickness (Daling, Moldestad, Johansen, Lewis and Rødal, 2003).

Asphaltenes, resins and wax are important compounds for stabilizing W/O emulsions. Asphaltenes and resins are surface active compounds with hydrophobic and hydrophilic characteristics. These will be found at the boundary layer between oil and water, and form a boundary surface film. The asphaltene's hydrophobic characteristics can result in an increased concentration of wax around the oil droplet causing a larger boundary surface film between oil and water. The boundary surface film acts as a physical barrier towards coalescence.

2.4.3.3 Evaporation

The evaporation rate is dependent on spreading of oil, amount of light components in the oil, wind speed and sea temperature. A rule of thumb is that components with boiling point below 200 °C evaporates within 12–24 hours at sea. Components with boiling point below than 270 °C will evaporate completely from the sea surface within a few days.

The boiling point curve, also called the distillation curve, is a curve where the cumulative

¹⁰Relating to physics and chemistry or to physical chemistry

percentage or percentage volume is a function of temperature. It is based on measurements of evaporation temperature as a function of the amount of distillate.

2.4.3.4 Additional weathering effects

Additional weathering effects that can affect the oil are listed below, however they will not be described in detail here. See e.g. (Sørheim et al., 2010b) for more details.

- Solubility in water
- Photo oxidation
- Biodegradation
- Sedimentation
- Submergence or “over-washing”
- Spreading

2.4.4 Physical Characteristics of Oil

The most important physical characteristics to consider when dealing with releases of oil are listed below.

- Viscosity
- Pour point
- Density
- Flame point

Viscosity is a measure of a liquid’s resistance to flow as a function of temperature. To relate measurements from the laboratory with actual conditions at sea, it is common practice in Norway to perform viscosity measurements at 5 °C and 13 °C, which are the winter and summer temperature in the North Sea, respectively. Viscosity of the oil will increase with increasing evaporation (Sørheim et al., 2010b).

The viscosity is sensitive to temperature change and reduces logarithmically with increasing temperature. For Newtonian fluids, the viscosity is independent of shear rate.

It is the case for light, water free crude oils. For non-Newtonian fluids, the viscosity reduces with increasing shear rate. It is the case for very viscous and wax-rich oils. The phenomena is also called sheer thinning and is applicable the pour point. A method for calculating the shear rate inside a pipe for a Newtonian fluid is presented in Appendix A.2 (Darby, 2001).

Water-in-oil emulsions are usually more viscous than the oil residue which constitutes the continuous phase. It is important to obtain more knowledge of these emulsions as it can be utilized understand oil spills at sea with weathered oils.

The pour point is defined as the temperature where oil stops flowing, when cooled under specified conditions in the laboratory. However, the measurement is often inaccurate compared to the pour point under actual conditions at sea. The pour point is dependent of the chemical composition of the oil, where the wax content is of special importance. A partially or completely solidified oil will limit the dispersant effectiveness, thus pour point is a limiting factor for chemical dispersion of wax-rich oils.

Density is defined as the mass of a substance per unit volume (Green and Perry, 2007). Other representations of density are relative density and API, see below. The definition of relative density is the relation between the densities at 15.5°C of an oil and distilled water. American literature often represent density as ° API. It is calculated by Equation (2.68) (Green and Perry, 2007).

$$^{\circ}\text{API} = \frac{141.5}{\text{Relative density}} - 131.5 \quad (2.68)$$

Low density oils often contain components with lower molecular weights, such as paraffins, while oils with a high degree of asphaltenes have a higher density. The density of emulsions increases with water content.

Flame point is the lowest temperature where vapour generated, by heating of the oil, can be ignited by a flame. The flame point is dependent on the chemical composition of crude oil and is often lower for fresh crude as light components are still present. Evaporation will occur gradually, thus the flame point will increase with time. Flame point is utilized as an indication for the explosion risk (Sørheim et al., 2010a).

Flame point to the oil affect the ignitability of the air above an oil slick, however there are other factors that has an impact. Such as weather situation, e.g. calm sea and high temperature will lead to a high concentration of ignitable gases above the oil slick. Strong wind will thin out the concentration of ignitable gases relatively quickly.

2.5 Interfacial Tension and Dispersants

O/W dispersions are strongly promoted by addition of chemical dispersant. The dispersant reduces the interfacial tension, IFT, between oil and water. In an effective chemical dispersion, small droplets are formed in the range from 5 to 10 μm (Sørheim et al., 2010a). Another definition of dispersant is; a formulation containing surfactants as active ingredients (Brown, Challenger, Etkin, Fingas, Hollebone, Kirby, Lamarche, Law, Mauseth, Michel, Nichols, Owens, Quek, Shigenaka, Simecek-Beatty and Yender, 2011).

When evaporation has caused the pour point to increase in size, the oil can be difficult to disperse. Experiments in the laboratory have shown that oil can be dispersible at a temperature between 10 to 15 °C below the pour point of the oil (Sørheim et al., 2010a). An upper viscosity limit, if the application of dispersants should be effective, is in the range 2000 to 30 000 mPa s, depending on the oil type.

In Figure 2.6 three different dispersant-to-oil ratios, DOR, are illustrated by pictures of arbitrary oil.

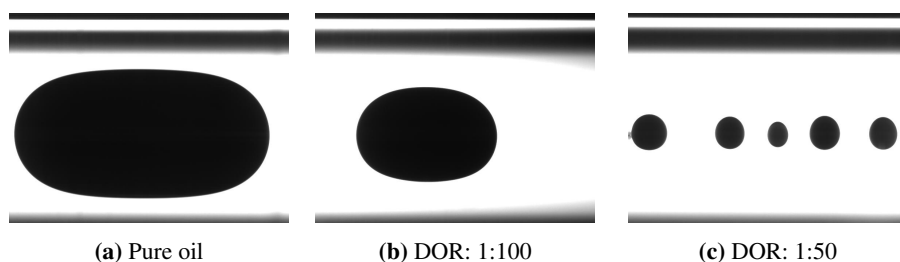


Figure 2.6: Oil droplets of an arbitrary oil with three different DOR. Pictures are taken with the spinning drop video tensiometer during IFT measurements (Farooq, SINTEF, 2013).

Dispersants can remove oil from the water surface and mix it into the water column. It will then increase the total hydrocarbon concentration, THC, in the water column. The dissolved hydrocarbon concentration may also increase when dissolution of water-soluble components from the oil droplets occurs. An increase in the potential for toxic effects is a plausible outcome (Daling, Singsaas, Reed and Hansen, 2002).

IFT is nearly the same as surface tension, however cohesive forces are included in the definition of IFT (Agrawal, 2013). Another definition of IFT is; a measurement of the cohesive or excess energy present at an interface arising from the unbalance of forces between molecules at an interface (Attension, 2012). Another difference between interfacial and surface tension are the phases present. IFT is between two immiscible liquids, while surface tension is between a gas and a liquid (Attension, 2012).

For the O/W dispersion it is important to have a positive spreading coefficient to promote the dispersion of oil in water. The derivation of the spreading coefficient can be found in Hiemenz and Rajagopalan (1997).

Chemical dispersants increase the natural process of dispersion by forming smaller oil droplets. These oil droplets can be mixed into the water column by wave energy. A typical chemical dispersant consists of a mixture of three different chemicals (United States Government Accountability Office, 2012):

- **Surfactants:** Active agents reducing oil-water IFT. Both water-compatible, hydrophilic, and oil-compatible, hydrophobic or lipophilic, groups on the same molecule.
- **Solvents:** Added to promote the dissolution of the surfactants and additives into the dispersant mixture. Reduces the viscosity of the oil (Committee on Effectiveness of Oil Spill Dispersants, 1989).
- **Additives:** Increase the long term stability of the dispersant formula and improve the dissolution of surfactants.

There is today limited knowledge of utilizing dispersants at large depths, where the pressure is high and the temperature is low. Valuable knowledge was obtained during the Deepwater Horizon spill that occurred at 1500 meters. Dispersants was utilized at the well head, thus the oil was broken into smaller droplets further down in the water

column. One of the conclusions from the spill is; more knowledge is required at larger depths to be able to understand the processes occurring in deep waters. (Thibodeaux, Valsaraj, John, Papadopoulos, Pratt and Pesika, 2011). It is especially the dispersant concentrations and DOR that requires further testing in deep water with respect to toxicological impacts (Kujawinski, Soule, Valentine, Boysen, Longnecker and Redmond, 2011)

One method utilized to classify surfactants, the main ingredient of the dispersant, is by the hydrophilic-lipophilic balance, HLB. To determine the size of the HLB, theoretical equations are utilized where the length of the water soluble portion is related to the oil soluble portion of surfactant. Dispersants are in the range of eight to twelve for the HLB. The range can promote both W/O emulsion, HLB between one and eight, and O/W emulsion, HLB between twelve and twenty. However, it most often promotes O/W emulsions (Brown et al., 2011). The HLB can be utilized to determine the effect of salinity on dispersant performance, since hydrophobic portions of the surfactant molecule tend to be salted out (Committee on Effectiveness of Oil Spill Dispersants, 1989).

A large part of the knowledge, on how and why dispersants work, are based on observations and empirical tests during sea trials and in the laboratory. Most of the studies with dispersants are performed with commercially available products, however there are few studies investigating the interactive phenomena of surfactants, water and crude oil (Committee on Effectiveness of Oil Spill Dispersants, 1989).

If the concentration of surfactants increases, the IFT between oil and water will decrease until a critical micelle ¹¹ concentration, CMC, is reached. There is little change in IFT above the CMC. Additional surfactant only form new micelles. Below the CMC, additional surfactant molecules accumulate at the oil-water or water-air interface (Committee on Effectiveness of Oil Spill Dispersants, 1989).

The main purpose with application of dispersants on an oil spill is to lower the oil-water IFT in order to enhance entrainment of small oil droplets into the water column at lower energy inputs. The oil-water interfacial area is increased with entrainment of small oil droplets into the water column. The process requires mixing energy as described with Equation (2.69) (Committee on Understanding Oil Spill Dispersants: Efficacy and

¹¹Micelles are ordered aggregates of surfactant molecules. With the hydrophobic portions of the molecules together at the interior of the micelle and the hydrophilic portions facing the aqueous phase (Hiemenz and Rajagopalan, 1997; Committee on Effectiveness of Oil Spill Dispersants, 1989).

Effects, 2005).

$$W_K = \gamma_{o/w} A_{o/w} \quad (2.69)$$

where $\gamma_{o/w}$ is oil-water IFT and $A_{o/w}$ is the interfacial area.

A reduction in the oil-water IFT will result in an increase in the interfacial area for the same energy input. Equation (2.69) provides an estimate for the minimum energy required to disperse oil as droplets in the water column (Committee on Understanding Oil Spill Dispersants: Efficacy and Effects, 2005).

Khelifa, Fingas, Hollebone and Brown (n.d.) showed that there exists an optimum DOR where the IFT reduction reaches a maximum value. The effectiveness of the chemical dispersant will be at the maximum at the optimum DOR. Another paper has found that change in DOR and mixing energy does not affect the correlation between viscosity and oil droplet size distribution. More viscous oil produce larger droplets than less viscous oils. Another characteristic, higher dispersant concentration favoured formation of smaller droplets (Mukherjee and Wrenn, 2011).

In Appendix A.3 seven requirements for a chemical dispersant to enhance the formation of oil droplets are presented. They are the same as found in Committee on Understanding Oil Spill Dispersants: Efficacy and Effects (2005) and are based on a report from Committee on Effectiveness of Oil Spill Dispersants (1989).

Strøm-Kristiansen, Daling, Hokstad and Singsaas (1997) has performed a weathering and dispersion study on three crude oils, where the waxy Norne is of special interest for the thesis. The results shows that fresh Norne crude oil at 3 °C could not be chemically dispersed. After emulsification with water, the crude oil was dispersible. Norne is a crude oil with high viscosity, approximately 2000 mPas, and this type of high viscosity crude oil was considered very difficult or impossible to chemically disperse in the 1980s. Recent studies, both in the laboratory and in the field, have shown that oils with viscosity up to 20000 mPas could be chemically dispersed with newer dispersants, e.g. Corexit 9500 and Slickgone NS (Committee on Understanding Oil Spill Dispersants: Efficacy and Effects, 2005).

2.6 Marine Environmental Modelling Workbench

The simulation software utilized in the Master's thesis is a simulation model developed by SINTEF named Marine Environmental Modeling Workbench, MEMW. In the following, an explanation of the main features of the software are presented.

MEMW is a framework for performing analysis, simulations and presentation tasks. These tasks are related to releases to the marine environment. MEMW utilizes different numerical models such as (SINTEF Marine Modeling Group, 2012):

- OSCAR: Oil spill contingency and response
- DREAM: Dose-related risk and effects assessment model
- ParTrack: Particle tracking for drilling discharges

In the thesis, two versions of MEMW will be utilized. MEMW v6.2 with the old droplet size distribution equation and MEMW v6.5 β where an improved equation for droplet size distribution is implemented. The two versions of MEMW will be compared to each other. Figure 2.7 presents a snapshot of the MEMW's interface for an arbitrary simulation.

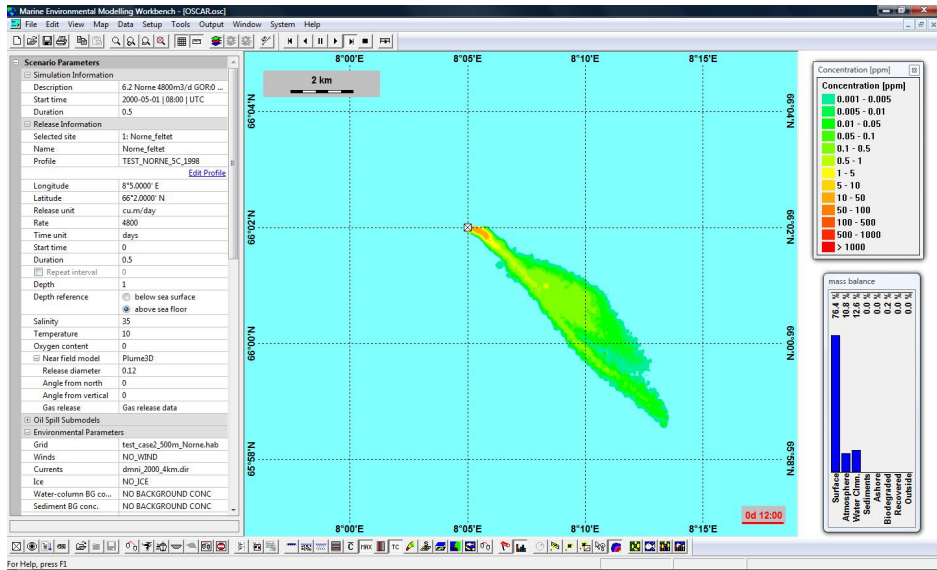


Figure 2.7: Snapshot of MEMW for an arbitrary simulation.

A review of the oil spill models existing in 2000, and the important parts implemented in these models can be found in Reed, Johansen, Brandvik, Daling, Lewis, Fiocco, Mackay and Prentk (1999). There exist few models concerning the impact oil spills will have on aquatic organisms and habitats, however one such model is described by French-McCay (2004).

2.6.1 Plume3D

Plume3D is a stand-alone general multiphase plume model developed from SINTEF's DeepBlow model. Near-field far-field coupling and far-field tracking for dispersed droplets, bubbles and mineral particles are also included in Plume3D. The model is utilized in MEMW to account for the formation of the multiphase plume from the discharge of oil and gas from the sea bed (Johansen and Durgut, 2006).

Plume3D has advantages of including separation of oil droplets and mineral particles from the plume. Drift and fate of separated gas bubbles in the far-field. The Plume3D

model includes several processes to be able to simulate a deep water plume, as listed below (Johansen and Durgut, 2006).

- Non-ideal gas behaviour
- Dissolution of gas from bubbles to ambient water
- Effects of cross currents
- Formation and dissociation of gas hydrates

3 Assumptions

The computer simulations will be performed with MEMW v6.2 and MEMW v6.5 β . The location of the subsurface blowout of oil and gas will take place at the Norne field, located at the Norwegian continental shelf approximately 200 kilometers from the Norwegian coast, see Figure 3.1. The exact location of the blowout is determined to be $66^{\circ}2'N$ $8^{\circ}5'E$.

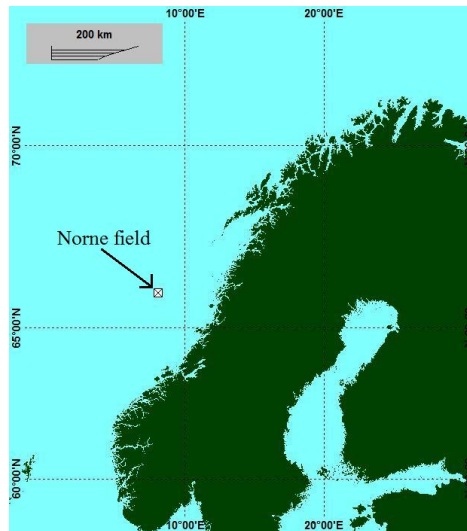


Figure 3.1: Location of the Norne field with coordinates $66^{\circ}2'N$ $8^{\circ}5'E$, at the Norwegian continental shelf from MEMW.

3.1 Information from Simulations

The discharge depth for the blowout is at 367.2 meters below the sea surface, 1 meter above the sea bed. A detailed description over the input data to MEMW is found in Appendix B.1. The most important assumptions for the simulations are summarized in the following list.

- Simulation time will be twelve hours. Data will be collected after ten hours¹².
- Default release rate of oil will be $4800\text{m}^3/\text{d}$.
- Three different oil types will be utilized; Alve, Norne and Sval.
- Release diameter of the nozzle is 120mm.
- GOR is varied between 0, 100, 200 and 400.
- IFT for pure oil: 20mN/m .
- IFT for oil with dispersant: 0.1mN/m .

A plume of a subsurface release with pure oil is depicted in Figure 3.2. The red box in the figure indicate the region of interest which is the plume. Figure 3.3 depict an example of the maximum concentration in the whole water column for a subsurface release of pure oil. The figure is similar to the outcome of the simulations in Section 5 Results. These figures are presented here to illustrate possible outputs from MEMW.

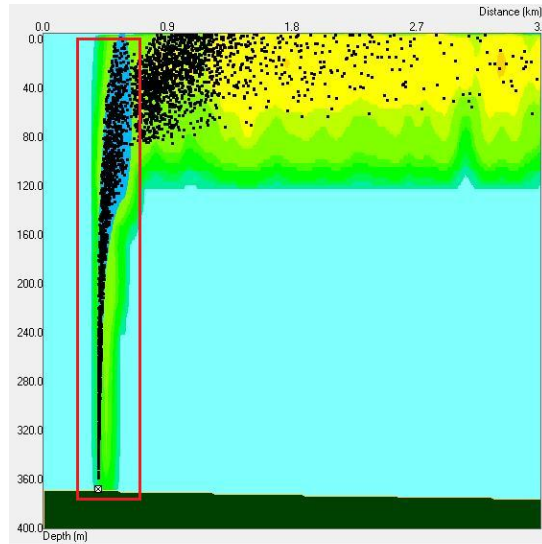


Figure 3.2: Vertical cross-section of a subsurface plume from MEMW. Red box indicates region of interest.

¹²The simulation data is collected before end of simulation to avoid influence by other factors. It was observed during the test simulations and therefore the results are collected before the simulations ends.

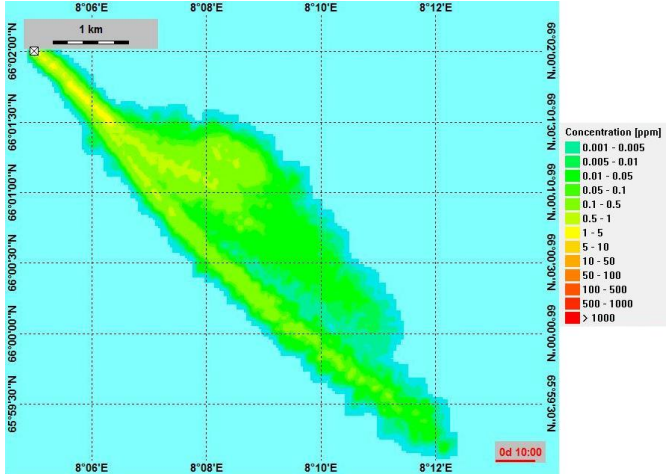


Figure 3.3: Illustration of maximum concentration of oil in the water column, output from MEMW.

The simulation results presented in Section 5 Results are the droplet size distribution for a release of pure oil or oil and gas. The default oil type utilized for simulations is Alve with a default flow rate of $4800\text{m}^3/\text{d}$.

The minimum droplet size bin for MEMW v6.2 is ten μm , while for the MEMW v6.5 β the minimum is one μm . The maximum droplet size, d_{max} , is calculated in MEMW after a method by Hu and Kintner (1955) and droplets larger than d_{max} are exposed to secondary droplet splitting. The large droplets are broken down into smaller and more stable droplets. The maximum droplet size, also called critical, follows the criteria of $(C_D We)$ equal to a constant. Hence, an equation for estimating the critical droplet size is found. It is dependent on the density difference and IFT of a system, e.g. oil and water (Hu and Kintner, 1955) Another empirical relation for determining maximum droplet size is presented in (Ceylan, Kelbaliyev and Ceylan, 2003).

3.2 Properties of Crude Oils

Three oil types, Alve, Norne and Svale, from the Norne field will be utilized in the experimental part of the work, hence they will also be utilized in the modelling part.

Table 3.1 presents the most important physical properties of the three oils.

Table 3.1: The most important physical properties of Alve, Norne and Svale.

Oil types (Fresh)	Density [g/mL]	Viscosity [mPa s]	Pour point [°C]	Flame point [°C]	Wax [wt%]
Alve	0.796	12.5 [*]	0	-	5.0
Norne	0.863	1968 [†]	21	-	13.0
Svale	0.914	257 [*]	-33	13	2.12

^{*} Viscosities are found in SINTEF's oil database and are earlier measured in the laboratory, at shear rate of 10 s^{-1} at 5°C .

[†] Viscosity is found in SINTEF's oil database and is earlier measured in the laboratory at shear rate of 10 s^{-1} at 13°C .

4 Experimental Work

The laboratory part of the Master's thesis was experiments conducted with the SINTEF MiniTower. In addition, IFT and viscosity measurements were performed. The particle size analyzer utilized in the MiniTower, a detailed description of the MiniTower and an experimental procedure are described in the following.

4.1 Particle Size Analyzer

A particle size analyzer, LISST-100X¹³, by Sequoia Scientific Inc. is utilized to measure the particle size distributions for the laboratory experiments. The LISST-100X utilizes laser diffraction, with a 670 nm laser, to obtain particle size distributions, PSDs. Laser diffraction is not affected by composition of particles because the scattering of laser light is observed at multiple, small forward angles (Agrawal and Pottsmith, 2000; Sequoia Scientific, Inc., 2012).

The LISST-100X records pressure, temperature and optical transmission as well. If desirable, a path reduction module can be attached to the instrument to reduce the measurement volume (Sequoia Scientific, Inc., 2012). It is the case for the LISST-100X utilized in the laboratory experiments and has a measuring volume with one centimeter in diameter.

The LISST-100X records scattering intensity over a range of small angles with a specially constructed multi-ring detector, see Figure 4.1 for internal details of the LISST-100X. The multi-ring detector consists of 32 logarithmically placed rings. Conversion from the multi-angle scattering to a PSD is performed with a mathematical inversion (Sequoia Scientific, Inc., 2012).

The LISST-100X was a type C which measures particle sizes from 2.5 μm to 500 μm . If the particles are larger than the upper range of the instrument, 500 μm , the inversion will continue to produce particle size distributions where the peaks vary between 250 μm and 400 μm . The phenomena is caused by the principal peaks in the scattering that are moving off the inside of the ring detectors. The remaining peaks in the scattering are

¹³LISST is short for **L**aser **I**n-**S**itu **S**cattering and **T**ransmissometry.

interpreted as the principal peaks and will yield a PSD within the range of the LISST-100X (Davies, Nimmo-Smith, Agrawal and Souza, 2012; Agrawal and Pottsmith, 2000).

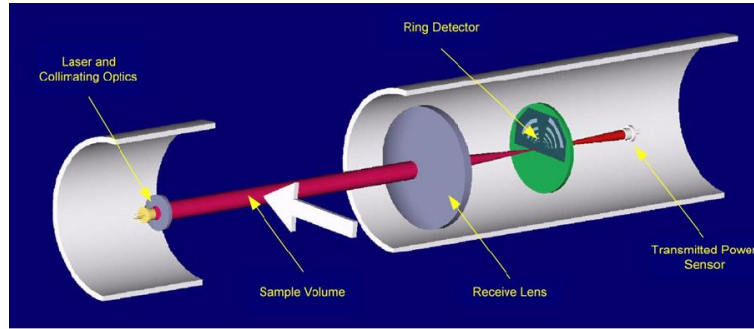


Figure 4.1: Overview of the inside of the LISST-100X by Sequoia Scientific, Inc. (2012). The collimated laser enters the sample volume and light is scattered by particles by the multi-ring detector behind a receiving lens. A photodiode, behind a centered hole, measures optical transmission.

4.2 SINTEF MiniTower

To measure the particle size distributions with the LISST-100X, SINTEF's new Mini-Tower was utilized. A schematic diagram over the MiniTower is presented in Figure 4.2. The left side of the figure depicts an overview of the most important parts and the dimensions of the MiniTower. While the right side of the figure depicts a detailed picture of the nozzle, which has a diameter of 0.5 mm. The dispersant is mixed with the oil six nozzle diameters below the nozzle tip, see right side of the figure. To create a constant laminar seawater flow through the whole MiniTower, many small inlet holes for seawater is placed in the bottom of the tower to distribute the flow evenly.

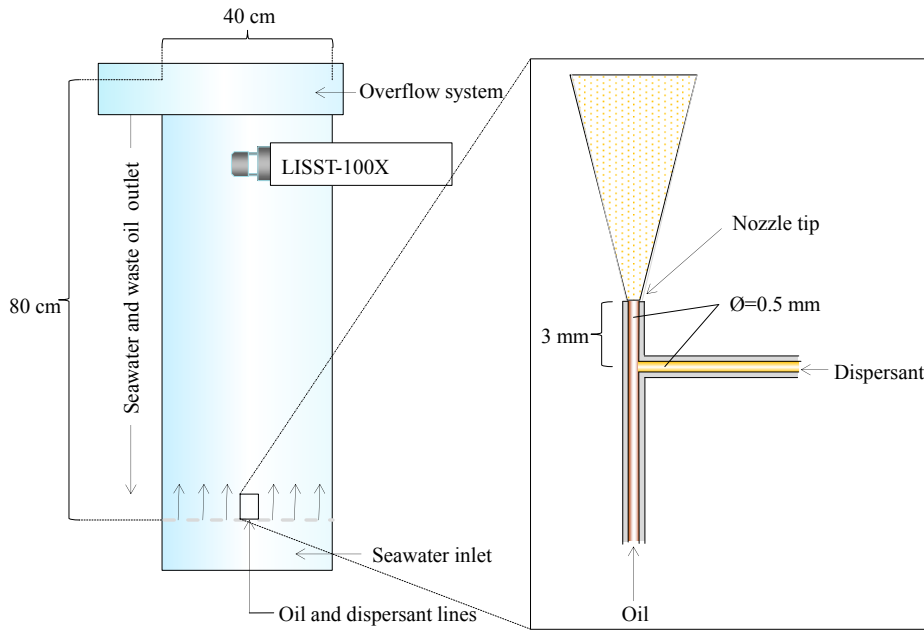


Figure 4.2: Schematic diagram over the SINTEF MiniTower setup (Leirvik, SINTEF, 2013).

Figure 4.3 depict the MiniTower, with the LISST-100X, utilized in the experiments.



Figure 4.3: Close-up of SINTEF MiniTower (Lindersen, 2013).

A close up of the placement of the LISST-100X in the MiniTower is depicted in Figure 4.4.

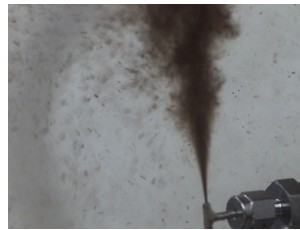


Figure 4.4: Placement of LISST-100X in the MiniTower (Lindersen, 2013).

In Figures 4.5a and 4.5b the jet of two different oil types, Norne and Svalde, utilized in the experiments are depicted. Figures 4.6a and 4.6 depicts an oil plume and an oil plume mixed with dispersant in the MiniTower, respectively.



(a) Norne



(b) Svalde

Figure 4.5: Oil jet from nozzle in the MiniTower for two of the oils (SINTEF, 2013).



(a) Oil plume



(b) Oil mixed with dispersant plume

Figure 4.6: Illustration of an oil plume and an oil plume mixed with dispersant (Brandvik, SINTEF, 2013).

4.3 Description of a MiniTower Experiment

A short description of the procedure for performing experiments with the MiniTower can be summarized as follows:

1. Make sure the drainage is open. Open seawater and fresh water inlet to the system.
2. Check that all equipment has connection with the software.
3. Determine test conditions, flow rates and duration of fluids.
4. Check background values for the LISST-100X and perform a background scatter in seawater with the LISST SOP software.
5. Prepare all data collection systems.
6. Initiate experiment, start release of relevant fluids, such as; oil, gas and dispersant.
7. Monitor the plume and record the oil droplet size distribution with the LISST-100X. The LabVIEW¹⁴ software will record a log file with flow rates for the different fluids.
8. Stop the release.
9. Initiate washing cycle with nozzles with hot fresh water for cleaning the Mini-Tower.
10. Collect data and make an initial quality control of them.

After the procedure is performed, the MiniTower is ready for new experiments. It is possible to run experiments over a long time period since the seawater is flowing continuously with drainage on the top.

The dispersant can be injected into the oil flow with two different methods:

- Simulated insertion tool. The dispersant is injected six nozzle diameters below the tip of the nozzle.
- External insertion tool. The dispersant is injected horizontally into the rising plume. It can be placed at different distances above the nozzle tip.

¹⁴LabVIEW system design software is utilized to control the MiniTower and measure the flow rates of seawater, oil, gas and dispersant.

For the laboratory experiments only the simulated insertion tool will be considered. The reason for utilizing different insertion techniques are to investigate if the reduced IFT is affected with different methods of injection of dispersant (Brandvik et al., 2012). Figure 4.7 depicts the two insertion techniques of dispersant presented above.

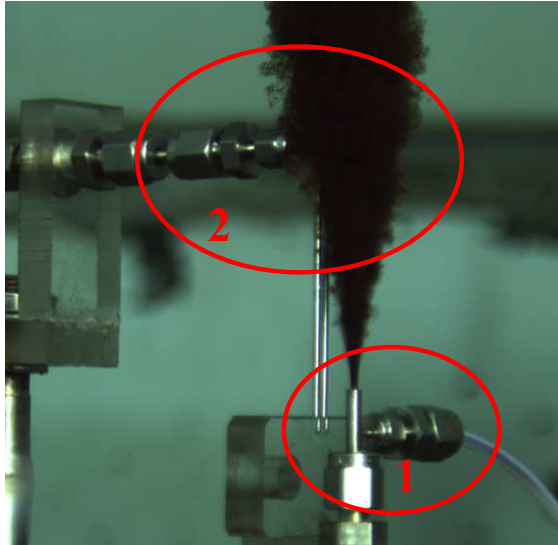


Figure 4.7: Release arrangement in SINTEF's Tower basin where 1 is the simulated insertion tool and 2 is the external insertion tool. Illustration with an arbitrary pure oil release (Brandvik et al., 2013).

To obtain reliable and stable data the oil plume will be held at one specific experimental condition for one minute. A new experimental condition can be initiated afterwards, e.g. change from pure oil to oil mixed with dispersant. Corexit 9500 will be the utilized dispersant. The data from the last 20 seconds of each run will be averaged to construct graphs of the respective oil droplet distributions.

The measured data from the LISST-100X are presented as volume fractions of oil as a function of droplet size. The droplet sizes are divided into 32 size ranges or bins that are evenly distributed on a logarithmic scale, ranging from 2.5 to 500 μm . Data in the three first bins have been omitted from the results due to influence from non-oil particles or possible background noise. As the upper limit for detection of droplets is 500 μm ,

it is possible that a significant number of droplets are not measured or interpreted as droplets with a smaller diameter. This phenomena is described more closely by Davies et al. (2012). Therefore, the characteristic droplet diameter is defined as center of the bin with peak to the distribution. Assuming that the droplet size distribution follows a log normal distribution, the peak diameter will coincide with the volume median droplet size with the uncertainty presented by the finite bin size. However, this may not be true for other distributions (Brandvik et al., 2012). The details for the case mentioned here, is discussed in more detail in (Johansen et al., 2012).

4.4 Interfacial Tension Measurements

IFT measurements, of the fresh crude oils and premixed fresh crude oils with dispersant, is performed by the spinning drop method¹⁵. The Spin Drop Video tensiometer, SVT 20N, from Dataphysics Instruments is utilized together with calculation and control software SVTS 20 IFT. To be able to control the temperature at 13 °C, the Julabo F12-ED Refrigerated and Heating Circulator is utilized. To inject the the oil sample into the SVT-20N capillary tube, a 1 mL disposable syringe will be utilized.

The capillary tube will be cleaned thoroughly before each measurement. First, it will be rinsed two times with dichloromethane, DCM, acetone and deionized water. Secondly, the capillary is dried with nitrogen gas and finally, it will be rinsed two times with seawater. The empty capillary tube is carefully filled with seawater to avoid air bubbles and the open side of the capillary is then closed with a septum. The closed capillary is inserted into the measuring cell. The oil sample is injected and the measurement of the IFT begin with a rotating measuring cell. The procedure is based on literature from Brandvik et al. (2012).

¹⁵A method for surface and IFT determinations. A small bubble/droplet of an immiscible gas or liquid, "A" suspended in a liquid "B", is rotated around a horizontal axis. Thus, the centrifugal forces will force "A" to an equilibrium position and migrate towards the center forming a bubble/drop astride the spinning axis. When the centrifugal forces reaches a certain value, the bubble/droplet becomes cylindrical(Viades-Trejo and Gracia-Fadrique, 2007).

4.5 Quality Assurance and Calibration

Quality assurance of experimental data, as well as simulated data, is crucial for the credibility of the obtained data. The nozzle of 0.5 mm in the MiniTower is earlier utilized by SINTEF and the droplet sizes produced are in accordance with Brandvik et al. (2013).

The simulated data can be quality assured by comparing them to earlier verified simulations. If the simulated data is verified, the results are easier accepted.

Calibration of instruments utilized in the laboratory experiments are important to perform in order to obtain quality assured data. In section 5.2.1 a calibration of the LISST-100X is performed with two sizes of monodisperse particles. The monodisperse particles have two different sizes, 80 μm and 346 μm , to verify the accuracy of the LISST-100X.

5 Results

The result section consists of four parts; results from simulations with the two versions of MEMW, i.e. existing v6.2 and new v6.5 β , laboratory experiments, IFT measurements and up-scaling of laboratory data to full scale.

5.1 Simulations with MEMW

The simulation part is divided into five different topics:

- Comparison of oil types
- Flow rate
- Effect of gas
- Effect of dispersant
- Change in DOR

5.1.1 Comparison of Oil Types

The three different oil types utilized in the simulations, Alve, Norne and Svale were compared to each other with MEMW v6.2 and MEMW v6.5 β . The results are depicted in Figure 5.1. Table 5.1 presents d_{95} and the peak values, d_{\max} , from the figure. The default flow rate was found to be 4800 m³/d, it was concluded after preliminary simulations with different flow rates were compared against d_{95} and d_{\max} values. It was desirable to have a d_{95} 50% lower than d_{\max} for the default simulation base case. Then the oil droplet size distributions would be based on d_{95} and not d_{\max} . In Appendix C.1, Figure C.1, d_{95} and d_{\max} are plotted as functions of flow rate.

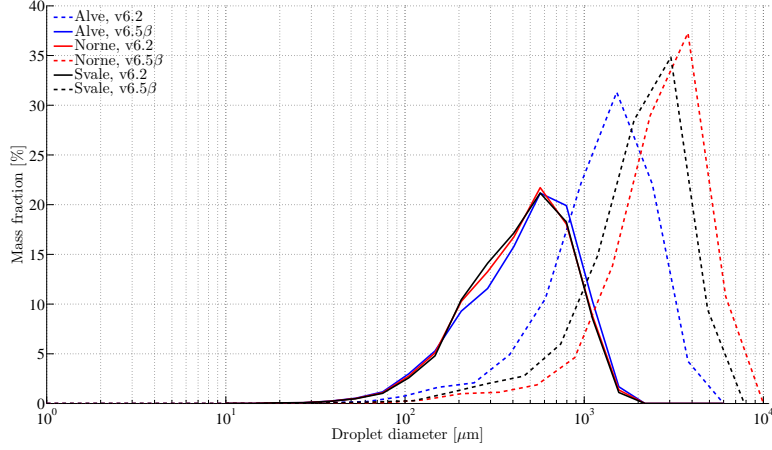


Figure 5.1: Oil droplet size distributions for Alve, Norne and Svale. Utilized for comparison between the three oil types. Simulations with MEMW v6.2 are showed with solid lines and simulations with MEMW v6.5 β are showed with dashed lines.

Table 5.1: Droplet sizes calculated for the comparison of oil types. The peak value, d_{peak} , and d_{95} are presented for MEMW v6.2. The same values are presented for MEMW v6.5 β together with the maximum stable droplet size, d_{max} . All droplet sizes in μm .

Oil type	MEMW v6.2		MEMW v6.5 β		
	d_{peak}	d_{95}	d_{peak}	d_{95}	d_{max}
Alve	568	1891	1519	4640	8630
Norne	568	1891	3793	10003	10003
Svale	568	1891	3046	7827	10719

Three different values for the viscosity is utilized to obtain the results. The values are presented in Table 5.2. The first column presents the values found in the oil database at SINTEF, which is utilized as input to the simulations with MEMW. The second column presents values calculated by MEMW v6.5 β . The third column presents values newly measured at SINTEF's laboratory without the correct pre-treatment¹⁶ procedure.

¹⁶SINTEF standard pre-treatment procedure for viscosity measurements are to keep the oils in the same temperature as the experimental temperature for approximately twelve hours. Before the experiments, presented in the thesis, they were only kept at 13 °C for one hour.

Table 5.2: Viscosity for the three different oil types calculated by MEMW v6.5 β compared to the earlier measured, input to MEMW, and the recently measured in the laboratory.

Oil type	Viscosity [mPa s]		
	Measured*	Calculated [†]	Measured [‡]
Alve	12.5	16.4	2.3
Norne	1968	8700	880
Svale	257	254	136

* Found in SINTEF's oil database as input to MEMW. The viscosities are measured earlier in the laboratory with shear rate 10 s^{-1} . Svale and Alve is measured at 5°C , while Norne is measured at 13°C due to the high wax content, hence the high pour point.

[†] Values are calculated by MEMW v6.5 β .

[‡] Recently measured in the laboratory with shear rate 10 s^{-1} at 13°C . The oils were not pre-treated after standard procedure, however the results are more close to the conditions in the MiniTower.

5.1.2 Flow Rate

Flow rates of 4800 , 7200 and $9600 \text{ m}^3/\text{d}$ were tested to see similarities and differences between MEMW v6.2 and v6.5 β . A few simulations of a flow rate of $2400 \text{ m}^3/\text{d}$ was performed, however the results did not meet the criteria of $d_{05} < d_{\max}$. The results from the simulations with multiple flow rates for Alve are depicted in Figure 5.2. Table 5.3 presents droplet size data from the simulations cases.

In Appendix C.2 the results for Svale are presented in Figure C.2 and Table C.1 to support the results from the base case with Alve.

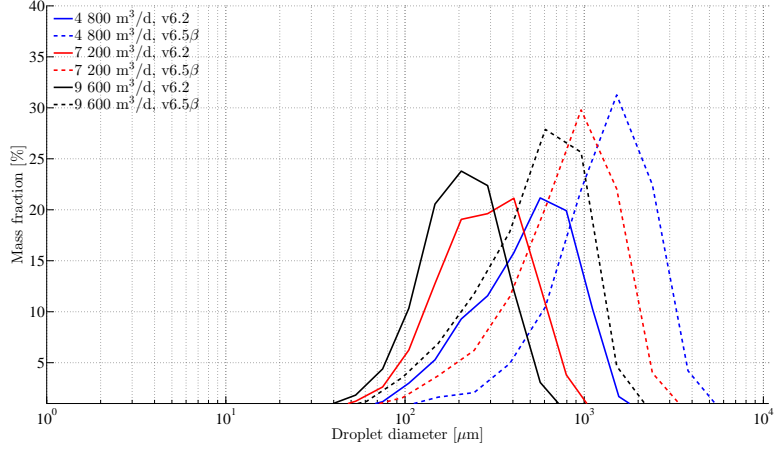


Figure 5.2: Alve: Droplet size distributions at three different flow rates; 4800, 7200 and $9600 \text{ m}^3/\text{d}$. Simulations with MEMW v6.2 are showed with solid lines and simulations with MEMW v6.5 β are showed with dashed lines.

Table 5.3: Alve: Droplet sizes for three different flow rates. The peak value, d_{peak} , and d_{95} are presented for MEMW v6.2. The same values are presented for MEMW v6.5 β together with the maximum stable droplet size, d_{max} . All droplet sizes in μm .

Rate [m^3/d]	MEMW v6.2		MEMW v6.5 β		
	d_{peak}	d_{95}	d_{peak}	d_{95}	d_{max}
4800	568	1891	1519	4640	8630
7200	405	1162	961	3005	8630
9600	206	823	607	2196	8630

5.1.3 Effect of Gas-to-Oil Ratio

Simulations with multiple GORs were performed for Alve, Norne and Svale. A GOR of 0, 100, 200 and 400 was utilized. The results are depicted in Figures 5.3 through 5.5. Tables 5.4 through 5.6 presents the most important diameters to consider when evaluating the results.

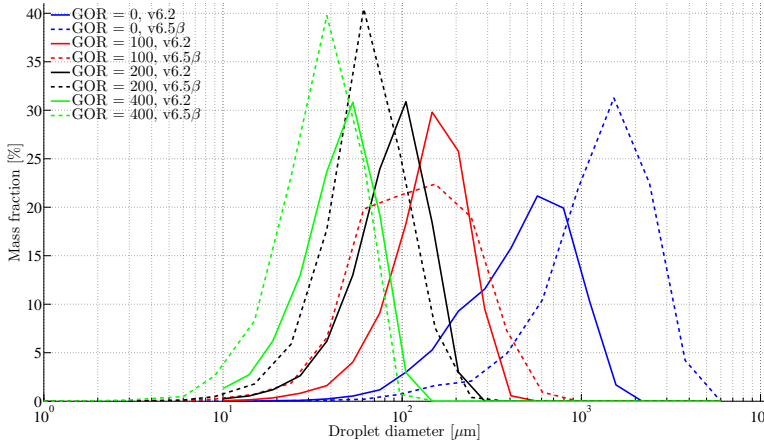


Figure 5.3: Alve: Droplet size distributions for four different GOR; 0, 100, 200 and 400. Simulations with MEMW v6.2 are showed with solid lines and simulations with MEMW v6.5 β are showed with dashed lines.

Table 5.4: Alve: Droplet sizes for simulations with and without gas. The peak value, d_{peak} , and d_{95} are presented for MEMW v6.2. The same values are presented for MEMW v6.5 β together with the maximum stable droplet size, d_{max} . All droplet sizes in μm .

GOR	MEMW v6.2		MEMW v6.5 β		
	d_{peak}	d_{95}	d_{peak}	d_{95}	d_{max}
0	568	1891	1519	4640	8630
100	147	479	153	699	8630
200	105	257	61	302	8630
400	53	126	38	119	8630

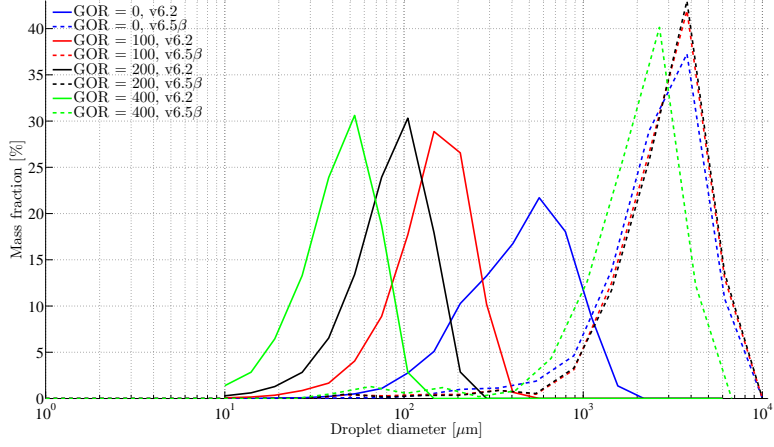


Figure 5.4: Norne: Droplet size distributions for four different GOR; 0, 100, 200 and 400. Simulations with MEMW v6.2 are showed with solid lines and simulations with MEMW v6.5 β are showed with dashed lines.

Table 5.5: Norne: Droplet sizes for simulations with and without gas. The peak value, d_{peak} , and d_{95} are presented for MEMW v6.2. The same values are presented for MEMW v6.5 β together with the maximum stable droplet size, d_{max} . All droplet sizes in μm .

GOR	MEMW v6.2		MEMW v6.5 β		
	d_{peak}	d_{95}	d_{peak}	d_{95}	d_{max}
0	568	1891	3793	10003	10003
100	147	479	3793	10003	10003
200	105	257	3792	10003	10003
400	53	126	2665	6742	10003

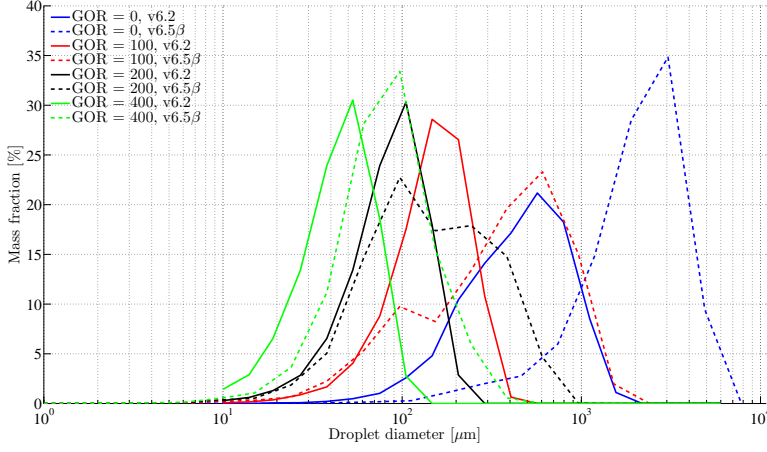


Figure 5.5: Svale: Droplet size distributions for four different GOR; 0, 100, 200 and 400. Simulations with MEMW v6.2 are showed with solid lines and simulations with new MEMW v6.5 β are showed with dashed lines.

Table 5.6: Svale: Droplet sizes for simulations with and without gas. The peak value, d_{peak} , and d_{95} are presented for MEMW v6.2. The same values are presented for MEMW v6.5 β together with the maximum stable droplet size, d_{max} . All droplet sizes in μm .

GOR	MEMW v6.2		MEMW v6.5 β		
	d_{peak}	d_{95}	d_{peak}	d_{95}	d_{max}
0	568	1891	3046	7827	10719
100	147	479	607	1806	10719
200	105	257	97	971	10719
400	53	126	97	485	10719

5.1.4 Effect of dispersant

Simulations with Alve, both with and without dispersant, are performed with MEMW v6.2 and v6.5 β . The results are presented in Figure 5.6 and Table 5.7. Results for Svale are presented in Appendix C.3 to support the results for Alve.

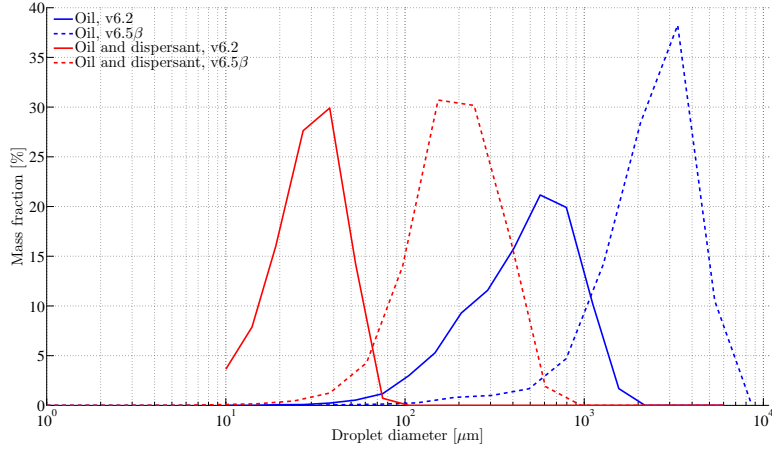


Figure 5.6: Alve: Droplet size distributions without and with dispersant. Without dispersant are blue lines, and with dispersant are red lines. Simulations with MEMW v6.2 are showed with solid lines and simulations with MEMW v6.5 β are showed with dashed lines.

Table 5.7: Alve: Droplet sizes for simulations with and without simulations. The peak value, d_{peak} , and d_{95} are presented for MEMW v6.2. The same values are presented for MEMW v6.5 β together with the maximum stable droplet size, d_{max} . All droplet sizes in μm .

IFT [mN/m]	MEMW v6.2		MEMW v6.5 β		
	d_{peak}	d_{95}	d_{peak}	d_{95}	d_{max}
20	568	1891	1519	4640	8630
1	38	79	153	814	894

5.1.5 Dispersant-to-Oil Ratio

Different values of IFT were chosen to represent the change in DOR. The chosen values were based on earlier simulations, confer e.g. Brandvik et al. (2013), to include the effect of dispersant mixed with oil. The IFT values were 20, 5, 1, 0.1, 0.05 and 0.01 mN/m, these values represents a reduction in IFT, from the starting point of 20 mN/m, by factors of 0, 4, 20, 200, 400 and 2000, respectively.

The different DORs were simulated, both with MEMW v6.2 and v6.5 β . The results for v6.2 are depicted in Figure 5.7 and in Figure 5.8 for v6.5 β . Table 5.8 presents the different oil droplet sizes.

To avoid d_{95} equal to d_{\max} for all the IFT values, a higher flow rate, 7200 m³/d, was utilized for Alve. The result was a d_{95} equal to d_{\max} only for the lowest IFT of 0.01 mN/m. Hence, the oil droplet distribution may not be completely representative.

The results for Alve and Svale at 4800 m³/d are presented in Appendix C.4. For Alve, the two lowest IFTs have d_{95} equal to d_{\max} . For Svale all the IFTs, except 20 mN/m, has d_{95} equal to d_{\max} .

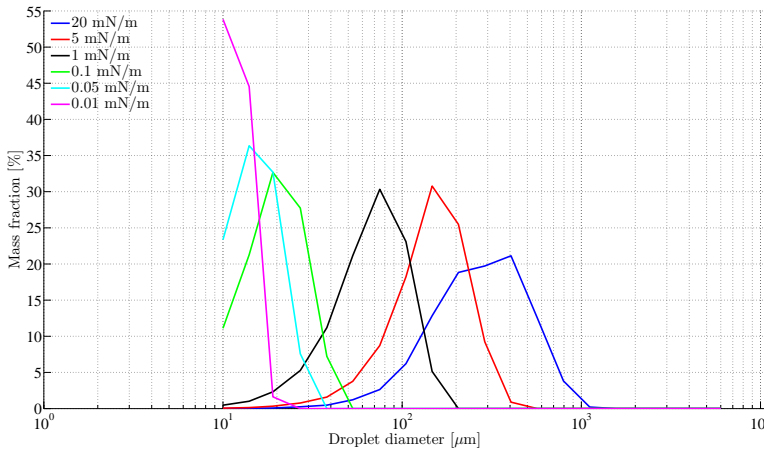


Figure 5.7: Alve: Droplet size distributions for six different IFT values and flow rate of 7200 m³/d. Simulations with MEMW v6.2 are showed with solid lines.

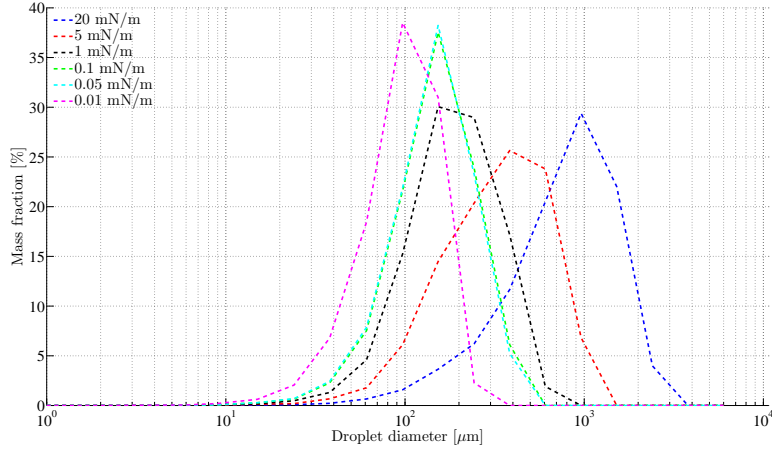


Figure 5.8: Alve: Droplet size distributions for six different IFT values at a flow rate of 7200 m³/d. Simulations with MEMW v6.5β are showed with dashed lines.

Table 5.8: Alve: Droplet sizes for simulations with different IFT values at a flow rate of 7200 m³/d. The peak value, d_{peak} , and d_{95} are presented for MEMW v6.2. The same values are presented for MEMW v6.5β together with the maximum stable droplet size, d_{max} . All droplet sizes in μm.

IFT [mN/m]	MEMW v6.2		MEMW v6.5β		
	d_{peak}	d_{95}	d_{peak}	d_{95}	d_{max}
20	405	1162	961	3005	8630
5	147	506	384	1488	4768
1	75	193	153	827	2394
0.1	19	48	153	606	894
0.05	14	32	153	592	664
0.01	10	20	97	334	334

Another representation of the results from variable DOR is a plot of d_{95} as a function of IFT. The results are presented in Figure 5.9. The lowest IFT value of 0.01 mN/m is excluded from the figure since d_{95} is equal to d_{max} .

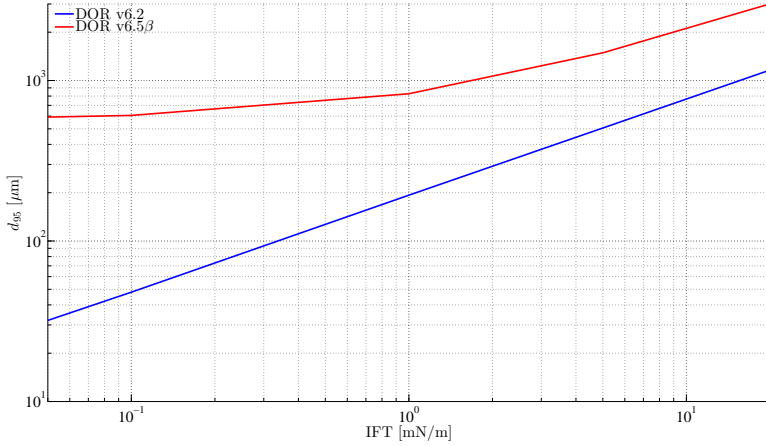


Figure 5.9: Alve: d_{95} as a function of IFT, with flow rate of $7200 \text{ m}^3/\text{d}$, without the lowest IFT value of 0.01 mN/m .

5.2 Laboratory Experiments

To obtain an improved understanding of the theory behind the droplet size distributions and the simulations performed with MEMW, a small quantity of laboratory experiments were performed. The main objective with the laboratory experiments was to obtain one oil droplet distribution for pure oil, i.e. untreated oil, and one for oil mixed with dispersant.

The first section with monodisperse particles is included to verify the LISST-100X utilized for measuring oil droplet size distributions. In addition, the results from the experiments with oil is presented in the sections to follow. Table 5.9 presents the different flow conditions for the fluids utilized in the MiniTower experiment.

Table 5.9: Flow rates for fluids utilized in laboratory experiments.

Fluid	Flow rate
Seawater [L/min]	100
Oil [mL/min]	100
Dispersant [mL/min]	1

5.2.1 Monodisperse Particles

To verify the measurements taken with the LISST-100X, two sizes of monodisperse polystyrene particles or standards, 80 and 346 μm , were injected into the MiniTower below the LISST-100X to measure their respective size. The results from the experiments with the monodisperse particles are depicted in Figure 5.10.

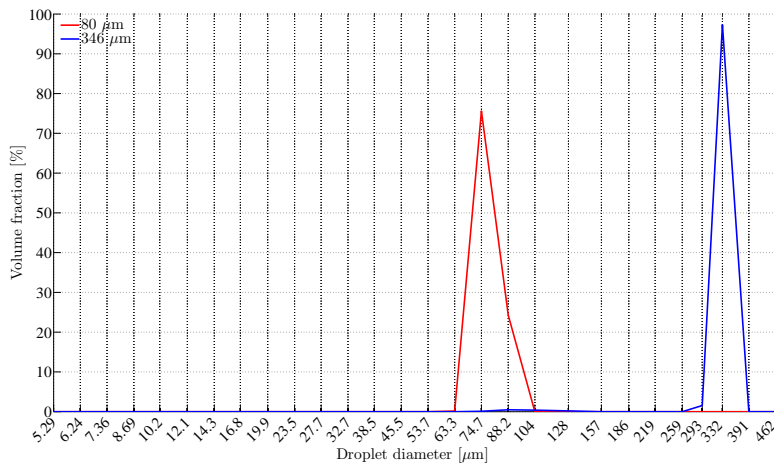


Figure 5.10: Verification of the LISST measurements with monodisperse particles, or standards, with diameter of 80 μm and 346 μm , respectively.

5.2.2 Alve Laboratory Results

The laboratory results for Alve are depicted in Figure 5.11. The blue line is the oil droplet size distribution for pure oil, while the red line is the oil droplet distribution for the mixture of oil and dispersant with a DOR of 1:100.

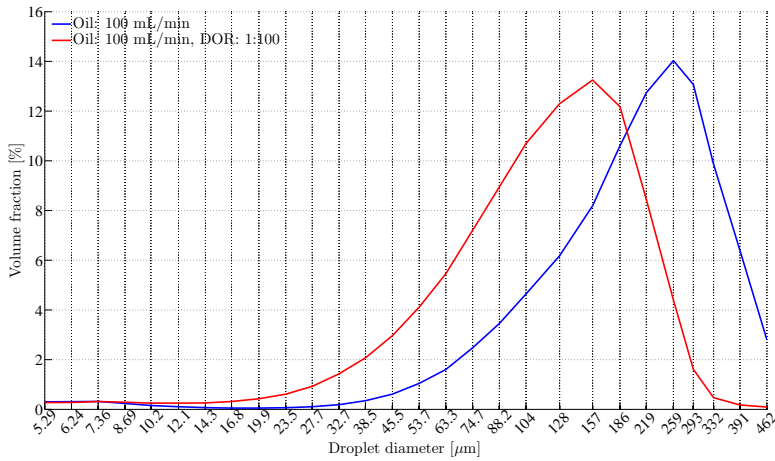


Figure 5.11: Droplet size distributions for Alve, both with and without dispersant, from laboratory experiment. d_{50} for pure only: 259 μm , and d_{50} for oil and dispersant: 157 μm .

5.2.3 Norne Laboratory Results

The oil droplet size distribution from the laboratory results with Norne are depicted in Figures 5.12 and 5.13. The first figure depicts the same graphs as for Alve and Svale, while the second figure depicts oil droplet size distributions for four different flow rates. Table 5.10 presents the d_{50} values for the respective flow rates.

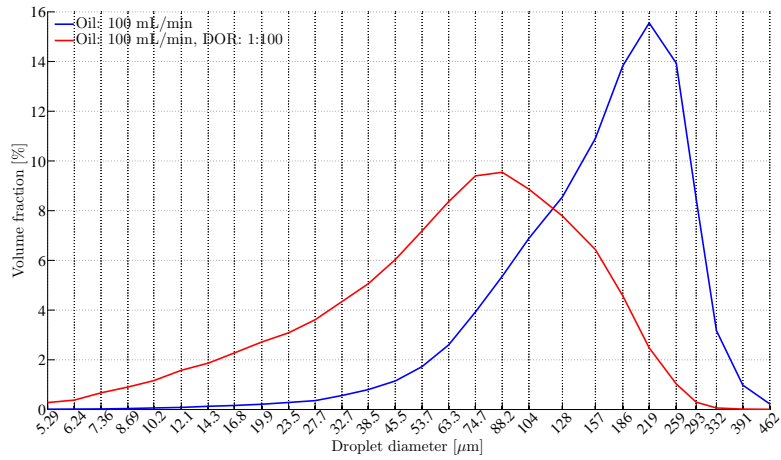


Figure 5.12: Droplet size distributions for Norne, both with and without dispersant, from laboratory experiment. d_{50} for pure only: 219 μm , and d_{50} for oil and dispersant: 88.2 μm .

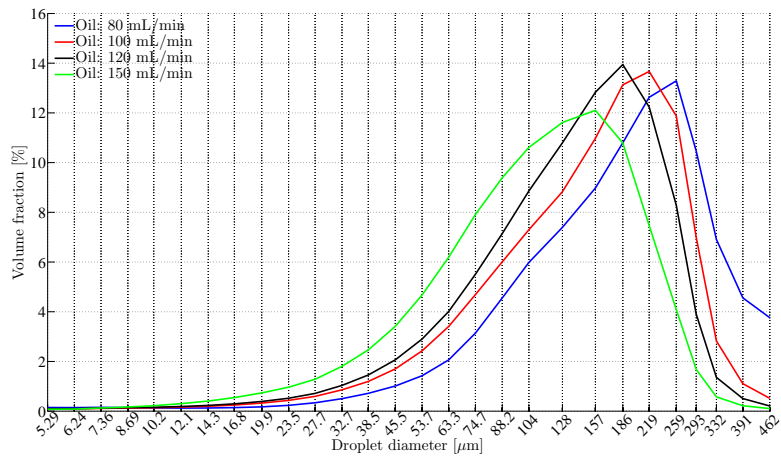


Figure 5.13: Droplet size distributions for Norne, at four different flow rates, from laboratory experiment. d_{50} values are presented in Table 5.10.

Table 5.10: d_{50} values for Norne with four different flow rates.

Flow rate [mL/min]	d_{50} [μm]
80	259
100	219
120	186
150	157

5.2.4 Svale Laboratory Results

The laboratory results for Svale are depicted in Figure 5.14. The blue line is the oil droplet size distribution for pure oil, while the red line is the oil droplet distribution for the mixture of oil and dispersant with a DOR of 1:100.

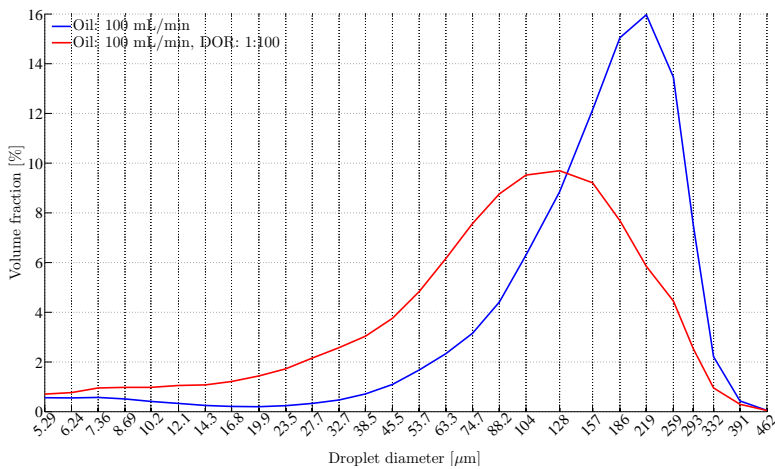


Figure 5.14: Droplet size distributions for Svale, both with and without dispersant, from laboratory experiment. d_{50} for pure only: 219 μm , and d_{50} for oil and dispersant: 128 μm .

5.2.5 Comparison of Volume Median Diameters

Table 5.11 presents the d_{50} values for Alve, Svale and Norne. The values are for pure oil, $d_{50,oil}$, and for oil mixed with dispersant, $d_{50,disp}$.

Table 5.11: d_{50} values for the three oils utilized in the laboratory experiments. Both for pure only and with dispersant with a DOR of 1:100.

Oil type	$d_{50,oil}$ [μm]	$d_{50,disp}$ [μm]
Alve	259	157
Norne	219	88.2
Svale	219	128

5.3 Interfacial Tension Measurements

The results of the measurements of IFTs for the three oils, with the spinning drop method, are presented in Table 5.12. Two values for each oil are reported, IFT for pure oil and oil mixed with dispersant. The measurements are performed at 13°C for Alve and Svale, while 25°C is utilized for Norne as it has a high pour point, 21°C.

Table 5.12: Interfacial tension results for the fresh crude oils and with premixed dispersant for Alve, Norne and Svale (Farooq, SINTEF, 2013).

Oil Type	IFT [mN/m]
Alve	13.0 ± 0.7
Norne*	18.2 ± 0.2
Svale	13.3 ± 0.1
IFT measurements with premixed dispersant	
Alve	0.09 ± 0.05
Norne*	0.007 ± 0.003
Svale	0.4 ± 0.2

* Measured at 25°C due to elevated pour point.

The densities of the samples with premixed dispersants are slightly higher, 0.1 % than

the samples with pure oil. The densities for Alve, Norne and Svale with dispersant are 0.7969, 0.8639 and 0.9147 g/mL, respectively.

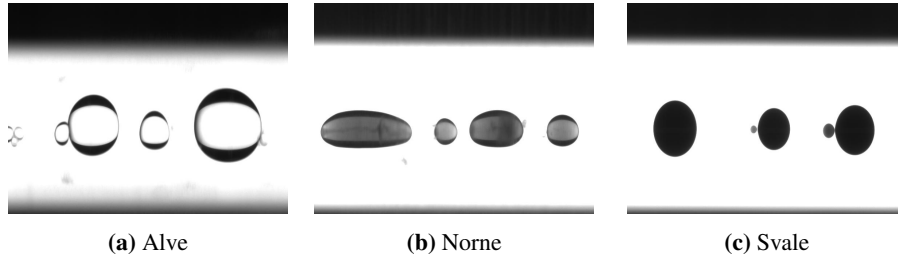


Figure 5.15: Oil droplets with premixed dispersant, with a DOR equal to 1:100. The pictures are taken with the spinning drop video tensiometer during the IFT measurements.

5.4 Up-scaling from Laboratory to Full Scale Experiments

An up-scaling of the laboratory results to the same nozzle diameter, 120 mm, utilized in the simulations with MEMW was performed. The d_{50} values was calculated for both the laboratory data and the up-scaled data for pure oil and oil mixed with dispersant. The sequence of equations utilized for calculating d_{50} values are presented in Appendix C.6.

Figures 5.16 through 5.18 compares actual oil droplet size distributions from the laboratory with the calculated distributions from the tables. Tables 5.13 through 5.15 presents the d_{50} values, as well as input data to the calculation, calculated and modified velocities, We number and Re number.

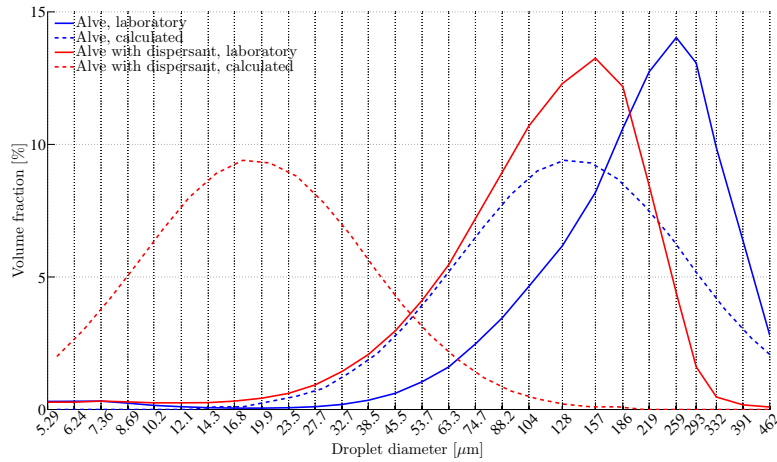


Figure 5.16: Alve: Comparison of calculated and measured droplet size distributions. d_{50} value for pure oil; measured was 259 μm and calculated was 125 μm . For oil mixed with dispersant; measured was 157 μm and calculated was 17 μm .

Table 5.13: Alve: Up-scaled data from MiniTower to full scale, with same diameter as utilized in simulations.

	D [mm]	Q_{oil}	n [%]	U_{oil} [m/s]	U' [m/s]	We'	Re'	$d_{50,oil}$ [μm]	$d_{50,disp}$ [μm]
Lab.	0.5	0.1 L/min	0	8.5	8.5	2223	1660	125	17
Full	120	22 m ³ /h	50	0.6	1.6	19433	76030	7895	438

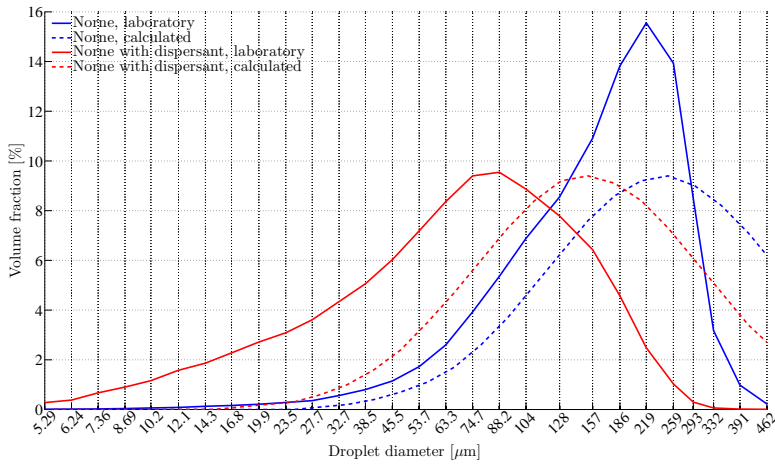


Figure 5.17: Norne: Comparison of calculated and measured droplet size distributions. d_{50} value for pure oil; measured was 219 μm and calculated was 247 μm . For oil mixed with dispersant; measured was 88.2 μm and calculated was 140 μm .

Table 5.14: Norne: Up-scaled data from MiniTower to full scale, with same diameter as utilized in simulations.

	D [mm]	Q_{oil}	n [%]	U_{oil} [m/s]	U' [m/s]	We'	Re'	$d_{50,oil}$ [μm]	$d_{50,disp}$ [μm]
Lab.	0.5	0.1 L/min	0	8.5	8.5	1257	91	247	140
Full	120	22 m ³ /h	50	0.5	1.6	10683	4096	11889	2054

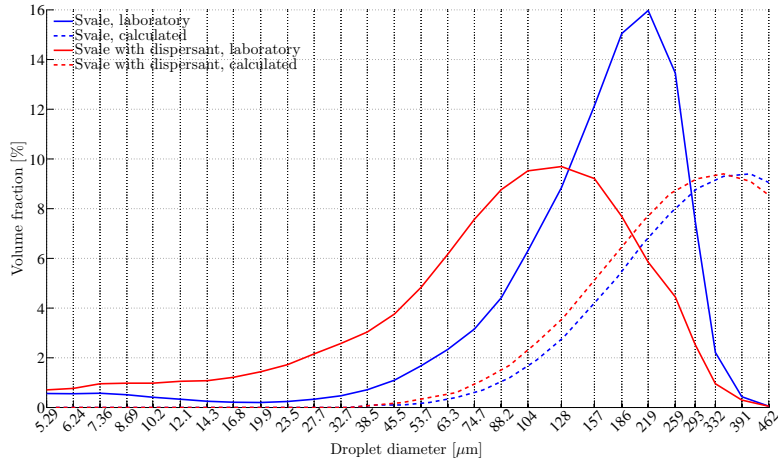


Figure 5.18: Svale: Comparison of calculated and measured droplet size distributions. d_{50} value for pure oil; measured was 219 μm and calculated was 353 μm . For oil mixed with dispersant; measured was 128 μm and calculated was 313 μm .

Table 5.15: Svale: Up-scaled data from MiniTower to full scale, with same diameter as utilized in simulations.

	D [mm]	Q_{oil}	n [%]	U_{oil} [m/s]	U' [m/s]	We'	Re'	$d_{50,oil}$ [μm]	$d_{50,disp}$ [μm]
Lab.	0.5	0.1 L/min	0	8.5	8.5	2489	31	353	313
Full	120	22 m ³ /h	50	0.5	1.6	20697	1380	9723	4388

6 Discussion

The discussion is divided into three sections representing the main results from the simulations with MEMW, i.e. effect of oil type, GOR and dispersant. In addition, sections addressing the laboratory experiments, up-scaling of the laboratory experiments and a few general considerations are added.

6.1 Effect of Oil Type

When the oil types were compared with MEMW v6.2, equal oil droplet size distributions and identical peak values were observed for the three oils, Alve, Norne and Svale. MEMW v6.5 β , with the new implemented droplet size algorithm, calculate different peak values for the three oil types. Alve had the lowest peak value at 1.5 mm followed by Svale with a peak value at 3.0 mm. Norne had the highest peak value at 3.8 mm. A reason for the differences in the peak values in MEMW v6.2 compared to MEMW v6.5 β is the large difference in viscosity between the three oils. In the new algorithm, see Equation (2.62), the Vi number is included with an additional term compared to the existing algorithm. The new term will contribute to oil droplet size distributions with larger droplets. The added term is implicitly dependent on the viscosity through the Vi number, as well as IFT and initial velocity of the jet.

Results from the simulations with several flow rates yields oil droplet size distributions with smaller droplets as the flow rate increases. To avoid distributions with secondary droplet splitting as a dominating process the 95 % maximum droplet size, d_{95} , must be smaller than the maximum stable droplet size, d_{\max} . For the default flow rate value of 4800 m³/d, Alve yielded a d_{95} that was 54 % of d_{\max} . It was considered to be an acceptable starting point for the simulations. When the flow rate was halved, i.e. 2400 m³/d and still utilizing the default outlet nozzle diameter, d_{95} was equal to d_{\max} . Thus, the flow rate was omitted from the simulations.

Svale with a flow rate of 7200 m³/d and 9200 m³/d with MEMW v6.5 β , equal peak values were observed. With MEMW v6.2 different peak values for all three flow rates were observed. Higher outlet velocity of oil jet, i.e increased flow rate, broke the oil

down into smaller droplets. The oil droplet size distribution was then shifted towards smaller sizes .

The same situation was not observed for Alve. Here, the peak values differ from each other for both MEMW v6.2 and v6.5 β . The difference between the oil types, when comparing flow rates, are caused mainly by the difference in viscosity for the oils. Density and IFT also comes in when comparing the flow rates.

In the simulations with MEMW the peak values attained are not necessarily equal to the volume median diameters. Assuming a logarithmic linear plot of the distribution, the maximum peak will be representative for the volume median diameter. The volume median diameters can be obtained if the cumulative volume fraction is depicted as a function of droplet sizes. This was not performed in the results as the shape of the oil droplet size distribution with mass fractions is easier to interpret than the cumulative volume fraction.

6.2 Effect of GOR

A GOR of 100 in MEMW v6.5 β yields a higher peak value for all three oil types compared to MEMW v6.2. With a GOR of 200, v6.5 β predicted smaller droplets than v6.2 for Alve and Svale. A possible reason for the observed effect can be the correction for buoyancy included in MEMW v6.5 β . For Norne, the oil droplet size distributions were always larger in v6.5 β compared to v6.2. The main reason was the high viscosity of Norne utilized as input in the simulations. It resulted in a d_{95} equal to d_{\max} . A GOR of 400 predicted an oil droplet size distribution not limited by the maximum stable droplet size for Norne. Hence, the distribution can be compared with Alve and Svale at a GOR of 400.

A GOR of 400 for Alve and Svale yields two different oil droplet size distributions, where for Alve MEMW v6.5 β predicted a lower peak value than v6.2. The opposite occurred for Svale where MEMW v6.2 predicted the highest peak value. Possible reasons for the droplet size distributions observed with different GOR are probably the buoyancy and void fraction corrections included in MEMW v6.5 β . They cause a higher turbulence in the plume for the simulations with MEMW v6.5 β compared to v6.2. The sensitivity

for change in GOR is increased in MEMW v6.5 β compared to v6.2. In MEMW v6.5 β , Equation (2.63) is included to correct for void fraction.

6.3 Effect of Dispersant

The simulations where the effect of dispersant was studied yield results in accordance with theory, where v6.5 β predicted oil droplet size distributions with higher peak values compared to v6.2. It can be explained by the implementation of new and modified algorithm for calculating the median volume droplet size diameter. The new added term will calculate larger oil droplet size distributions compared to the existing algorithm.

Simulations with several DORs yield oil droplet size distributions in accordance with the new droplet size algorithm implemented into MEMW v6.5 β . Peak values from the simulations with v6.5 β are consistently higher than peak values from v6.2. With decreasing IFT, the oil droplet size distribution decrease, i.e. the oil droplets become smaller.

For Alve the default flow rate of 4800 m³/d yields a d_{95} equal to d_{\max} for the two lowest IFTs, 005 and 0.01 mN/m. The flow rate for Alve was increased to 7200 m³/d and only the lowest value of 0.01 mN/m had a d_{95} equal to d_{\max} . Alve with a flow rate of 7200 m³/d yields the the best prediction of oil droplet size distributions, thus presented in the results. To avoid a d_{95} to be equal to d_{\max} for the lowest IFT, a flow rate 3.5 times larger than the default flow rate, 16 800 m³/d, must be used. As this correspond to a flow rate twice the size of the flow rate in the Macondo blowout, the flow rate was considered unrealistic and simulations was not performed.

The IFT measurements confirmed differences between the three oils. Norne, with a value of 18.2 mN/m, had the highest IFT for fresh oil due to the high content of wax. Svale and Alve had approximately equal values, i.e. approximately 13 mN/m. The IFT of oils with premixed dispersant rendered Norne with the lowest value, followed by Svale and Alve. The values for Alve, Norne and Svale were reduced 140, 2600 and 30 times, respectively. The oil droplet size distributions measured in the MiniTower were in accordance with the simulations. An exception was the laboratory results for Alve with larger droplets than both Norne and Svale.

As depicted in Figure 5.9, where d_{95} is plotted as a function of IFT, it is a distinct difference between MEMW v6.2 and v6.5 β . d_{95} in MEMW v6.2 has a linear decrease towards smaller droplets. For the existing algorithm in v6.2, it is possible to obtain droplets with an infinite small diameter by decreasing the IFT values. d_{95} for v6.5 β will decrease towards an asymptotic value and at a specific point additional dispersant will not decrease the droplet size. Thus, there exists an absolute minimum droplet size, even though the IFT is further decreased. If the IFT is small enough the droplet size is no longer dependent on the We number, instead it is dependent on the Re number. It may be the reason for the inconsistency observed for low IFTs. Another possible reason is that d_{95} is equal to d_{\max} and the correct oil droplet size distribution is not obtained.

The IFT measurements were performed at 13°C for Alve and Svale, and at 25°C for Norne. To obtain the most correct values for the conditions in the MiniTower, the temperatures should have been lower, as the actual seawater temperature was lower, during the experiments. In addition, the dispersant was premixed with the pure oils. In experiments performed in the MiniTower the dispersant was injected into the jet, six nozzle diameters below the outlet of the jet. Thus, the mixtures may not have the same characteristics.

To measure IFT with high density oils, e.g. Svale, can be a challenge. It is challenging to create droplets inside the capillary test tube. When injecting the oil with a needle, the droplets may stick to the needle tip and create too large droplets which renders IFT measurements unattainable. In addition, there is often a variation in the IFT values and a distribution of dispersant in the oil sample may be the reason. It could be a possible explanation and must be tested further to be proven or disproved.

An important field of interest these days is the effect of dispersant on different oil types. Understanding the effect of different dispersants are crucial to develop improved dispersants, which can handle the large variety of crude oils. There are large differences between dispersants and different dispersants have different advantages. One dispersant can e.g. be mixed with oil for a long time period, while another dispersant can disappear from the oil after a short time period.

6.4 Laboratory Experiments

The laboratory experiments were conducted to increase the understanding of underlying theory for oil droplet size distributions. In addition, the experiments were utilized to test a prototype of SINTEF's new MiniTower. The available quantity of Alve and Svale limited the experiments to one run with pure oil and one run with oil mixed with Corexit 9500 dispersant. A larger quantity of Norne was available, thus experiments with four different flow rates were performed. The seawater flow of 100L/min produced small concentrations of oil, measured by the LISST-100X and could have been substantially higher.

The d_{50} values for the three oil types alone yielded almost equal oil droplet size distributions. Norne and Svale had the same peak at 219 μm , while Alve had a slightly higher at 259 μm . There were larger differences when the oils were mixed with dispersant at a DOR of 1:100. After addition of dispersant, the peak values were found to be 88.2 μm , 128 μm and 157 μm for Norne, Svale and Alve, respectively. The results for Alve, Norne and Svale, as pure oils, were in accordance with the IFT values measured in the laboratory. Norne and Svale had d_{50} values in the same bin, while Alve had the d_{50} value in a larger bin, right next to Norne and Svale.

The IFT measurements for pure oils indicate that Norne should produce the largest droplets, followed by Svale and Alve. The result for the oils was Alve with the largest droplets, followed by Svale and Norne with equal d_{50} value. The oil droplet size distribution for Alve is not necessarily incorrect as the difference in IFT measurements were within the same range, a deviation of 5 mN/m is not a large correction. A significant correction would be the IFT values for oil mixed with dispersant where the IFT is reduced 30 times or more.

Comparing the IFT measurements for the three oils mixed with dispersant, Norne should produce the smallest droplets according to IFT theory, which it did. Alve should produce larger droplets than Norne, due to increased IFT and was confirmed by the resulting oil droplet size distributions. However, Svale should yield the largest droplets due to the highest IFT of the three oils when mixed with dispersant. This was not the case as the volume median diameter for Svale was between Alve and Norne.

To further verify and improve the models for subsurface blowouts of oil and gas a more comprehensive quantity of laboratory experiments will be required. Laboratory experiments yields crucial information to improve the existing blowout models for predicting subsurface releases of oil and gas. Experiments resembling an actual blowout, e.g. field scale or full scale experiments, would yield valuable data required to fully understand the phenomena occurring during a blowout. However, it is difficult to obtain permissions for these experiments due to environmental regulations and restriction on quantities of oil released in seawater. In addition, field experiments are very expensive and requires extensive planning.

For the viscosity measurements, the standard pre-treatment at SINTEF was not followed. A consequence may be different values compared to earlier measurements performed at SINTEF of the three oils. The tests are nevertheless performed at a temperature close to the seawater in the MiniTower.

6.5 Up-scaling of Laboratory Experiments

The calculated oil droplet size distributions, based on the inlet flow of oil, nozzle diameter in the MiniTower and physical characteristics of the oils, resulted in both too low and too high values compared to the oil droplet size distributions measured in the MiniTower. Physical parameters affecting these calculations are especially viscosity and IFT. Both were measured at SINTEF, to obtain equal conditions as the MiniTower. Another parameter affecting the calculations can be the flow rate from the oil pump. However, the uncertainty of the pump is very low and should not affect the results.

The actual shear rate inside the nozzle in the MiniTower was calculated to be very high. With a nozzle diameter of 0.5 mm and an oil flow of 100 mL/min, the value is approximately $135\,000\text{ s}^{-1}$. This will affect the viscosity of the oil, especially for an oil with a non-Newtonian behaviour, e.g. Norne. As the viscosity is very sensitive to temperature change, it is desirable to measure the viscosity in the laboratory as close as possible to conditions out at sea.

To perform experiments in the MiniTower with Weber numbers comparable to field conditions, e.g. DeepSpill, the flow rate of oil should be increased to at least 500 mL/min or the nozzle should be reduced to 0.1 mm. The modified We number will increase to

approximately the same value obtained in the Tower basin and by an eventual up-scaling of these results, the volume median diameters will probably be closer to the field data from DeepSpill and Macondo. However, the intention with the MiniTower was originally screening of different dispersants and the results from these experiments are not necessary to up-scale.

6.6 General Considerations

The results from the simulations with MEMW could have been illustrated with cumulative volume fractions compared to the utilized, mass fraction in percent versus droplet diameter. The diameters are divided in multiple bins and if the droplets are small enough a standard distribution is utilized. The size range is between 10 and 6000 μm , and between 1 and 6000 μm for MEMW v6.2 and v6.5 β , respectively. If the droplets are larger, e.g. at low flow rates, the bin with largest droplet size will have the value of d_{max} of the respective oil.

Division of oil droplets in bins with determined sizes may contribute to not observing the differences in oil droplet size distributions, even though there is a shift in the volume median diameter. If one oil has a d_{50} in the lowest part of the bin, while another oil is in the upper part of the bin, their distributions will appear to be the same. For bins with larger diameters, their range can be several hundred micrometer. For bins with smaller diameters, the range is smaller and it will be easier to see a shift in volume median diameter.

The run-time for subsurface blowout simulations was set to twelve hours. Data was collected after ten hours due to unstable oil droplet size distributions in the last time step. The number of particles in the water column representing liquid oil droplets after ten hours was very different from simulation case to case. A larger number of particles were present for a few of the cases. Increased number of particles would have been achieved by decreasing the run-time. With shorter time steps as input to the model, it performs a larger quantity of calculations. The main outcome of increasing the number of particles in the water column would probably been smoother oil droplet size distributions.

The bin sizes for the droplets can affect the distribution of oil droplets. It can be a challenge to shift a distribution, e.g. from a higher to a lower droplet distribution, by chang-

ing the IFT. It was the case for simulations with different DOR of 1, 0.1 and 0.05 mN/m where the same peak value at 153 μm was observed. In reality the oil droplet size distribution should shift towards smaller droplets when decreasing the IFT. However, as the droplets are placed in predetermined bins where only the peak diameter is utilized for representation of the bin, the peak value for the distribution may not be entirely correct.

To obtain quality assured and robust simulations, with MEMW v6.2 and v6.5 β , as few as possible changes in parameters should be utilized. Multiple release locations, multiple depths, numerous oil types, flow rates, IFTs and GOR could form a more solid basis for the oil droplet size distributions.

Robust-and-close to reality simulation models are important for understanding subsurface releases of oil and gas, due to the increased search for oil and gas in more vulnerable areas, e.g. the search for oil is moving further north. If the models predict the location of the oil and its condition, preventing or partially preventing the oil from reaching wildlife reserves and other vulnerable areas will have an increased likelihood of success. If a blowout preventer, BOP, breaks down, oil and gas will flow out of the reservoir and if a cap and contain system is not in place the oil will reach the water column and consequently the sea surface. The best method to find escaped oil would be to predict the location with simulations. A simulation model as MEMW would be invaluable for authorities and companies trying to prevent oil from reaching habitats, settlements and other vulnerable areas.

The new and modified We number scaling, utilized to calculate the oil droplet size distributions, in MEMW v6.5 β represents only minor changes. As it is based on data acquisition from many experiments performed in SINTEF's Tower Basin, it will probably estimate more correct oil droplet size distributions compared to earlier versions of MEMW.

7 Conclusion

The new modified algorithm for determining oil droplet size distributions, implemented in MEMW v6.5 β , produces oil droplet size distributions with larger droplets compared to MEMW v6.2. MEMW v6.5 β yields results in accordance with the new modified algorithm when effect of oil type, GOR and dispersant was investigated.

The inclusion of the new algorithm in MEMW v6.5 β , which is dependent on differences in viscosity for different oil types, is especially important when predicting the efforts required to inhibit or prevent subsurface blowouts of oil and gas.

In MEMW v6.5 β , a reduction in DOR does no longer create infinite small oil droplets when the interfacial tension becomes low enough. Rather, it decreases towards an asymptotic value which is an improvement from MEMW v6.2.

The laboratory results were in accordance with both theory and simulations. The up-scaled laboratory results, predicted volume median diameters of oil droplets larger than the maximum stable droplet size. Hence, the oil droplets will be exposed to secondary droplet splitting.

Interfacial tension measurements yield similar interfacial tension values for pure Alve, Norne and Svale. With addition of dispersant, the values decreased in accordance with the theory. The values for Alve, Norne and Svale was reduced 140, 2600 and 30 times with a DOR of 1:100, respectively.

8 Recommendations

Many of the obtained results may be of interest for further investigation. The coherence between viscosity and shear rate, and its effect on oil droplet size distributions may be interesting to explore in more detail.

Only a small part of the required verification work with MEMW v6.5 β has been performed during this Master's thesis. A comprehensive set of simulations must be performed to investigate the robustness of the model. To further validate the oil droplet size distributions from MEMW v6.5 β , a comprehensive set of field data should be compared with simulated distributions.

Possible improvement, at least if the oil's properties considerably differ from the rest, is a procedure to estimate IFT as a function of dispersant type, DOR and oil type in MEMW automatically when changing oil type. The connection between dosage of dispersant, IFT between oil droplets and water should be areas for increased research. A reason is the many unresolved challenges on how to apply the dispersants most effectively.

For the future experiments performed in the MiniTower, a higher concentration of oil should be achieved. With the seawater flow of 100L/min, utilized in the laboratory experiments, a partially horizontal movement was observed in addition to the main vertical flux. Lowering the seawater flow, higher oil concentrations can be attained in the MiniTower. Hence, the flow will be less turbulent.

Accidents with subsurface releases of oil and gas will definitely occur in the future. In case of a blowout, operational models predicting the fate of oil are essential to be able to reduce the environmental impact. The models can be utilized during oil spills to predict where the oil will be located at any given time. The models for simulating the blowouts are of great importance for oil companies, national authorities and the population in areas that can be affected of a release of oil and gas.

When, and if, oil droplet size distributions are measured in the sea at an actual subsurface blowout, entrainment of sediment particles can affect the droplet distribution. It is important to do field measurements to create field datasets for validating models. These data should be collected when the next accidental blowout of oil and gas occur.

If the work performed in this Master's thesis is to be utilized in further and expanded work, gaining more insight to the link between simulations and experiments with the MiniTower is recommended.

References

- Adcroft, A., Hallberg, R., Dunne, J., Samuels, B., Galt, J., Barker, C. and Payton, D. (2010). Simulations of underwater plumes of dissolved oil in the Gulf of Mexico,, Technical report, Geophys. Res. Lett.
- Agrawal, A. (2013). Interfacial tension, <http://web.mit.edu/nmf/education/wettability/interfacial.html>.
- Agrawal, Y. and Pottsmith, H. (2000). Instruments for particle size and settling velocity observations in sediment transport, Marine Geology **168**: 89–114.
- Attension (2012). Interfacial tension, <http://www.attension.com/interfacial-tension>.
- Bandara, U. and Yapa, P. (2011). Bubble Sizes, Breakup, and Coalescence in Deepwater Gas/Oil Plumes, Journal of Hydraulic Engineering **137**: 729–738.
- Bettellini, M. and Fanneløp, T. (1993). Underwater plume from an instantaneously started source, Applied Ocean Research **15**: 195–206.
- Bishnoi, P., Gupta, A., Englezos, P. and Kalogerakis, N. (1989). Multiphase Equilibrium Flash Calculations for Systems Containing Gas Hydrates, Fluid Phase Equilibria **53**: 97–104.
- Brandvik, P., Øistein Johansen, Angell, G. and Leirvik, F. (2013). Subsurface oil releases – Experimental study of droplet distributions and different dispersant injection techniques. final report, Technical report, SINTEF Materials and Chemistry, Environmental Technology.
- Brandvik, P., Johansen, Ø., Leirvik, F., Farooq, U. and Daling, P. (2012). Droplet breakup in sub-surface oil releases - Part 1: Experimental study of droplet breakup and effectiveness of dispersant injection, Submitted to Marine Pollution Bulletin October 2012 .
- Brown, Challenger, Etkin, Fingas, Hollebone, Kirby, Lamarche, Law, Mauseth, Michel, Nichols, Owens, Quek, P., Shigenaka, Simecek-Beatty and Yender (2011). Oil Spill Science and Technology, Gulf Professional Publishing.

- Ceylan, S., Kelbaliyev, G. and Ceylan, K. (2003). Estimation of the maximum stable drop sizes, coalescence frequencies and the size distributions in isotropic turbulent dispersions, Colloids and Surfaces, A: Physicochemical and Engineering Aspects **212**: 285–295.
- Chen, F. and Yapa, P. (2001). Estimating hydrate formation and decomposition of gases released in a deepwater ocean plume, Journal of Marine Systems **30**: 21–32.
- Chen, F. and Yapa, P. (2002). A model for simulating deepwater oil and gas blowouts - Part II: Comparison of numerical simulations with "DeepSpill" field experiments, Journal of Hydraulic Research **41**: 353–365.
- Chen, F. and Yapa, P. (2004a). Modeling gas separation from a bent deepwater oil and gas jet/plume, Journal of Marine Systems **45**: 189–203.
- Chen, F. and Yapa, P. (2004b). Three-dimensional visualization of multi-phase (oil/-gas/hydrate) plumes, Environmental Modelling & Software **19**: 751–760.
- Chen, F. and Yapa, P. (2007). Estimating the oil droplet size distribution in deepwater oil spills, Journal of Hydraulic Engineering pp. 197–206.
- Committee on Effectiveness of Oil Spill Dispersants (1989). Using Oil Spill Dispersants on the Sea, Technical report, National Research Council.
- Committee on Understanding Oil Spill Dispersants: Efficacy and Effects (2005). Oil Spill Dispersants - Efficacy and Effects, Technical report, National Research Council of the National Academies.
- Daling, P., Moldestad, M., Johansen, Ø., Lewis, A. and Rødal, J. (2003). Norwegian Testing of Emulsion Properties at Sea - The Importance of Oil Type and Release Conditions, Spill Science & Technology Bulletin **8**(2): 123–136.
- Daling, P., Singsaas, I., Reed, M. and Hansen, O. (2002). Experiences in Dispersant Treatment of Experimental Oil Spills, Spill Science & Technology Bulletin **7**: 201–213.
- Daly, S. (1991). Frazil Ice Blockage of Intake Trash Racks, Cold Regions Technical Digest **91**(1): 1–12.
- Darby, R. (2001). Chemical Engineering Fluid Mechanics, Marcel Dekker, Inc.

REFERENCES

- Dasanayaka, L. and Yapa, P. (2009). Role of plume dynamics phase in a deepwater oil and gas release model, Journal of Hydro-Environment Research **2**: 243–253.
- Davidson, M. and Pun, K. (1999). Weakly Advected Jets in Cross-Flow, Journal of Hydraulic Engineering **125**: 47–58.
- Davies, E., Nimmo-Smith, W., Agrawal, Y. and Souza, A. (2012). LISST-100 response to large particles, Marine Geology **307-310**: 117–122.
- Englezos, P. (1993). Clathrate Hydrates, Ind. Eng. Chem. **32**: 1251–1274.
- Fanneløp, T. and Sjøen, K. (1980). Hydrodynamics of underwater blowouts, Technical report, The Ship Research Institute of Norway.
- Fingas, M., Fieldhouse, B. and Mullin, J. (1996). Studies of Water-in-Oil Emulsions - Stability Studies, Spill Science & Technology Bulletin **3**(4): 189–190.
- French-McCay, D. (2004). Oil Spill Impact Modeling: Development and Validation, Environmental Toxicology and Chemistry **23**(10): 2441–2456.
- Fry, D. and Adams, E. (1983). Confined Radial Buoyant Jet, Journal of Hydraulic Engineering **109**: 1185–1202.
- Gould, T., Tek, M. and Katz, D. (1974). Two-Phase Flow Through Vertical, Inclined, or Curved Pipe, Journal of Petroleum Technology **26**: 915–926.
- Green, D. and Perry, R. (2007). Perry's Chemical Engineers' Handbook, McGraw-Hill.
- Hiemenz, P. and Rajagopalan, R. (1997). Principles of Colloid and Surface Chemistry, Taylor & Francis Group.
- Hinze, J. (1955). Fundamentals of the Hydrodynamic Mechanism of Splitting in Dispersion Processes, A.I.Ch.E. Journal **1**(3): 289–295.
- Hu, S. and Kintner, R. (1955). The Fall of Single Liquid Drops through Water, A.I.Ch.E. Journal **1**(1): 42–48.
- Infield Systems (2013). Definition of a Deepwater Field Development, <http://www.deepwater.co.uk/info.htm>.
- Jakobsen, H. (2008). Chemical Reactor Modeling, Springer.

- Johansen, Ø. (2000). DeepBlow - A Lagrangian Plume Model for Deep Water Blowouts, Spill Science & Technology Bulletin **6**(2): 103–111.
- Johansen, Ø. (2003). Development and verification of deep-water blowout models., Marine Pollution Bulletin **47**: 360–368.
- Johansen, Ø., Brandvik, P. and Farooq, U. (2012). Droplet breakup in subsea oil releases, Part 2 - Predictions of droplet size distributions with and without injection of chemical dispersants, Submitted to Marine Pollution Bulletin October 2012 .
- Johansen, Ø. and Durgut, I. (2006). Implementation of the near-field module in the ERMS model, Technical report, SINTEF.
- Johansen, Ø., Rye, H. and Cooper, C. (2003). Deep Spill - Field study of a simulated oil and gas blow-out in deep water, Spill Science & Technology Bulletin **8**: 433–443.
- Khelifa, A., Fingas, M., Hollebone, B. and Brown, C. (n.d.). Effects of Chemical Dispersants on Oil Physical Properties and Dispersion, Technical report, Emergencies Science and Technology Divison, Environmental Science and Technology Centre, Science and Technology Branch, Environment Canada.
- Kujawinski, E., Soule, M., Valentine, D., Boysen, A., Longnecker, K. and Redmond, M. (2011). Fate of Dispersants Associated with Deepwater Horizon Oil Spill, Environmental Science and Technology **45**: 1298–1306.
- Lane, J. and Labelle, R. (2000). Meeting the Challenge of Potential Deepwater Spills: Cooperative Research Effort Between Industry and Government, SPE International Conference on Health, Safety, and the Environment on Oil and Gas Exploration and Production.
- Lee, J. and Cheung, V. (1990). Generalized Lagrangian Model for Buoyant Jets in Current, J. Environ. Eng. **116**: 1085–1106.
- Li, M. and Garrett, C. (1998). The Relationship Between Oil Droplet Size and Upper Ocean Turbulence, Marine Pollution Bulletin **36**: 961–970.
- Lin, S. and Lian, Z. (1998). Mechanisms of the Breakup of Liquid Jets, AIAA Journal **28**(1): 120–126.

REFERENCES

- Maini, B. and Bishnoi, P. (1981). Experimental investigation of hydrate formation behaviour of a natural gas bubble in a simulated deep sea environment, Chemical Engineering Science **36**: 183–189.
- Masutani, S. and Adams, E. (2001). Experimental Study of Multi-Phase Plumes with Application to Deep Ocean Spills, Final Report to the MMS (the U.S. Dept. of the Interior by Univ. of Hawaii/Massachusetts Inst. of Technology).
- McCain Jr., W. (1990). The Properties of Petroleum Fluids, PennWell Publishing Company.
- Mukherjee, B. and Wrenn, B. (2011). Effects of Physical Properties and Dispersion Conditions on the Chemical Dispersion of Crude Oil, Environmental Engineering Science **28**(4): 263–273.
- Ogawa, K., Sha, Z., Palosaari, S. and Ok, T. (2001). Size Distribution Function of Droplet in Liquid-Liquid Mixing and Bubble in Gas-Liquid Mixing, Crystal in Crystallization and Crushed Product in Crushing, Journal of Chemical Engineering of Japan **34**(5): 627–633.
- Oxford Dictionaries (2013). Plume, <http://oxforddictionaries.com/definition/english/plume>.
- Reed, M., Johansen, Ø., Brandvik, P., Daling, P., Lewis, A., Fiocco, R., Mackay, D. and Prentk, R. (1999). Oil Spill Modeling towards the Close of the 20th Century: Overview of the State of the Art, Spill Science & Technology Bulletin **5**: 3–16.
- Republic of the Marshall Islands Maritime Administrator (2011). Deepwater Horizon Marine Casualty Investigation Report, Technical report, Office of the Maritime Administrator.
- Ryan, J., Zhang, Y., Thomas, H., Rienecker, E. and Cummings, R. N. S. (2010). A High-Resolution Survey of a Deep Hydrocarbon Plume in the Gulf of Mexico during the 2010 Macondo Blowout, Technical report, American Geophysical Union.
- Rye, H. and Brandvik, P. (1997). Verification of Subsurface Oil Spill Models, 1997 International Oil Spill Conference.

- Rye, H., Brandvik, P. and Strøm, T. (1997). Subsurface Blowouts: Results from Field Experiments, Spill Science & Technology Bulletin **4**(4): 239–256.
- Rye, H., Nordtug, T. and Skognes, K. (2003). Spredning og deponering av kaks og slam. Spredning av produsert vann med doser på organismer. Spredning av radioaktivitet. OED studie 5a og 5b - Lofoten-Barentshavet., Technical report, SINTEF Materialer og Kjemi. Marin Miljøteknologi.
- Seol, D., Bryant, D. and Socolofsky, S. (2009). Measurement of Behavioral Properties of Entrained Ambient Water in a Stratified Bubble Plume, Journal of Hydraulic Engineering **135**(11): 983–988.
- Sequoia Scientific, Inc. (2012). LISST-100X Particle Size Analyzer User's Manual.
- SINTEF Marine Modeling Group (2012). Userguide MEMW 6.2, SINTEF Materials and Chemistry.
- S.L Ross Enviromental Research Ltd. (1997). Fate and Behavior of Deepwater Subsea Oil Well Blowouts in the Gulf of Mexico, Technical report, for Minerals Management Service.
- Socolofsky, S. (2001). Laboratory Experiments of Multi-phase Plumes in Stratification and Crossflow, PhD thesis, Massachusetts Institute of Technology.
- Socolofsky, S. and Adams, E. (2003). Liquid Volume Fluxes in Stratified Multiphase Plumes, Journal of Hydraulic Engineering **129**(11): 905–914.
- Socolofsky, S. and Adams, E. (2005). Role of Slip Velocity in the Behavior of Stratified Multiphase Plumes, Journal of Hydraulic Engineering **131**(4): 273–282.
- Socolofsky, S., Bhaumik, T. and Seol, D. (2008). Double-Plume Integral Models for Near-Field Mixing in Multiphase Plumes, Journal of Hydraulic Engineering **134**(6): 772–783.
- Spaulding, M., Bishnoi, P., Anderson, E. and Isaji, T. (n.d.). An Integrated Model for Prediction of Oil Transport from a Deep Water Blowout, Technical report, University of Rhode Island.

REFERENCES

- Sørheim, K., Leirvik, F. and Brandvik, P. (2010a). Kartlegging av forvittringsegenskaper av Norne Blend, Stær, Svale og Alve samt effekt av voks-inhibitor på Norne Blend, SINTEF report pp. 1–122.
- Sørheim, K., Leirvik, F. and Brandvik, P. (2010b). Mapping of weathering characteristics of Norne Blend, Stær, Svale and Alve as well as the effect of wax inhibitors on Norne Blend, Sintef report, translated from Norwegian to English pp. 1–122.
- Sterling Jr., M., Bonner, J., Ernest, A., Page, C. and Autenrieth, R. (2004). Chemical dispersant effectiveness testing: influence of droplet coalescence, Marine Pollution Bulletin **48**: 969–977.
- Strøm-Kristiansen, T., Daling, P., Hokstad, J. and Singsaas, I. (1997). Weathering and dispersion of naphthenic, asphaltenic and waxy crude oils, 1997 International Oil Spill Conference.
- Thibodeaux, L., Valsaraj, K., John, V., Papadopoulos, K., Pratt, L. and Pesika, N. (2011). Marine Oil Fate Knowledge Gaps, Basic Research, and Development Needs, Environmental Engineering Science **28**: 87–93.
- Topham, D. (1975). Hydrodynamics of an Oilwell Blowout, Technical report, Beaufort Sea Project, Technical Report No. 33.
- Topham, D. (1984). The Modeling of Hydrocarbon Bubble Plumes to Include Gas Hydrate Formation, Chemical Engineering Science **39**(11): 1613–1622.
- United States Government Accountability Office (2012). Oil Dispersants: Additional Research Needed, Particularly on Subsurface and Arctic Applications, Technical report, Report to Congressional Requesters.
- Viades-Trejo, J. and Gracia-Fadrique, J. (2007). Spinning drop method From Young-Laplace to Vonnegut, Colloids and Surfaces, A: Physicochemical and Engineering Aspects **302**: 549–552.
- Wang, C. and Calabrese, R. (1986). Drop Breakup in Turbulent Stirred-Tank Contactors. Part II: Relative Influence of Viscosity and Interfacial Tension, A.I.Ch.E. Journal **32**(4): 667–676.

- Yapa, P. (2003). A Module for NOAA's GNOME Model to Provide Capability to Simulate Deepwater Oil and Gas spills, Final Report to The Cooperative Institute for Coastal and Estuarine Environmental Technology (CICEET) .
- Yapa, P. (2013). CDOG (Comprehensive Deepwater Oil and Gas) Model, <http://www.clarkson.edu/cee/faculty/yapa.html>.
- Yapa, P. and Chen, F. (2004). Behavior of Oil and Gas from Deepwater Blowouts, Journal of Hydraulic Engineering **130**: 540–533.
- Yapa, P. and Li, Z. (1997). Simulation of oil spills from underwater accidents I: Model development, Journal of Hydraulic Research **35**(5): 673–688.
- Yapa, P. and Li, Z. (1998). Simulation of oil spills from underwater accidents II: Model verification, Journal of Hydraulic Research **36**(1): 117–134.
- Yapa, P., Wimalaratne, M., Dissanayake, A. and DeGraff Jr., J. (2012). How does oil behave when released in deepwater?, Journal of Hydro-Environment Research **6**: 275–285.
- Yapa, P. and Xie, H. (2002). Modeling Underwater Oil/Gas Jets and Plumes: Comparison with Field Data, Journal of Hydraulic Engineering **125**: 855–860.
- Yapa, P. and Zheng, L. (1997). Modelling Oil and Gas Releases from Deep Water: A Review, Spill Science & Technology Bulletin **4**(4): 189–198.
- Yapa, P., Zheng, L. and Chen, F. (2001). A Model for Deepwater Oil/Gas Blowouts, Marine Pollution Bulletin **43**: 234–241.
- Yapa, P., Zheng, L. and Nakata, K. (1999). Modeling Underwater Oil/Gas Jets and Plumes, Journal of Hydraulic Engineering **125**: 481–491.
- Zheng, L. and Yapa, P. (2000). Bouyant Velocity of Spherical and Nonspherical Bubbles/Droplets, Journal of Hydraulic Engineering **126**: 852–854.
- Zheng, L., Yapa, P. and Chen, F. (2002). A model for simulating deepwater oil and gas blowouts - Part I: Theory and model formulation, Journal of Hydraulic Research **41**(4): 339–351.

A Additional Information Theory

A complete method on how to derive a droplet size distribution is presented in the following, together with a section on calculation of shear rate and a section with requirements for a dispersant on how to enhance the formation of oil droplets.

A.1 Derivation of a Droplet Size Distribution

An article written by Chen and Yapa (2007) describes a thorough method on how to determine the droplet size distribution of oil droplets. A summary of the equations required for it, will be presented in the following appendix. The earlier defined oil droplet diameter, d is replaced by δ through the whole appendix.

The probability density function, PDF, must be connected with a characteristic size in order to estimate the droplet size distribution for a spill model. If there is a wide distribution of droplets, then it is best described by mean diameters, see Equation (A.1).

$$\delta_{qp}^{(q-p)} = \frac{\int_0^{\infty} f \cdot \delta^q d\delta}{\int_0^{\infty} f \cdot \delta^p d\delta} \quad (\text{A.1})$$

where f is the probability density function, δ is droplet size and $p = 2$ or 0 , $q = 1, 2$ or 3 . These are the most common values for p and q .

To calculate the mass mean volume-equivalent diameter of oil droplets, δ_{30} , Equation (A.2) is utilized. The Sauter mean diameter, δ_{32} , also called the volume-surface diameter, is calculated by Equation (A.3).

$$\delta_{30} = \left(\int_0^{\delta_{\max}} f \cdot \delta^3 d\delta \right)^{1/3} \quad (\text{A.2})$$

$$\delta_{32} = \left(\int_0^{\delta_{\max}} f \cdot \delta^2 d\delta \right)^{-1} \delta_{30}^3 \quad (\text{A.3})$$

$$(\text{A.4})$$

A.1.1 Maximum Entropy Formalism Model for Oil Droplet Size Distribution

A model for the PDF for oil droplet size distribution is the maximum entropy formalism, MEF, model. The statistical inference method provides the least biased estimate of a probability distribution. In order to obtain an accurate distribution of droplets, physical conservation principles are utilized with a set of constraint equations (Chen and Yapa, 2007).

The continuous integral form of the constraint equations are utilized. The normalization constraint is presented in Equation (A.5).

$$\iint f \cdot d\delta^* du^* = 1 \quad (\text{A.5})$$

where $f = f(\delta^*, u^*)$ is the joint PDF, $\delta^* = \delta/\delta_{30}$ is the non-dimensional droplet diameter, $u^* = u/U_0$ is the non-dimensional droplet velocity and U_0 is the jet release velocity.

Conservation of mass is presented in Equation (A.6), where S_m is the source term for mass conservation.

$$\iint f \cdot \delta^{*3} d\delta^* du^* = 1 + S_m \quad (\text{A.6})$$

Conservation of momentum is presented in Equation (A.7), where S_{mv} is the source term for momentum constraint. The term accounts for the momentum flux exchanged with the ambient fluid.

$$\iint f \cdot \delta^{*3} d\delta^* du^* = 1 + S_{mv} \quad (\text{A.7})$$

Conservation of surface and kinetic energy is presented in Equation (A.8), where S_e is the source term for energy conservation. The term accounts for the energy flux transferred into ambient fluid.

$$\iint f \cdot (\delta^{*3} u^{*2} + \delta^{*2} B) d\delta^* du^* = 1 + S_e \quad (\text{A.8})$$

where B is defined by;

$$B = \frac{2s}{We} \quad (A.9)$$

and where s is a shape factor, defined in Equation (A.10). The Weber number, We , is defined in Equation (A.11).

$$s = \frac{A}{V} \cdot \delta \quad (A.10)$$

where A is surface area and V is volume of a droplet. For a spherical shape, S_m is assumed to be zero and $s = 6$.

$$We = \frac{\rho_{oil} U_0^2 \delta_{30}}{\sigma} \quad (A.11)$$

where ρ_{oil} is the oil density, U_0 is initial velocity of oil and σ is interfacial tension between oil and water.

The PDF is found by maximizing Shannon's entropy, see Equation (A.12).

$$S = -k \cdot \int f(\delta^*, u^*) \cdot \ln(f(\delta^*, u^*)) d\delta^* du^* \quad (A.12)$$

If Shannon's entropy is maximized with $k = 1$ and with the constraints in Equations (A.5) to (A.8), the joint PDF will have the form presented in Equation (A.13).

$$f = 3\delta^{*2} \exp \left[-\lambda_0 - \lambda_1 \delta^{*3} - \lambda_2 \delta^{*3} u^* - \lambda_3 (\delta^{*3} u^{*2} + \delta^{*2} B) \right] \quad (A.13)$$

The Lagrangian multiplier, λ_i , must be evaluated by solving the above constraints, then Equation (A.13) can be integrated over the velocity axis, du , to obtain the number-based droplet size distribution. With boundaries from minimum to maximum normalized droplet velocity, the equation becomes as presented in Equation (A.14).

$$\begin{aligned} f_N &= \frac{dN}{d\delta^*} = \int_{u_{min}^*}^{u_{max}^*} f du^* \\ &= \frac{3}{2} \left(\frac{\pi \delta^*}{\lambda_3} \right) \cdot A(\delta^*) \exp \left[-\lambda_0 - \lambda_3 B \delta^{*2} - \left(\lambda_1 - \frac{\lambda_2^2}{\lambda_3} \right) \delta^{*3} \right] \end{aligned} \quad (A.14)$$

where

$$A(\delta^*) = \operatorname{erf} \left[\left(u_{\max}^* - \frac{\lambda_2}{2\lambda_3} \right) \sqrt{\lambda_3 \delta^{*3}} \right] - \operatorname{erf} \left(\left(u_{\min}^* - \frac{\lambda_2}{2\lambda_3} \right) \sqrt{\lambda_3 \delta^{*3}} \right) \quad (\text{A.15})$$

where $\operatorname{erf}()$ is the error function and the minimum velocity is set to zero. The upper integration limit domain must be chosen in such a way that the PDF at the limit of integration approaches zero.

When a number-based PDF is obtained, it is possible to find the volume-based PDF. In Equation (A.16) it is assumed spherical droplets, thus the volume of the droplets is proportional to δ^3 .

$$f_V = \frac{\delta^3}{\delta_{30}^3} f_N = \delta^{*3} f_N \quad (\text{A.16})$$

A.1.1.1 Numerical procedure for solving the PDF

For solving the PDF numerical, five steps have to be followed:

1. Estimate the constraints in the source terms with conditions at the release point.
2. Calculate the mass mean diameter, δ_{30} , based on earlier information.
3. Calculate the Weber number with respect to δ_{30} .
4. Solve Equations (A.5) to (A.8) for the four Lagrangian multipliers, λ_i , with a modified Newton-Raphson method.
5. Calculate the droplet size distribution with Equations (A.14) and (A.16).

The conditions in Equation (A.17) usually have to be satisfied for the initial guess of λ_i (Chen and Yapa, 2007).

$$\lambda_1 > 0, \quad \lambda_2 < 0, \quad \lambda_3 > 0, \quad \lambda_1 + \lambda_3 > |\lambda_2| \quad (\text{A.17})$$

A.1.2 Simplified Maximum Entropy Formalism-Based Models

The MEF model for oil droplet size distributions yields reasonable results for several cases, however it has disadvantages which are listed below (Chen and Yapa, 2007).

- Difficult to define the full set of constraints and they may be inaccurate.
- A challenge to obtain convergence, especially if the number of equations with constraints are increased.
- Difficulties with defining constraint equations for each case.
- An implicit relationship between model and parameters. Leads to difficulties with the understanding of certain parameters.

A simplified model with mass balance as basis is presented in the next paragraph, Model 1.

A.1.2.1 Model 1: Conservation of mass

The solution of the number-based PDF can be obtained by utilizing the constraints from Equations (A.5) and (A.6). It results in the following, with $\lambda_0 = 0$ and $\lambda_1 = 1$;

$$f_N = \frac{dN}{d\delta^*} = 3\delta^{*2} \exp(-\delta^{*3}) \quad (\text{A.18})$$

Utilizing the Sauter mean diameter in Equation (A.18), Equation (A.19) can be obtained (Chen and Yapa, 2007).

$$f_N = \frac{dN}{d\bar{\delta}} = 3C_1 \bar{\delta}^2 \exp(-C_2 \bar{\delta}^3) \quad (\text{A.19})$$

where

$$\begin{aligned} \bar{\delta} &= \frac{\delta}{\delta_{32}} \\ \delta_{32} &= A \cdot \delta_{30} \\ \delta^* &= A \cdot \bar{\delta} \\ C_1 &= A^2 \quad \text{and} \quad C_2 = A^3 \end{aligned}$$

The distribution presented in Equation (A.18) has the same form as a Nukiyama and Tanasawa number-based distribution, see Equation (A.20) (Chen and Yapa, 2007).

$$f_N = \frac{dN}{d\delta} = B\delta^m \exp[-C\delta^q] \quad (\text{A.20})$$

where m is usually equal to two, B , C and q are constants.

Equation (A.18) has similarities with the Rosin-Rammler distribution. The volume-based Rosin-Rammler distribution function is presented in Equation (A.21) (Chen and Yapa, 2007).

$$\Phi(\delta) = 1 - \exp\left[-C' \left(\frac{\delta}{\delta_c}\right)^q\right] \quad (\text{A.21})$$

where $\Phi(\delta)$ is the fraction contained in drops of diameter less than δ , δ_c is characteristic droplet size and C' is a constant related to δ_c .

The volume-based size distribution is presented in Equation (A.22), where $\delta^* = \delta/\delta_c$.

$$f_V = \frac{dV}{d\delta^*} = C'q(\delta^*)^{q-1} \exp[-C\delta^q] \quad (\text{A.22})$$

The Rosin-Rammler number-based size distribution is presented in Equation (A.23).

$$f_N = \frac{dN}{d\delta^*} = C'q(\delta^*)^{q-4} \exp[-C\delta^q] \quad (\text{A.23})$$

Equation (A.18), (A.20) and (A.23), have the same form, however with different parameters. Since the equations have these similarities, it is reasonable to say that both the Nukiyama and Tanasawa model, and the Rosin-Rammler model can be derived by using the MEF model.

A.1.2.2 Model 2: Averaged specific surface area

A simplified model with the averaged specific surface area as basis is presented below.

Assuming a spherical droplet with size δ . Then the specific surface area is proportional to δ^{-1} . A proposed model is to assume an averaged value of δ^{-1} for the whole system with quasi-steady conditions. This is $1/\delta_{32}$, presented in Equation (A.24) and was

proposed by Ogawa, Sha, Palosaari and Ok (2001).

$$\int_0^{\infty} f\left(\frac{1}{\delta}\right) \left(\frac{1}{\delta}\right) d\left(\frac{1}{\delta}\right) = \frac{1}{\delta_{32}} \quad (\text{A.24})$$

The normalization condition utilized to be able to apply the MEF approach is presented in Equation (A.25). Shannon's entropy, S , for the simplified model is presented in Equation (A.26).

$$\int_0^{\infty} f\left(\frac{1}{\delta}\right) d\left(\frac{1}{\delta}\right) = 1 \quad (\text{A.25})$$

$$S = -k \int_0^{\infty} f\left(\frac{1}{\delta}\right) \ln \left[f\left(\frac{1}{\delta}\right) \right] d\left(\frac{1}{\delta}\right) \quad (\text{A.26})$$

An estimate of the PDF, f_{L0} , is found by maximizing S , with $k = 1$, and utilizing the constraints in Equations (A.24) and (A.25). The result is presented in Equation (A.27).

$$f_{L0}\left(\frac{1}{\delta}\right) = \delta_{32} \cdot \exp\left(-\frac{\delta_{32}}{\delta}\right) \quad (\text{A.27})$$

The equation above is not realistic since it states that larger droplets always has a larger probability. The statement is not true, however it is more reasonable that the probability of larger droplets is always smaller. It results in Equation (A.28) which is based on δ_{32} and the oil droplet number. B' and C' are two adjustable parameters.

$$f_L = \frac{dN}{d\delta} = \delta_{32} \cdot \exp\left(-\frac{\delta_{32}}{\delta}\right) \left[-B' \left(\frac{\delta}{\delta_{32}}\right)^{C'} \right] \quad (\text{A.28})$$

The droplet size is normalized by replacing δ_{32} with δ_{30} , then Equation (A.29) is obtained.

$$f_N = \frac{dN}{d\delta^*} = A \cdot \exp\left[-\frac{1}{\delta^*} - B \cdot \delta^{*C}\right] \quad (\text{A.29})$$

where f_N is a number based PDF, $\delta^* = \delta/\delta_{30}$ and A is a parameter to account for the normalization condition, $\int f_N d\delta^*$.

Since there are two tuning parameters, B and C , in Equation (A.29) it is easier to fit experimental data than in the first simplified model. These two tuning parameters can be dependent of other variables, e.g. surface tension, release velocity or viscosity of liquid. More details for the parameters are found in (Chen and Yapa, 2007).

In (Li and Garrett, 1998) a relationship between oil droplet size and upper ocean turbulence is discussed. A couple of the equations utilized in the scientific paper can be related to the equations utilized in above to calculate the oil droplet sizes from a jet/plume.

A.2 Shear Rate

The shear rate inside a pipe can be calculated by Equation (A.30) and the method is described in more detail in (Darby, 2001).

$$\dot{\gamma} = \frac{8u}{d} \quad (\text{A.30})$$

where $\dot{\gamma}$ is the shear rate, u is linear fluid velocity and d is inner diameter of pipe. The linear fluid velocity is calculated by Equation (A.31).

$$u = \frac{Q}{A} \quad \text{where} \quad A = \pi r^2 \quad (\text{A.31})$$

where Q is volumetric flow rate, A is cross-sectional area of pipe and r is inner radius of the pipe. Equation (A.30) can be simplified to Equation (A.32), and will then only be dependent of flow rate and radius.

$$\dot{\gamma} = \frac{4Q}{\pi r^3} \quad (\text{A.32})$$

A.3 Dispersant Requirements

Seven requirements for a chemical dispersant to enhance the formation of oil droplets according to Committee on Understanding Oil Spill Dispersants: Efficacy and Effects (2005) are:

1. The dispersant must hit the target oil at the desired dosage.
2. The surfactant molecules in the dispersant must have enough time to penetrate and mix into the oil.
3. The surfactant molecules must orient at the oil-water interface with the lipophilic groups in the oil phase and the hydrophilic groups in the water phase.
4. The oil-water interfacial tension must decrease due to the presence of surfactant molecules at the oil-water interface, thereby weakening the cohesive strength of the oil film.
5. Sufficient mixing energy must be applied at the oil-water interface, by wind and/or wave action, to allow generation of smaller droplets, with a concomitant increase in interfacial surface area.
6. The droplets must be dispersed throughout the water column by a combination of advective and diffusive processes to minimize droplet-droplet collisions and coalescence to form larger droplets. The larger droplets can resurface in the absence of continued turbulence.
7. After entrainment, the droplets must be diluted to nontoxic concentrations and remain suspended in the water column long enough for the majority of the oil to be biodegraded.

B Additional Information Simulations and Laboratory Experiments

B.1 Input Data to MEMW

- **Simulation Information**

- **Start time:** May 1, 2000, due to the limited amount of current data available.
- **Duration of simulation:** Twelve hours.

- **Release Information**

- **Selected site:** Norne field, 66°2'N 8°5'E, approximately at 370 meters sea-water depth.
- **Profile:** Change between Alve, Norne and Svale with their respective composition files. Exception for Norne where the composition file for Norne Blend is utilized, due to it does not exist a composition file for Norne.
- **Release rate:** Default is 4800m³/d. 7200m³/d and 9600m³/d are also utilized.
- **Duration of release:** Twelve hours.
- **Depth:** One meter above sea floor.

- **Near Field Model**

- **Near field model:** Plume3D
- **Release diameter:** 120 mm.
- **Gas/Liquid ratio:** 0, 100, 200 and 400. Where e.g. 960000Sm³/d gas is equivalent to 4800m³/d oil release for a GOR of 200.
- **Gas density:** Default value of 0.8kg/Sm³.
- **Hydrate formation:** Neglected.

- **Oil/Water Tension [N/m]:** Standard value utilized will be 20mN/m, not the default of 30mN/m. The value is assumed to be 200 times smaller when dispersant is utilized, hence the value utilized if dispersant is present is 0.1 mN/m.

- **Environmental Parameters**

- **Grid:** A grid size of 200x153 will be utilized.
- **Wind:** No wind, because then the quantity of liquid droplets in the water column will not be affected of entrained droplets from the surface.
- **Current:** dmni_2000_4km.dir, found in the basic edition of MEMW.
- **Salinity and temperature profile:** Actual profiles for the Norne field, described more closely in Appendix B.2.

- **Model Parameters**

- **Liquid/Solid particles:** 30 000, maximum allowed.
- **Dissolved particles:** 30 000, maximum allowed.
- **Gas particles:** 30 000, maximum allowed and is only applicable for MEMW v6.5 β .
- **Concentration grid:** 200x153x10, the same size as the grid in environmental parameters and the Z direction is divided in 10 layers.
- **Surface grid dimensions:** 200x153, the same size as the grid in environmental parameters.
- **Concentration grid depth:** Min: 0, Max: 400.
- **Output interval:** One hour, i.e. write data to log file every hour.
- **Time step:** Five minutes, i.e. the model does calculations every fifth minute.

The values not discussed above, the default values from MEMW will be utilized.

B.2 Salinity and Temperature Profile

The temperature and salinity profile utilized as input data in the simulations at the Norne field are found in Rye, Nordtug and Skognes (2003). Figures B.1 and B.2 are the same as from an article by Rye et al. (2003). The figures are reproduced with the hydrographic data from Henrik Rye at SINTEF (personal communication).

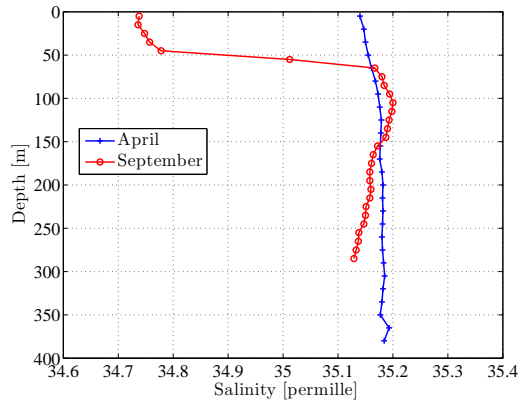


Figure B.1: Salinity profile for the Norne field, Rye et al. (2003).

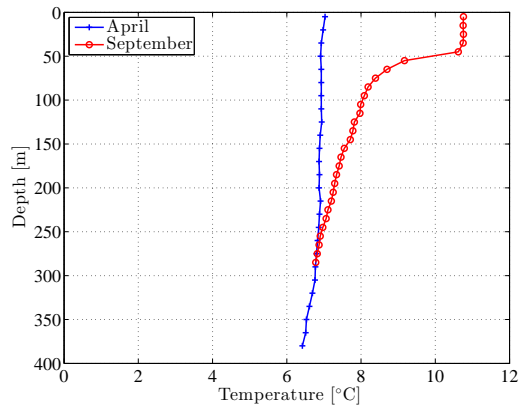


Figure B.2: Temperature profile for the Norne field, Rye et al. (2003).

B.3 Size Ranges for LISST-100X Type C

Table B.1: Size ranges for spherical particle inversion method for the LISST-100X Type C (Sequoia Scientific, Inc., 2012).

Size bin number	Lower [μm]	Upper [μm]	Median [μm]
1	2.50	2.95	2.72
2	2.95	3.48	3.20
3	3.48	4.11	3.78
4	4.11	4.85	4.46
5	4.85	5.72	5.27
6	5.72	6.75	6.21
7	6.75	7.97	7.33
8	7.97	9.4	8.65
9	9.4	11.1	10.2
10	11.1	13.1	12.1
11	13.1	15.4	14.2
12	15.4	18.2	16.8
13	18.2	21.5	19.8
14	21.5	25.4	23.4
15	25.4	30.0	27.6
16	30.0	35.4	32.5
17	35.4	41.7	38.4
18	41.7	49.2	45.3
19	49.2	58.1	53.5
20	58.1	68.6	63.1
21	68.6	80.9	74.5
22	80.9	95.5	87.9
23	95.5	113	104
24	113	133	122
25	133	157	144
26	157	185	170
27	185	218	201
28	218	258	237
29	258	304	280
30	304	359	331
31	359	424	390
32	424	500	460

C Additional Information Results

The appendix contains additional information to section 5 Results. The subsections are named analogous to the results section. Here, extra figures and tables are presented to support the already presented data. In addition a complete table of droplet size raw data is included. A graph from the IFT measurements and a graph from the viscosity measurements are attached, as well.

C.1 Comparison of Oil Types

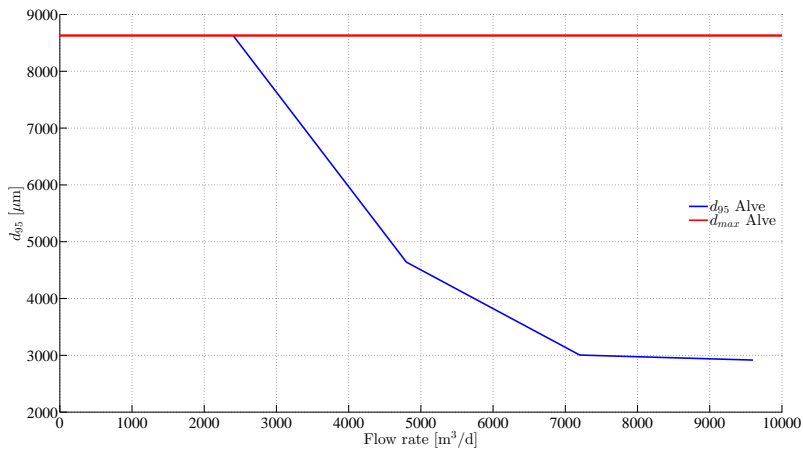


Figure C.1: d_{95} as a function of flow rate, blue line, and d_{max} is the asymptote, red line.

C.2 Flow Rate

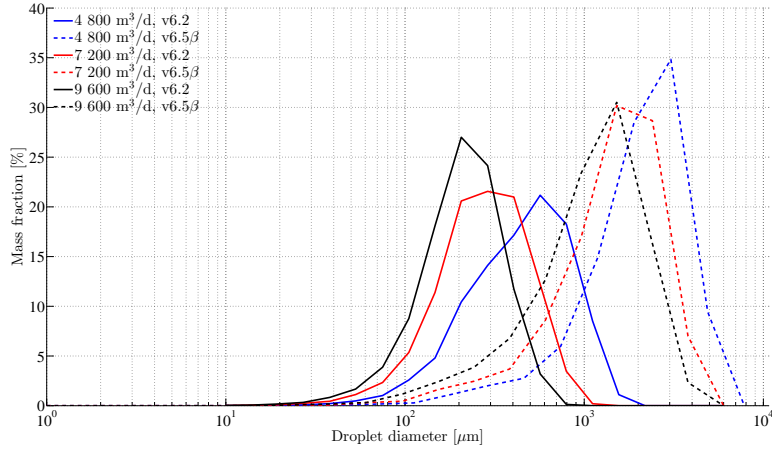


Figure C.2: Svale: Droplet size distributions at three different flow rates; 4800, 7200 and 9600 m³/d. Simulations with MEMW v6.2 are showed with solid lines and simulations with MEMW v6.5β are showed with dashed lines.

Table C.1: Svale: Droplet sizes for three different flow rates. The peak value, d_{peak} , and d_{95} are presented for MEMW v6.2. The same values are presented for MEMW v6.5β together with the maximum stable droplet size, d_{max} . All droplet sizes in μm.

Rate [m³/d]	MEMW v6.2		MEMW v6.5β		
	d_{peak}	d_{95}	d_{peak}	d_{95}	d_{max}
4800	568	1891	3046	7827	10719
7200	289	1162	1519	5518	10719
9600	206	823	1519	4313	10719

C.3 Effect of Dispersant

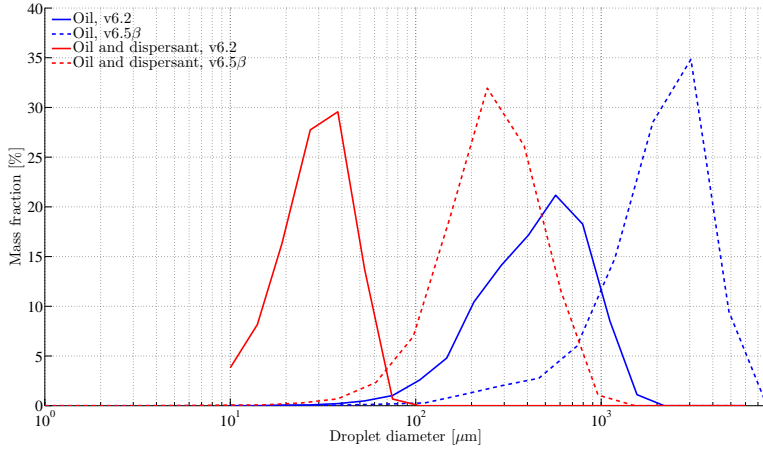


Figure C.3: Svale: Droplet size distributions without and with dispersant. Without dispersant are blue lines, and with dispersant are red lines. Simulations with MEMW v6.2 are showed with solid lines and simulations with MEMW v6.5 β are showed with dashed lines.

Table C.2: Svale: Droplet sizes for simulations with and without dispersant. The peak value, d_{peak} , and d_{95} are presented for MEMW v6.2. The same values are presented for MEMW v6.5 β together with the maximum stable droplet size, d_{max} . All droplet sizes in μm .

IFT [mN/m]	MEMW v6.2		MEMW v6.5 β		
	d_{peak}	d_{95}	d_{peak}	d_{95}	d_{max}
20	568	1891	3046	7827	10719
1	38	79	243	1110	1110

C.4 Dispersant-to-Oil Ratio

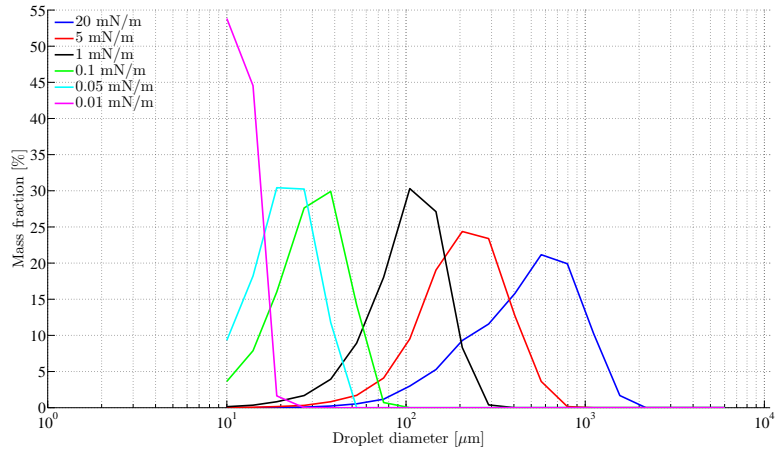


Figure C.4: Alve: Droplet size distributions for six different IFT values at a flow rate of $4800 \text{ m}^3/\text{d}$. Simulations with MEMW v6.2 are showed with solid lines.

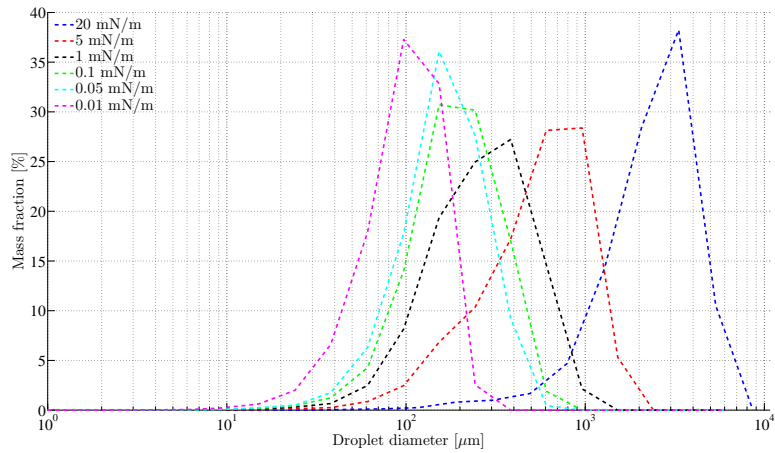


Figure C.5: Alve: Droplet size distributions for six different IFT values at a flow rate of $4800 \text{ m}^3/\text{d}$. Simulations with MEMW v6.5 β are showed with dashed lines.

Table C.3: Alve: Droplet sizes for simulations with different DOR at a flow rate of $4800\text{m}^3/\text{d}$. The peak value, d_{peak} , and d_{95} are presented for MEMW v6.2. The same values are presented for MEMW v6.5 β together with the maximum stable droplet size, d_{max} . All droplet sizes in μm .

IFT [mN/m]	MEMW v6.2		MEMW v6.5 β		
	d_{peak}	d_{95}	d_{peak}	d_{95}	d_{max}
20	568	1891	3324	4640	8630
5	206	823	961	2245	4768
1	105	313	384	1184	2394
0.1	38	79	153	814	894
0.05	19	52	153	664	664
0.01	10	20	97	334	334

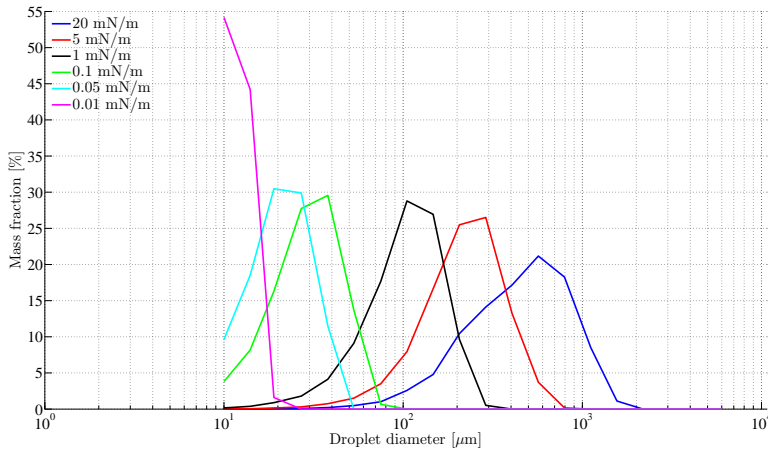


Figure C.6: Svale: Droplet size distributions for six different IFT values at a flow rate of $4800\text{m}^3/\text{d}$. Simulations with MEMW v6.2 are showed with solid lines.

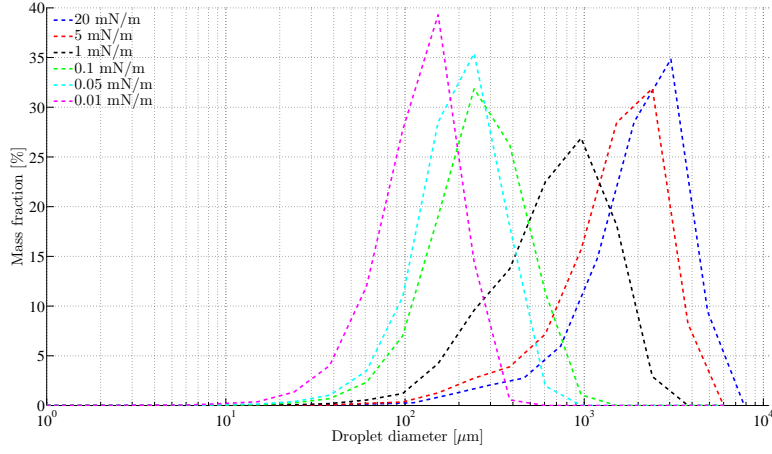


Figure C.7: Svale: Droplet size distributions for six different IFT values at a flow rate of $4800\text{m}^3/\text{d}$. Simulations with MEMW v6.5 β are showed with dashed lines.

Table C.4: Svale: Droplet sizes for simulations with different DOR. The peak value, d_{peak} , and d_{95} are presented for MEMW v6.2. The same values are presented for MEMW v6.5 β together with the maximum stable droplet size, d_{max} . All droplet sizes in μm .

IFT [mN/m]	MEMW v6.2		MEMW v6.5 β		
	d_{peak}	d_{95}	d_{peak}	d_{95}	d_{max}
20	568	1891	3046	7827	10719
5	289	823	2401	5922	5922
1	185	313	961	2974	2974
0.1	38	79	243	1110	1110
0.05	19	52	243	825	825
0.01	10	20	153	414	414

C.5 Droplet Size Raw Data for Simulations

Table C.5 contains all the raw data information available in the two log files, .prt and .p3d, from MEMW for droplet sizes that characterizes the oil droplet size distribution functions. The interpretation of the different droplet sizes are:

- $d_{95,\max}$ is the 95 % maximum droplet size from the .prt log file. It is the same number as $d_{95,\text{old}}$, from the .p3d log file from MEMW v6.5 β , for MEMW v6.2.
- $d_{95,\text{old}}$ is calculated in MEMW v6.5 β and is utilized for comparison with the new calculated droplet size.
- d_{peak} is the peak value from a graph and is the bin with the largest percentage of oil droplets.
- d_{\max} is presented in the .p3d log file from MEMW v6.5 β and is the largest stable droplet size. It is calculated by a correlation presented by Hu and Kintner (1955).
- d_{char} is a characteristic size that MEMW calculates internally, however it is not describing the oil droplet size distribution correctly and will not be utilized further.

Table C.5: Raw data with droplet sizes from log files. All droplet sizes in μm .

	MEMW v6.2			MEMW v6.2 beta					
	d _{char}	d _{95,max}	d _{peak}	d _{95,old}	d ₉₅	d _{peak}			
Comparison of oil types, 4800m ³ /d	Svale	883	1891	568	1891	7827	3640	7827	3046
	Alve	883	1891	568	1891	4640	8630	2158	4640
	Norne	883	1891	568	1891	10003	10003	4651	10003
Effect of dispersant, 4800m ³ /d	Svale IFT 20mN/m	883	1891	568	1891	7827	10719	3640	7827
	Svale IFT 0.1mN/m	41	79	38	79	1110	1110	516	1110
Effect of dispersant, 4800m ³ /d	Alve IFT 20mN/m	883	1891	568	1891	4640	8630	2158	4640
	Alve IFT 0.1mN/m	41	79	38	79	814	894	378	814
Flow rates, Svale	4800m ³ /d	883	1891	568	1891	7827	10719	3640	7827
	2400m ³ /d	2024	4344	405	4344	10719	10719	4984	10719
	7200m ³ /d	544	1162	289	1162	5518	10719	2566	5518
	9600m ³ /d	387	823	206	823	4313	10719	2006	4313
Flow rates, Alve	4800m ³ /d	883	1891	568	1891	4640	8630	2158	4640
	2400m ³ /d	2024	4344	405	4344	8630	8630	4013	8630
	7200m ³ /d	544	1162	289	1162	3005	8630	1397	3005
	9600m ³ /d	387	823	206	823	2916	8630	1021	2196
Effect of gas, Svale, 4800m ³ /d	GOR=0	883	1891	568	1891	7827	10719	3640	7827
	GOR=100	227	479	147	479	1806	10719	840	1806
	GOR=200	124	257	105	257	971	10719	451	971
	GOR=400	63	126	53	126	485	10719	225	485
Effect of gas, Alve, 4800m ³ /d	GOR=0	883	1891	568	1891	4640	8630	2158	4640
	GOR=100	227	479	147	479	699	8630	325	699
	GOR=200	124	257	105	257	302	8630	140	302
	GOR=400	63	126	53	126	119	8630	55	119
Effect of gas, Norne, 4800m ³ /d	GOR=0	883	1891	568	1891	10003	10003	4651	10003
	GOR=100	227	479	147	479	10003	10003	4651	10003
	GOR=200	124	257	105	257	10003	10003	4651	10003
	GOR=400	63	126	53	126	6472	10003	3135	6742
Different DOR, Svale, 4800m ³ /d	IFT 20mN/m	883	1891	568	1891	7827	10719	3640	7827
	IFT 5mN/m	387	823	289	823	5922	2754	5922	2401
	IFT 1mN/m	150	313	185	313	2974	2974	1383	2974
	IFT 0.1mN/m	41	79	38	79	1110	1110	516	1110
Different DOR, Alve, 4800m ³ /d	IFT 0.05mN/m	28	52	19	52	825	384	825	243
	IFT 0.01mN/m	13	20	10	20	414	192	414	153
	IFT 20mN/m	883	1891	568	1891	4640	8630	2158	4640
	IFT 5mN/m	387	823	206	823	2245	4768	1044	2245
Different DOR, Norne, 4800m ³ /d	IFT 1mN/m	150	313	105	313	1184	2394	551	1184
	IFT 0.1mN/m	41	79	38	79	814	894	378	814
	IFT 0.05mN/m	28	52	19	52	664	664	309	664
	IFT 0.01mN/m	13	20	10	20	334	334	155	334
Different DOR, Alve, 7200m ³ /d	IFT 20mN/m	544	1162	405	1162	3005	8630	1394	3005
	IFT 5mN/m	239	506	147	506	1488	4768	692	1488
	IFT 1mN/m	94	193	75	193	827	2394	385	827
	IFT 0.1mN/m	26	48	19	48	606	894	282	606
Different DOR, Norne, 7200m ³ /d	IFT 0.5mN/m	19	32	14	32	592	664	275	592
	IFT 0.1mN/m	13	20	10	12	334	334	155	334
	IFT 0.01mN/m	13	20	10	12	334	334	155	334
	IFT 0.01mN/m	13	20	10	12	334	334	155	334

C.6 Up-scaling of Laboratory Results

It is possible to predict the volume median diameter, d_{50} , for both laboratory experiments and full scale tests. To find the values, Equations (C.1) through (C.12) are utilized.

$$Q = \frac{\pi}{4} D^2 U \quad (C.1)$$

$$\text{We} = \frac{\rho}{\sigma} \left(\frac{4}{\pi} \right)^2 \frac{Q^2}{D^3} \quad (C.2)$$

$$Q_{\text{eq}} = \frac{\pi}{4} \text{We}^{1/2} \left(\frac{\sigma}{\rho} \right)^{1/2} D^{3/2} \quad (C.3)$$

$$U_{\text{oil}} = \frac{Q}{\frac{\pi}{4} D^2} \quad (C.4)$$

$$U_n = \frac{U}{(1-n)^{1/2}} \quad (C.5)$$

$$U' = U_n (1 + \text{Fr}^{-1}) \quad (C.6)$$

$$\text{Fr} = \frac{U_n}{g' D} \quad (C.7)$$

$$g' = \frac{g [\rho_w - \rho_{\text{oil}} (1-n)]}{\rho_w} \quad (C.8)$$

$$\text{We}' = \frac{\rho U'^2 D}{\sigma} \quad (C.9)$$

$$\text{Re}' = \frac{\rho U' D}{\mu} \quad (C.10)$$

$$\text{Vi} = \frac{\text{We}'}{\text{Re}'} \quad (C.11)$$

$$\frac{d_{50}}{D} = A \text{We}'^{-3/5} \left[1 + B \text{Vi} \left(\frac{d_{50}}{D} \right)^{1/3} \right]^{3/5} \quad (C.12)$$

C.7 Viscosity Measurements

Viscosity measurements were performed at different shear rates with the pure oils of Alve, Norne and Svale. The standard pre-treatment procedure for SINTEF Sealab was not followed. The oils were tempered to 13 °C before the tests were performed. The results from the measurements are presented in Figure C.8.

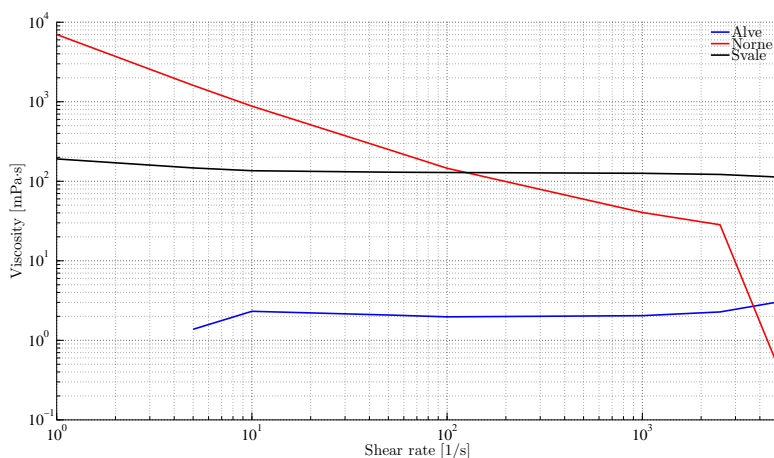


Figure C.8: Viscosity measurements of Alve, Norne and Svale performed at SINTEF Sealab to check and verify the already earlier measured viscosities.

C.8 Interfacial Tension Measurements

IFT measurements were performed with the spinning drop video tensiometer for the three oil types; Alve, Norne and Svale. Experiments were performed for both the pure oils, as well as for oils with premixed dispersant. The results from the measurements as a function of time are presented in Figure C.9.

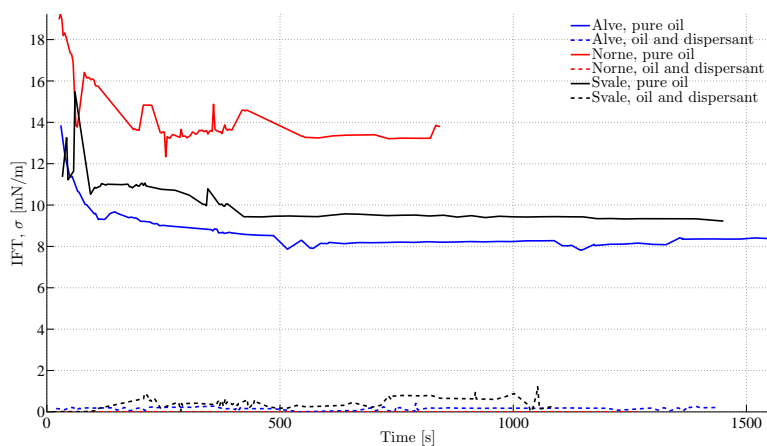




Figure C.9: IFT measurements of Alve, Norne and Svale as a function of time from the spinning drop video tensiometer.

D Health, Safety and Environment

The Health, Safety and Environment, HSE, evaluation for the Master's thesis is attached in the following. The next pages contains one page describing the mapping of high-risk activity, and two pages with a risk assessment for the Master's thesis. The evaluation is mandatory and must be completed before the thesis can commence. HSE has become more important these days, hence it has been a valuable experience to complete a risk assessment before the laboratory experiments were carried out.


NTNU		Kartlegging av risikofylt aktivitet				
						
HMS						
		Utarbeidet av	Nnummer	Dato		
		HMS-avd.	HMSRV/2601	22.03.2011		
		Godkjent av	Side	Erstatter		
		Rektor	1 av 1	01.12.2006		

Enhet: Institutt for kjemisk prosess teknologi /Department of Chemical Engineering
Deltakere ved kartleggingen (m/ funksjon): Peter Johan Bergh Lindersen (student), Per Johan Brandvik (veileder)

Dato: 18.01.2013

Kort beskrivelse av hovedaktivitet/hovedprosess: Programmering og simulering ved bruk av datamaskin, labforsøk med MiniTower


ID nr.	Aktivitet/prosess	Ansvarlig	Eksisterende dokumentasjon	Eksisterende sikringstiltak	Lov, forskrift o.l.	Kommentar
1	Programmering og simulering	Per Johan Brandvik	-	-	-	Ingen risikofylt aktivitet
2	Labforsøk med MiniTower	Per Johan Brandvik	-	-	HMS regler for SINTEF	Liten eller ingen risiko


NTNU	Risikovurdering			
				
HMS/IKS				
	utarbeidet av	Nummer	Dato	
	HMS-avd.	HMSRV2003	04.02.2011	
	godkjent av	side	Erstatter	
	Rektor	1 av 2	9.2.2010	

Enhet: Institutt for kjemisk prosesssteknologi /Department of Chemical Engineering
Linjeleder: Øyvind Gregersen
Deltakere ved risikovurderingen (m/ funksjon): Peter Johan Bergh Lindersen (student), Per Johan Brandvik (veileder)

Dato: 18.01.2013

ID nr	Aktivitet fra kartleggings-skjemaet	Mulig uønsket hendelse/belastning	Vurdering av sannsynlighet (1-5)	Vurdering av konsekvens:			Risiko-verdi	Kommentarer/status Forslag til tiltak
				Menneske (A-E)	Ytre miljø (A-E)	Øk/ materiell dømme (A-E)		
1	Arbeid med PC, programmering og simulering	Rygg- og nakkeproblemer, underarmsplager	1	A	-	-	A1	Dette arbeid vil i svært liten grad være skadelig for studenten
2	Labforsøk med MiniTower	Snuble i ledninger eller klemskader	1	A	-	-	A1	Dekke til løse ledninger, se seg for
	Labforsøk med MiniTower	Hodeskader ved å gå under stige	2	A	-	-	A2	Bruke hjem, ikke gå under stiger
	Labforsøk med MiniTower	VOC fra oljer, bruk av dispergeringsmidler	2	B	-	-	B2	Les datablader, ha avtrekk i rommet slik at VOC suges ut av rommet
Sannsynlighet 1. Svært liten 2. Liten 3. Middels 4. Stor 5. Svært stor				Konsekvens A. Svært liten B. Liten C. Moderat D. Alvorlig E. Svært alvorlig				
Risikoverdi (beregnes hver for seg): Menneske = Sannsynlighet x Konsekvens Ytre miljø = Sannsynlighet x Konsekvens Økonomi/materiell = Sannsynlighet x Konsekvens Omdømme = Sannsynlighet x Konsekvens								

NTNU		Risikovurdering		utarbeidet av	Nummer	Dato
 HMS/KS				HMS-avd.	HMSRV2603	04.02.2011
				godkjent av	side	Erstatter
				Rektor	2 av 2	9.2.2010



Sannsynlighet vurderes etter følgende kriterier:

Svært liten 1	Liten 2	Middels 3	Stor 4	Svært stor 5
1 gang pr 50 år eller sjeldnere	1 gang pr 10 år eller sjeldnere	1 gang pr år eller sjeldnere	1 gang pr måned eller sjeldnere	Skjer ukentlig

Konsekvens vurderes etter følgende kriterier:

Gradering	Menneske	Ytre miljø Vann, jord og luft	Øk/materiell	Omdømme
E Svært Alvorlig	Død	Svært langvarig og ikke reversibel skade	Drifts- eller aktivitetsstans >1 år.	Troverdighet og respekt betydelig og varig svekket
D Alvorlig	Alvorlig personskade. Mulig uørømt.	Langvarig skade. Lang restitusjonstid	Driftstans > ½ år Aktivitetsstans i opp til 1 år	Troverdighet og respekt betydelig svekket
C Moderat	Alvorlig personskade.	Mindre skade og lang restitusjonstid	Drifts- eller aktivitetsstans < 1 mnd	Troverdighet og respekt svekket
B Liten	Skade som krever medisinsk behandling	Mindre skade og kort restitusjonstid	Drifts- eller aktivitetsstans < 1uke	Negativ påvirkning på troverdighet og respekt
A Svært liten	Skade som krever førstehjelp	Ubetydelig skade og kort restitusjonstid	Drifts- eller aktivitetsstans < 1dag	Liten påvirkning på troverdighet og respekt

Risikoverdi = Sannsynlighet x Konsekvens
Beregn risikoverdi for Menneske. Enheten vurderer selv om de i tillegg vil beregne risikoverdi for Ytre miljø, Økonomi/materiell og Omdømme. I så fall beregnes disse hver for seg.

Til kolonnen "Kommentarer/status, forslag til forebyggende og korrigerende tiltak":
Tiltak kan påvirke både sannsynlighet og konsekvens. Prioriter tiltak som kan forhindre at hendelsen inntreffer, dvs. sannsynlighetsreducerende tiltak foran skjerpet beredskap, dvs. konsekvensreducerende tiltak.